Modelling precipitation hardening in an A356+0.5Cu cast aluminum alloy

Anass Assadiki

PSL UNIVERSITÉ PARIS

THÈSE DE DOCTORAT

DE L'UNIVERSITÉ PSL

Préparée à MINES ParisTech

Modélisation du durcissement par précipitation dans un alliage d'aluminium de fonderie A356+0.5Cu

Modelling precipitation hardening in an A356+0.5Cu cast aluminum alloy

Anass ASSADIKI

19 Juin 2020

École doctorale n°621

ISMME: Ingénierie des Systèmes, Matériaux, Mécanique, Énergétique

Spécialité

Sciences et génie des matériaux

Composition du jury :

Michel Perez Professeur, Université de Lyon	*Rapporteur*
David Balloy Professeur, Université de Lille	*Rapporteur*
Ivan Guillot Professeur, ICMPE	*Président*
Shahrzad Esmaeili Professeur, Université de Waterloo	*Examinateur*
Georges Cailletaud Professeur, MINES ParisTech	*Examinateur*
Warren J. Poole Professeur, Université de la Colombie-Britannique	*Examinateur*
Vladimir A. Esin Chargé de recherche, MINES ParisTech	*Examinateur*
Rémi Martinez Ingénieur de recherche PhD, Linamar	*Examinateur*

MINES ParisTech | PSL

Contents

Acknowledgements

First of all, I would like to thank all the members of the jury for being incredibly accommodating and flexible. My defense took place in a very peculiar context. The world was impacted by a sweeping pandemic and the initial date set for my defense coincided with the beginning of lockdown measures in many countries. The circumstances of the defense were being changed entirely and it was made considerably easier by the wonderful involvement of the members of jury.

My thanks go to Ivan Guillot for presiding over the jury and going over the complicated administrative work relative to the remote defense. Thanks to Michel Perez and David Balloy for accepting to examine my work. I greatly appreciated the precise and generous comments in your reports. Your presence in my jury is a true honor and I greatly enjoyed our discussion during the defense. My thanks go to Shahrzad Esmaeili for her great involvement in the examination of my work and the detailed feedback which was instrumental in the preparation of my defense and subsequent corrections of the manuscript.

Five years ago, I was accepted in the first class of the newly created specialized masters entitled design of materials and structures (DMS) at Centre des Materiaux MINES ParisTech. The mastermind behind the creation of this program was Georges Cailletaud. Through this program I was able to develop enough skills in metallurgy, mechanics and numerical computation to qualify for a PhD position. I am eternally grateful for all the late evening hours you stayed with me at the lab, Georges, directly teaching me important basics. Thank you for helping me through the most difficult times with your ruthless solution oriented mind and constantly positive attitude. Thank you for setting up the defense and going through the labyrinth of administrative procedures in the uncertain context it took place in. You will forever be my reference in terms of rigor, humility and positivity. The particular circumstances of my defense made it so that I was your very last PhD student. I wish you a happy retirement and I think every single one of your students would join me to thank you for your great service to research and teaching.

I was very lucky to have had the opportunity to spend a full year at the University of British Columbia in wonderful Vancouver - Canada. I was warmly welcomed and integrated in the aluminum research group lead by Warren J. Poole at the Materials Engineering Department. Thank you Warren for your hospitality and for making available critical human and material resources that were pivotal for the completion of this work. Warren, thanks to you I was reminded of the engineering part of materials science and engineering. Thank you for helping me

make the most of my stay in UBC and for coordinating the experimental work with McMaster University. I would like to also specifically thank Xiang Wang from McMaster University for all the meticulous and extensive TEM work featured in this manuscript. I am thankful for your generosity and hospitality during my visit to the CCEM.

I would like to thank Vladimir Esin for teaching me pretty much everything I know about metallurgy and thermodynamics. Vladimir, your humanity is without pair and every PhD student that worked with you, myself included, attributes a large part of their success to your support both technically and psychologically. Thank you for supporting me during the toughest times and for always taking into account personal circumstances in setting objectives for me.

Thank you Rémi Martinez, my industrial supervisor, for your continuous support despite major changes in your career path. You helped me keep the industrial element of this work in front of my eyes while still providing the freedom to dive deep into the science. Thank you for your mentoring and your involvement in setting up the PhD project.

I would also like to thank Denis Massinon for starting the research collaboration endeavor between Montupet (now Linamar) and Centre des Matériaux more than fifteen years ago. I am honored to have been a part of this large and continued research effort. I wish you all the best in your new career move.

I would like to thank Djamel Missoum, Nikolay Osipov and Kais Ammar for their help with Z-Set and coding issues generally speaking. You helped get me out on many tricky situations, your contribution has been pivotal for the accomplishment of this work.

Throughout my stay at Centre des Matériaux and UBC I have met some truly amazing people. Many of whom remain my best friends to this day. Alexiane, Nicolas, Laurane, William, Thomas, Aurélien and many others, thank you all for your friendship, your support and your priceless humor. I keep precious memories with each one of you, thank you for making this journey pleasurable !

Thank you mom and dad for all the sacrifices you have made so that I could pursue my studies and aspirations abroad. You have given me a wonderful upbringing and I am forever thankful for the values you instilled in me. Without your support and encouragement, none of this would have been possible. I love you and wish you health and serenity.

Thank you brother and sister for always taking care of me, your little brother. Thank you for always being encouraging and supportive.

Finally, to my wife and love of my life, I say thank you. You are my backbone and my muse. When I started my thesis I was a single international. By the end of it you had given me a family. Not in my wildest dreams did I picture my wife and my own daughter watching my PhD defense. I am eternally grateful to you. I love you both.

Introduction

The global ecological circumstances have had multiple organizing bodies opting for different ways to ensure the sustainability of the environment. The European Union (EU) has been particularly responsive to the global ecological challenges. Regarding transport vehicle emissions, the EU has been setting, during the past three decades, increasingly stringent toxic emission standards on new vehicles (Figure 1). Carbon monoxide (CO), nitrous oxydes (NO_x) and particulate matter (PM) are the main combustion engine emissions concerned with these regulations. These emissions fall under the local category while carbon dioxide (CO_2) for example is considered a more globally acting pollutant. A limit of 130 g/km of CO_2 emission was set between 2012 and 2015, and a target of 95 g/km will apply by 2020 [1].

All these requirements translate into design constraints and directives for automotive manufacturers. Two main development directions ensue: weight reduction and the amelioration of the efficiency of internal combustion engines. Lighter weight allows the reduction of fuel consumption which results in fewer toxic emissions. More efficient engines have higher specific power[1] as they make better use of fuel. This allows engine downsizing without any loss in performance.

These development directions have been driving the substitution of steel and cast iron with lighter alloys such as aluminum alloys and, less predominantly, magnesium alloys [2]. Extensive use of aluminum alloys in the structure and body panels of vehicles is entering the market nowadays. One impressive example is the 2015 Ford F-150 pick-up truck losing around 300 kg in comparison to its predecessor [3].

Regarding engines, there has been an ever-growing shift in the last two decades from iron to aluminum alloys. It is worth noting that this substitution concerns mainly cylinder heads (Figure 2), although aluminum engine blocks are becoming increasingly prevalent. Aside from the obvious and significant weight reduction (at least 50%), use of aluminum alloy is also motivated by its high thermal conductivity which allows more efficient heat extraction. The cylinder head contains gas, coolant and lubrication oil circuits which are independent from one another. The internal geometry of the cylinder head is therefore highly intricate. Thus these parts are manufactured using various casting processes. Cast aluminum alloys offer an advantage in that area as well as they possess good castability and are compatible with subsequent finishing manufacturing processes. Their significantly lower melting temperatures compared to iron presents an additional cost related

[1] Power per unit volume of engine displacement.

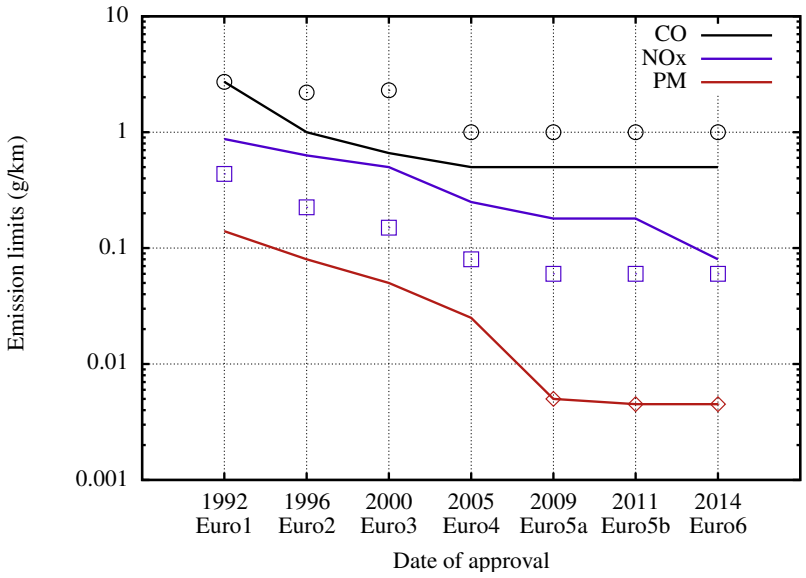

Figure 1 – The Euro emission standards for diesel engines (lines) and petrol engines (points) [1].

advantage.

Obtaining higher engine efficiency requires the alteration of the thermodynamic conditions under which the combustion reaction takes place. Higher levels of temperature and pressure have to be achieved in the combustion chambers to ensure a more complete combustion of the air and fuel mixture. Consequently, the search for higher efficiency leads to more severe service conditions for the constituent alloys leading to their premature aging. In order to satisfy these requirements, the potential of aluminum alloys for cylinder heads has to be exploited in its entirety. This can only be achieved by acquiring better control over the process-microstructure-properties triptych.

Cast aluminum alloys draw their properties from precipitation microstructures, the formation and evolution of which are diffusion controlled. It is then paramount to understand and model the effect of thermal exposure on the precipitation kinetics and their subsequent effect on mechanical properties.

First, one can distinguish the phenomenological approach to model the aging behavior of aluminum alloys. It consists in the introduction of internal variables into the constitutive equations of the material accounting for the progression of the aging process [5, 6]. It is an easy to implement and straightforward approach which also presents the advantage of relatively low calculation costs. However, the absence of any physical underpinning to the internal variables is a major drawback. Also, the additional constitutive law parameters have to be identified through extensive mechanical tests for each alloy composition and heat treatment state. Such approaches are very useful for in-service behavior simulations without being suitable for sharp thermal transients. For example, simulation of the effect of solutionizing heat treatments fall outside of the domain of applicability of such

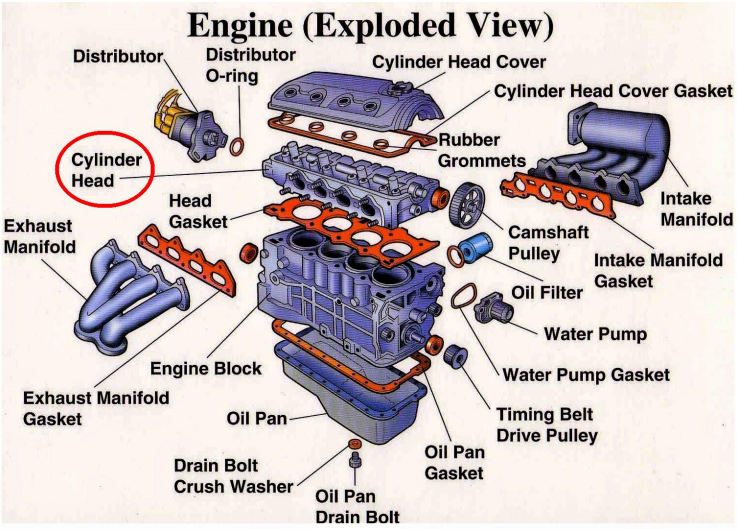

Figure 2 – Exploded view of an internal combustion engine showing the position of the cylinder head [4].

methods.

It is the second type of "microstructure-informed" approaches that allow the simulation of such thermal histories [7, 8, 9, 10, 11]. These approaches are more closely related to the emerging integrated computational materials engineering (I.C.M.E.) discipline [12]. Physics-based models are relied upon to describe the temperature dependent precipitation kinetics on the one hand, and precipitation state dependent mechanical properties on the other hand. The impact of the microstructural evolution in the alloy is therefore directly integrated in the calculation chain. Obviously, this means that these type of models hold more predictive capabilities. It is also possible to extend them to different chemical compositions which can be used for designing new alloys. However, calculation costs increase significantly in comparison to phenomonological approaches.

The aim of this work was to develop a multiscale calculation chain enabling simulations of heat treatments of cylinder heads manufactured using cast aluminum alloys of type A356+0.5Cu. The modelling effort starts at the microscale with a precipitation kinetics model following on work done by Martinez *et al.* for A319 type alloys [13]. A transition to the macroscale is represented by a hardening model allowing the description of the evolution of yield strength in full dependence of the precipitation state. The validity of both levels of the model is verified using the results of an experimental microstructural study and tensile test campaign performed on an A356+0.5Cu at different aging states. Finally, coupling to the finite element method (FEM) ensures the transition to the structural scale. The end result will be to calculate the mechanical property gradient within the cylinder head due to the heterogenous thermal exposure during heat treatments.

This manuscript is organized in five chapters with a conclusion and perspectives at the end. This work has been conducted over a period of three years. The first

and third year took place in Centre des Matériaux Mines ParisTech in Evry, France, and the second year was spent in the Advanced Materials and Process Engineering Laboratory of the University of British Columbia in Vancouver, Canada. While it is written in the english language, a chapter summary in french can be found preceding each chapter. The first chapter provides the reader with elements of scientific and industrial context as well as certain fundamentals from literature. The second chapter presents the results from the microstructural and mechanical characterization campaign conducted on the A356+0.5Cu alloy. Chapter three outlines the components of the precipitation kinetics model and its governing equations. Simulations are then compared to the results of the microstructural characterization. Finally, chapter four, describes the yield stress model and its coupling to the precipitation model and the integration of the model to the FEM method. The yield stress model is confronted to the mechanical characterization results and a 2D examples of FEM calculations is presented.

Chapter 1

Industrial and scientific context

Résumé

La culasse est une pièce critique du moteur à combustion interne. Il s'agit d'une pièce géométriquement complexe qui subit des contraintes thermomécaniques sévères en service. En réponse aux exigences écologiques, les culasses sont dorénavant fabriquées principalement avec des alliages d'aluminium.

Dans ce chapitre, le fonctionnement du moteur à combustion interne est rappelé en soulignant le rôle de la culasse dans chaque étape. Ensuite, les étapes du procédé de fonderie utilisé pour la fabrication des culasses sont détaillées. Des généralités sur l'aluminium et ses alliages sont présentées, en portant un intérêt particulier aux alliages de fonderie de la série 3xx qui font l'objet de ce travail.

Les étapes de solidification dendritique sont expliquées et les microstructures résultantes sont décrites. Finalement, l'importance des traitements thermiques dans l'activation du durcissement par précipitation et, *in fine*, l'amélioration de la dureté est illustrée. Les étapes des traitements thermiques, leur classification, ainsi que les séquences de précipitation ayant lieu sont présentées. Un inventaire des phases participant aux séquences de précipitation de chaque famille d'alliages est établi.

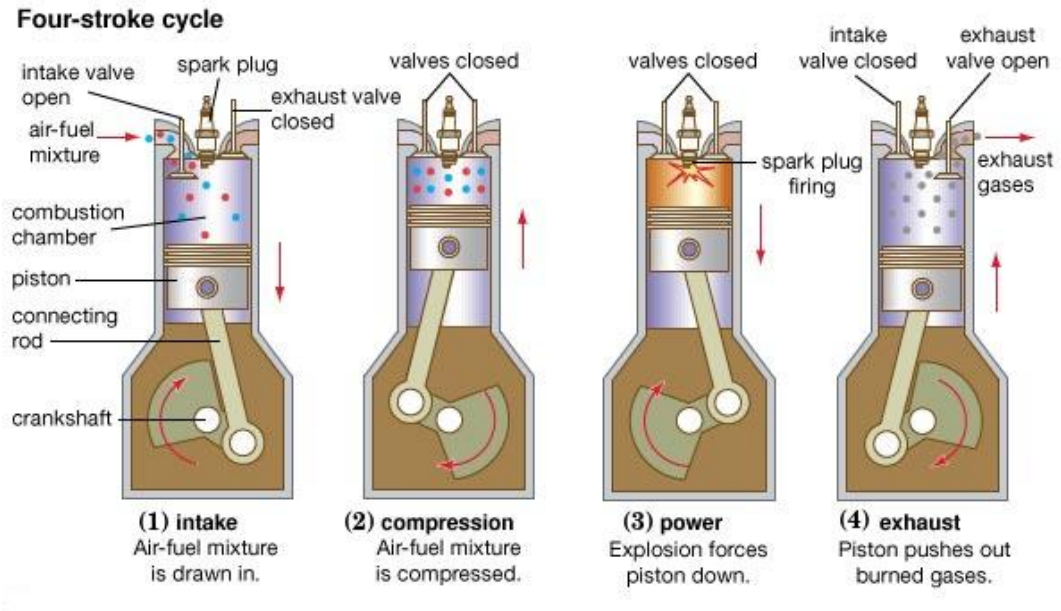

Figure 1.1 – Schematic of the 4 strokes that make up a thermodynamic cycle of a petrol internal combustion engine [14].

1.1 Cylinder heads

Internal combustion engines convert the energy produced by the combustion reaction of the air and fuel mixture into kinetic energy. The combustion occurs in a combustion chamber in which wall temperature and pressure are controlled. In a 4-stroke piston engine, this chamber consists of the enclosed space between the engine block cylinders, the cylinder head and the pistons. The air and fuel mixture is introduced into the chamber through the cylinder head during the intake stroke (a.k.a. the induction stroke). The pistons then compress the mixture against the fire deck of the cylinder head during the compression stroke. The combustion then either occurs spontaneously (diesel engines) or forcibly thanks to a spark plug (petrol engines) during the power stroke (a.k.a. the ignition stroke). The combustion gases then expand pushing down the pistons that transfer their motion to the crankshaft all the way to the wheels through the remaining elements of the powertrain. Finally, the cycle ends in the exhaust gases being pushed out by the pistons through the exhaust circuit of the cylinder head during the exhaust stroke (Figure 1.1).

The cylinder head plays major roles all throughout the thermodynamic cycle of an internal combustion engine. It hosts the intake and exhaust valves as well as independent circuits for exhaust gases, coolant and lubricant oils. It evidently is one of the most geometrically complex parts of the internal combustion engine. This part is subject to large amounts of thermomechanical stresses during service. Temperatures as high as 280°C can be reached in the hottest areas of the firedeck of the cylinder head, usually the intervalve brigdes (Figure 1.2). Add to that,

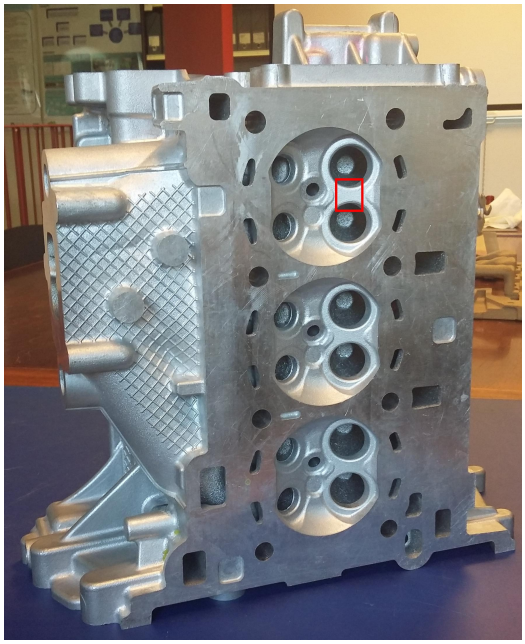

Figure 1.2 – Firedeck side of the cylinder head for the Ford 1.0L 3 cylinder engine with the integrated exhaust manifold (the red square shows the sensitive intervalve area).

pressures approximating 180 bars are reached inside the combustion chambers. It is also worth mentioning that important stresses ensue from bolts and/or screws assembling the cylinder head to the engine block.

The intricacy of the internal geometry of cylinder heads reduces the compatible manufacturing processes to gravity and die casting. While additive manufacturing processes are capable of producing such geometries, they are far from being suitable for this application for obvious cost and technology readiness considerations.

The manufacturing process of cylinder heads is detailed in 7 major steps in the following paragraphs.

1) Alloy preparation: In a melting furnace, aluminum master alloys in the form of ingots are introduced in appropriate proportions to produce the desired compositions. Chemical spectroscopy allows for control over this process and for potential deviations from the specifications to be systematically corrected. The resulting melt is poured in a transfer ladle where it gets degassed using a nitrogen jet. This ensures that excess hydrogen is extracted which drastically reduces subsequent porosity of the castings. Finally, the molten slag is removed and the melt is poured in a suspension furnace awaiting casting.

2) Coring: The internal cavities of the cylinder head are produced with sand cores that are prepared in coring boxes using sand and resin mixtures. Usually, multiple separate cores have to be produced and then glued together to produce the entirety of the internal geometry of the part.

3) Casting: The sand cores are placed inside the mold (or the die in the case of injection casting). The metallic parts of the mold are usually sprayed with a demolding agent to prevent gripping once solidification occurs. This also minimises contamination of the liquid melt with iron from the tooling. The melt is then poured (or injected) into the mold and is left to solidify.

4) Decoring: The cast solidifies around the sand cores which have to be subsequenty removed. This can be achieved by subjecting the cylinder head to various hammerings and vibrations. Although a thermosetting resin is used in the manufacturing process, the recuperated sand can still be recycled and reused.

5) Cutting: Excess metal, which consists of feeders, fillers and sprues is removed to obtain the near-finished shape of the cylinder head. This scrap metal is carefully sorted according to chemical composition in order to be fully recycled and reused.

6) Heat treatment: Certain cylinder heads are delivered as-cast, in what is called the F state. However, in the F state, the mechanical properties of the aluminum alloys are significantly low in comparison to the heat treated states (labelled T5, T6, T64, T7, etc..). Such cylinder heads are usually mounted in low performance small engines. In most cases, cylinder heads are required to undergo specific heat treatments to improve their mechanical properties. Heat treatment sequences include solutionizing, quenching or controlled air cooling and subsequent aging heat treatments. The mechanical properties are improved thanks to the precipitation microstructures that are obtained as a consequence of the heat treatment. A detailed description of the different types of heat treatments as well as the phenomena responsible for the precipitation microstructures can be found in the following sections.

7) Machining: The cylinder heads are machined to obtain the final shape according to client specifications.

1.2 Overview on aluminum and its alloys

Aluminum is the third most abundant element in the crust of planet Earth. The main aluminum ore in the world is a mineral called bauxite containing 30 to 60 % aluminum oxides and it is strip-mined in many areas in the world [15]. Bauxite is refined into alumina (Al_2O_3) thanks to the Bayer process [16]. In the early 19^{th} century, producing aluminum from alumina was extremely complicated and costly making aluminum more expensive than gold and silver. At this point, applications of aluminum were limited to jewelry and luxury cutlery [17].

In 1886, chemists Charles Hall from the USA and Paul Héroult from France, independently and almost simultaneously developed an electrolysis process which drastically reduced the cost of aluminum smelting. This discovery coincided with

the emergence of large industries to which aluminum and its alloys would be a perfect fit: transportation of electricity, internal combustion engine driven vehicles and aeronautics [15]. Thus, aluminum and its alloys made their entry into these markets thanks to their properties of high thermal and electrical conductivity, good mechanical properties, intrinsic corrosion resistance, low density and low melting temperature.

Pure aluminum has the following elementary physical properties:

- Crystal structure : Face-centered cubic (FCC);
- Lattice parameter at 25°C : a = 0.404 nm;
- Melting temperature : T_m = 660°C ;
- Density near room temperature : d = 2700 kg.m^{-3};
- Thermal conductivity at 25°C : k = 217.6 W.m^{-1} .K^{-1};
- Electrical resistivity at 25°C : ρ = 2.63x10^{-8} Ω.m;
- Proof stress : 30 to 40 MPa.

Pure aluminum has mediocre mechanical properties and is usually alloyed to other chemical elements to increase its strength.

Aluminum master alloys are available in two different categories:

Primary alloys: originating from aluminum smelters, characterized by high levels of purity. These alloys are destined for top tier industries such as aeronautics in which the high added value products justify the high cost of raw materials.

Secondary alloys: originating from recycling, characterized by the presence of notable amounts of impurities. Iron is chief among these impurities in terms of the negative impact on mechanical fatigue properties. These alloys are better suited for the automotive industry due to their significantly low cost (95 % less than primary alloys).

Another categorization of aluminum alloys can be established on the basis of the metalworking process type to which they are destined. Two categories can be distinguished: wrought alloys and cast alloys. The former are destined for processes involving plastic deformation such as extrusion, rolling, stamping and deep drawing. The latter are destined for casting processes which involve transformation to the liquid state. Tables 1.1 and 1.2 present a summary of the main aluminum alloy series with their respective main alloying elements and applications for each category.

The designation system used is that of the north american Aluminum Association Incorporated which is the most widely used [18, 19]. Note that Tables 1.1 and 1.2 also show whether each series is heat treatable or not, which is yet another categorization of aluminum alloys. The strength of a heat treatable alloy can be

increased by subjecting it to a heat treatment as opposed to a non-heat treatable one. However, aluminum alloys can also be strain hardened to have their strength increased but this applies only to wrought alloys since castings are generally never deformed.

While most alloying elements are used to control mechanical properties, some of them are added to modify process related behavior as well as resistance to certain types of corrosion (stress, pitting and crevice corrosion). It is worth noting that, for casting applications that involve complex geometries, series 3xx and 4xx are the most widely used as alloying with silicon improves castability.

Table 1.1 – Summary of the main wrought aluminum alloy series with their main alloying elements and their applications [19, 15].

Series	Alloying elements	Heat treatable	Application
1xxx	min. 99 %wt. Pure Al	No	Electric wires, foil, packaging
2xxx	Cu	Yes	Aerospace, automotive, pressure vessels
3xxx	Mn	No	Beverage cans, heat exchangers
4xxx	Si	Yes[1]	Wires
5xxx	Mg	No	Marine, automotive
6xxx	Mg + Si	Yes	Extrusions for aerospace, automotive, marine and construction
7xxx	Zn	Yes	Aerospace and automotive (high strength)

[1]: with some exceptions

Table 1.2 – Summary of the main cast aluminum alloy series with their main alloying elements and their applications [19, 15].

Series	Alloying elements	Heat treatable	Application
1xx	minimum 99 % Pure Al	No	N.A.
2xx	Cu	Yes	Aircraft construction and high pressure casings
3xx	Si + Mg and/or Cu	Yes	Cylinder heads, engine blocks, pistons, casings, wheels
4xx	Si	Yes	Thin walled intricate casings
5xx	Mg	No	Fittings, utensils
7xx	Zn	Yes	Farming and mining tools, furniture
8xx	Sn	No	Bearings, bushings

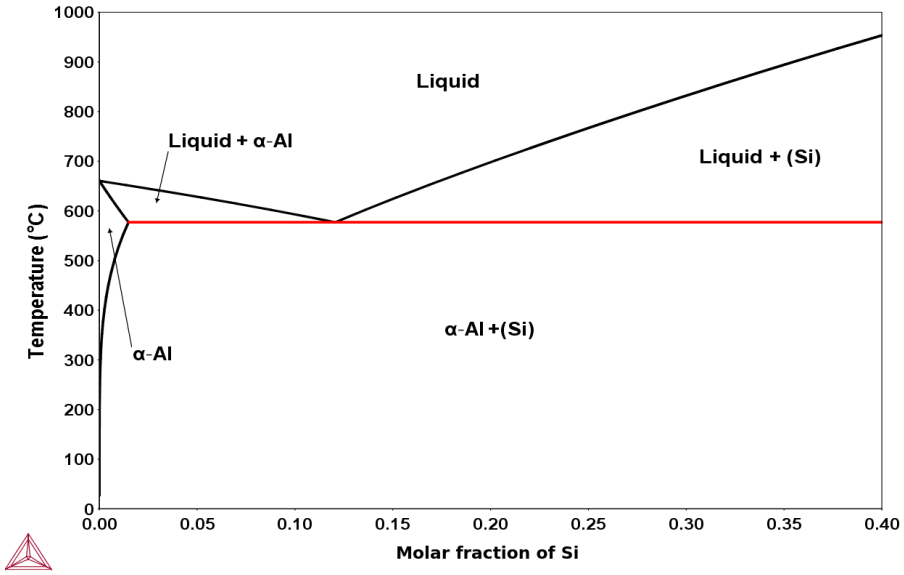

Figure 1.3 – Al-Si binary phase diagram at atmospheric pressure, calculated using Thermo-Calc (TCAL4 database).

1.3 Cast aluminum alloys of the 3xx series

The 3xx series of aluminum alloys designates alloys containing large quantities of silicon (6 to 13 %wt.) along with either copper, magnesium or both. Silicon improves castability (flow properties of the liquid phase) and it expands during solidification compensating the relatively high shrinkage of aluminum (about 5.6 %). This allows a more economical design of the feeders and gives further design freedom in terms of small-dimension details. Furthermore, it reduces the risk of hot-tear cracking and the appearance of shrinkage cavities in the castings. Finally, as can be seen in the Al-Si binary phase diagram (Figure 1.3), adding silicon to aluminum decreases the melting temperature which has obvious impacts on energy consumption during processing.

1.3.1 Solidification

Solidification can occur when a metal reaches temperatures below its melting (liquidus) temperature T_m. However, this transformation can take place spontaneously and homogeneously only when high levels of undercooling are reached (i.e. high values for $\Delta T = T_m - T$). Therefore, solid nuclei usually start forming on the mold walls rather than the much hotter core. These nuclei then grow competitively to form the grain structure. In order to control the grain size, heterogeneous nucleation can be induced by providing preexisting sites that reduce the interfacial term of the free energy associated with solidification. This process is referred to as "inoculation", and for cast aluminum alloys of the 3xx series it is usually achieved by adding TiB_2 particles to the melt [20].

When Al-Si alloys are cast, solidification starts from the mould walls and potentially in sufficiently undercooled regions around inoculant particles. In the example of a hypoeutectic alloy (<13%wt. Si), the solidification path is as follows (α-Al refers to the FCC aluminum solid solution):

Liquid $\rightarrow$ Liquid + Primary α-Al $\rightarrow$ Primary α-Al + Eutectic constituant (α-Al + Si phase).

The equilibrium concentration of Si in the α-Al phase decreases as temperature is decreased. Therefore the formation and growth of α-Al is accompanied by the rejection of excess Si back into the liquid. This increases the Si concentration of the liquid near the solid/liquid interface which decreases its solidus temperature. It is what is referred to as constitutional undercooling. It can be assumed that during the first stages of solidification the solidification front remains planar. However, a local increase of the growth velocity of the interface can create a protrusion in the solid/liquid interface (Figure 1.4a). Seeing as the protrusion can expell excess solute more efficiently (larger contact surface with the liquid), its surrounding area witnesses a stronger constitutional undercooling. This makes it more likely for another protrusion to form in the neighboring area, and then process repeats itself. These protrusions then develop into long arms the surface of which can also become unstable and break up into secondary or even tertiary arms. The continuous enrichment in solute of the liquid between these arms moves its composition towards the eutectic composition. Once reached, the liquid isothermally solidifies into the eutectic constituent, i.e. there is a simultaneous formation of α-Al and the Si-phase. This solidification structure is referred to as "dendrite" from the greek "*déndron*" for tree (Figure 1.4b) [21].

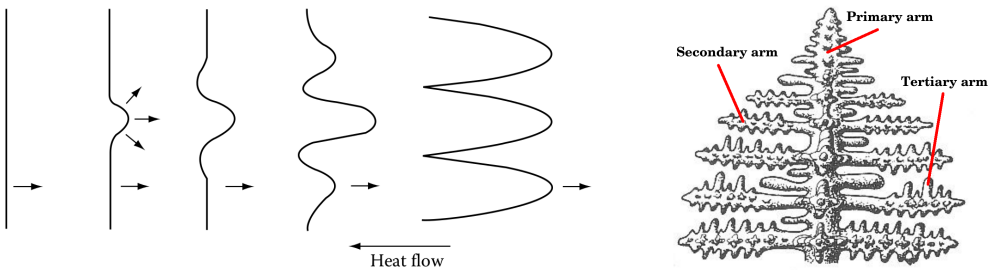

(a) (b)

Figure 1.4 – Schematic of dendrite formation and morphology : (a) stages of breakdown of a planar solid/liquid interface which forms the dendritic structure [22] and (b) a dendrite with its primary, secondary and tertiary arms [23].

1.3.2 Alloying elements

Alongside silicon, other chemical elements are found in the composition of 3xx series cast aluminum alloys. There are three families of alloys in this series that

are the most widely used in automotive applications. They are summarized in Table 1.3 along with their composition ranges and the hardening phase systems they rely upon. The alloying elements present in these alloys alter its microstructure and, *in fine*, its properties in ways that will be described hereafter.

Silicon: In addition to its previously described effect on casting related properties, silicon contributes to the formation of a hardening phase with magnesium (the β-Mg_2Si system). Silicon also forms the pure silicon phase which is very hard compared to α-Al which raises the hardness of the alloy and decreases its ductility. The hardness difference between the aforementioned phases explains the decohesive ductile failure behavior of such alloys where voids nucleate, grow and coalesce at the interface between these two phases [24]. The Si-phase in an as-cast alloy generally has a fibrous or lamellar morphology with sharp edges depending on the solidification velocity and the presence of interfering agents such as strontium (Figure 1.5a and 1.5b). If left unmodified, these sharp edges of the Si-phase act as stress concentrators and can promote crack initiation [25]. The high hardness of the Si-phase increases wear resistance of the alloy which decreases its machinability.

Copper: It contributes to the formation of a hardening phase (the θ-Al_2Cu system) therefore improving yield strength and hardness. Combining it with silicon and magnesium leads to the formation of another hardening phase (the Q-phase system). However, it has detrimental effects on corrosion resistance and lowers the thermal conductivity of the alloy when added in large amounts. It can also decrease the resistance of the alloy to hot-tear cracking [26].

Magnesium: As mentioned before, it participates in the formation of hardening phases together with silicon (β-Mg_2Si) or silicon and copper (Q-phase). It reinforces corrosion resistance of the alloy but reduces its castability and machinability [6].

Strontium: This element is added in small amounts (100 to 200 ppm) to modify the structure of the eutectic constituent. It disturbs the competitive growth of the Si-phase into lamellae thanks to its high atomic radius. This promotes the fibrous morphology over the lamellar morphology and allows the subsequent globularization of the Si-phase with solutionizing heat treatments (Figure 1.5c). The globularization of the eutectic Si-phase occurs due to the existence of a driving force for ripening at the solutionizing temperature. Assuming an isotropic interface energy, this driving force is due to the fact that a spherical shape has the smallest surface area per volume than any other shape, thus a globular morphology reduces the total free energy. The Si-phase in its globular morphology is far less deleterious to dynamic mechanical properties than its alternatives. It is worth noting that other elements such as sodium, calcium or antimony have similar effects.

Iron: While iron is not to be considered an alloying element *per se*, it is worth mentioning its significant effects on the properties of cast aluminum alloys.

As mentioned previously, it is prevalent mostly in secondary alloys. Frequent contact with iron in tooling and assembly increases its amounts in recycled alloys. Therefore, it is present in the composition as an ineradicable impurity (0.25 to 0.8 %wt. versus 0.03 to 0.15 %wt in primary alloys). Due to its very low solubility in α-Al, iron forms iron-rich intermetallic phases during solidification. In the presence of silicon alone, the observed phases are either the α-Al_8Fe_2Si phase or the β-Al_5FeSi. When magnesium is also present the π-$Al_8FeMg_3Si_6$ phase can form and in the presence of manganese, the α-$Al_{15}(Fe,Mn)_3Si_2$ phase can be observed [27]. These phases have different morphologies as is shown in Figure 1.6 and while they all have a negative impact on ductility and fracture behavior, the platelet-shaped β-Al_5FeSi phase is reported to be the most deleterious (Figure 1.6b) [28].

Table 1.3 – Cast aluminum alloy families of the 3xx series for automotive applications.

Family	Alloying elements (%wt.)	Hardening phases	Example alloy
Al-Si-Cu	Cu - 3 to 5 %	θ-Al_2Cu	A319 (Al-7%Si-3%Cu)
Al-Si-Mg	Mg - 0.25 to 1%	β-Mg_2Si	A356 (Al-7%Si-0.4%Mg)
Al-Si-Cu-Mg	Cu - 0.5 to 1% Mg - 0.3% Mg	θ-Al_2Cu β-Mg_2Si Q-phase	A356+0.5Cu (Al-7%Si-0.4%Mg-0.5%Cu)

1.3.3 As-cast microstructure

In light of what was presented up to here, it can be summarized that the as-cast microstructure of a 3xx series aluminum alloy contains the following features: α-Al dendrites, the eutectic constituent, iron-rich intermetallics and intermetallics involving alloying elements with hardening potential (θ-Al_2Cu, β-Mg_2Si and Q).

In addition to these phases, the presence of cast defects and gas pores is also characteristic of these alloys (Figure 1.7). Although they both appear as voids in the microstructure, pores containing gas can be distinguished thanks to their roundness. Casting defects are due to shrinkage and can occur as a consequence of an inappropriate design of feeders. Pores in cast aluminum alloys are due to the high solubility of hydrogen in liquid aluminum. Hydrogen diffuses very easily in solid aluminum which allows it to form gas bubbles of molecular hydrogen (H_2). Although the melt is degassed using a nitrogen jet, some hydrogen can still remain in the melt and it can also be picked up during the casting operations.

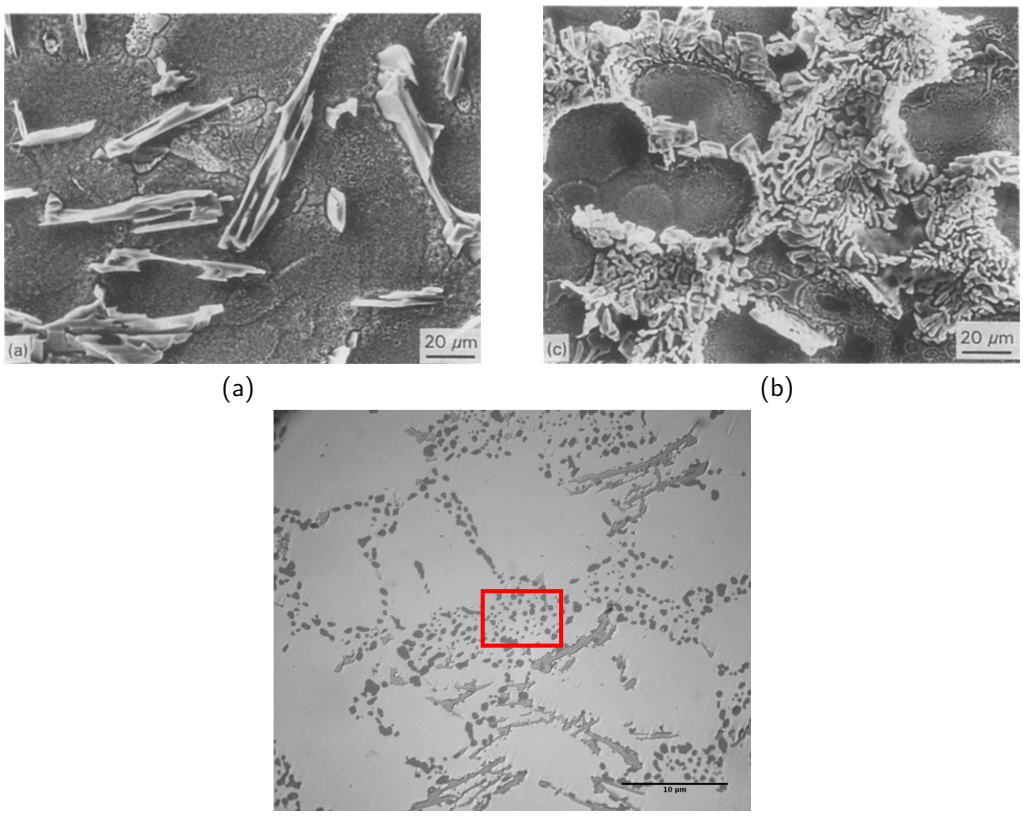

(a) (b)

(c)

Figure 1.5 – Deep-etched micrographs of a 319 alloy : (a) SEM secondary electron micrograph of non-modified as-cast alloy showing a lamellar eutectic Si-phase morphology, (b) SEM secondary electron of a Strontium-modified as-cast alloy showing a fibrous eutectic Si-phase morphology [29] and (c) optical micrograph of a T7 heat treated 319 strontium-modified alloy showing the globular morphology of the eutectic Si-phase [7].

As shown in figure 1.8, the phases that have hardening potential have large and bulky shapes in the as-cast state. Their effect on the yield strength of the alloy is very limited in this state. It is only after proper heat treatments that their hardening potential is unlocked and mechanical properties are improved.

1.4 Precipitation hardening and heat treatments

Hardening occurs when free movement of dislocations is impeded therefore allowing the material to accommodate more deformation energy. Among the possible obstacles to the movement of dislocations are grain boundaries, other dislocations, solute atoms and precipitates. For cast aluminum alloys precipitation hardening constitutes the biggest contribution to the yield strength. However, the primary precipitates obtained after solidification are not effective in impeding dislocation movement due to their large dimensions and their heterogeneous distribution. In

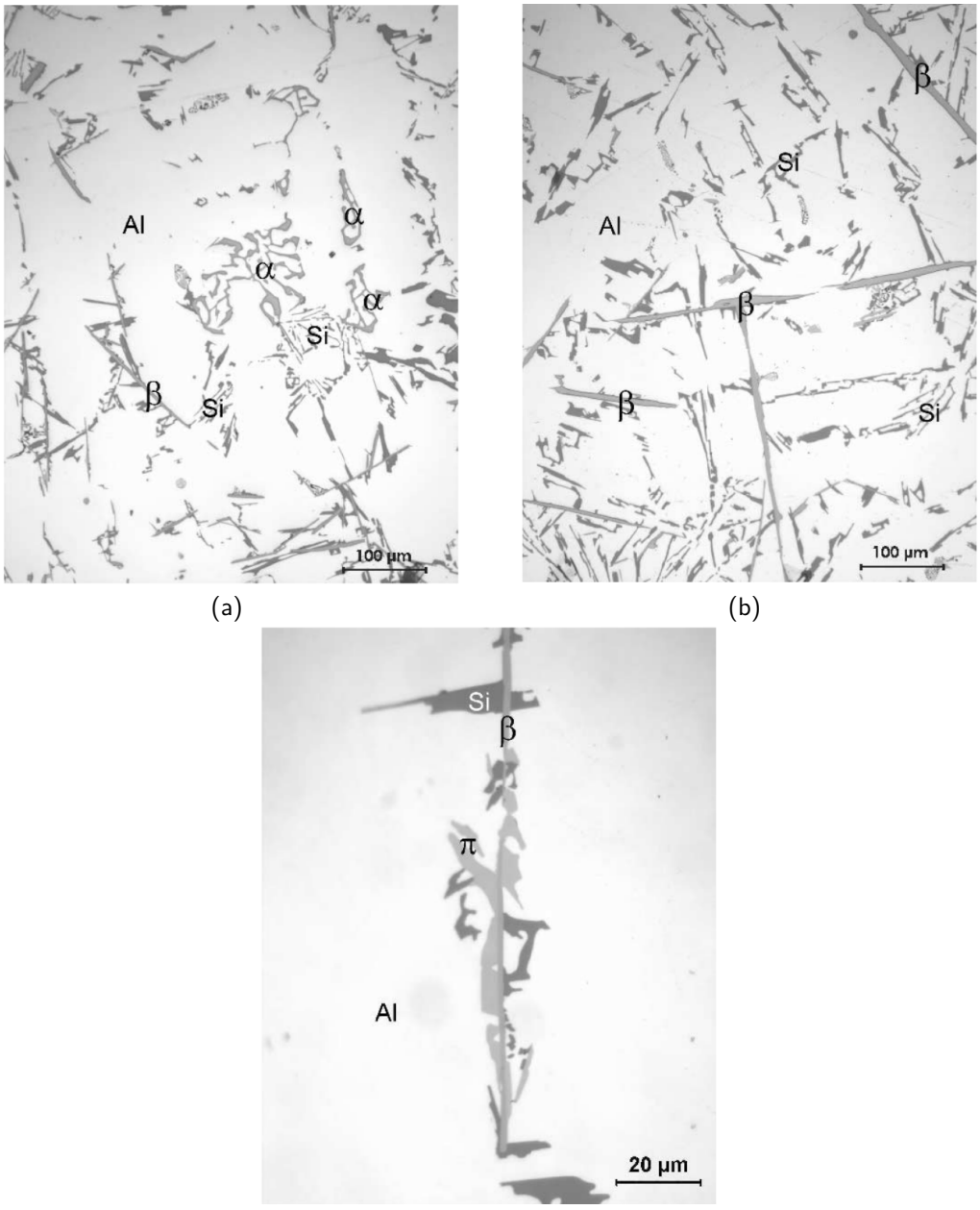

Figure 1.6 – Optical micrographs showing the different iron-rich intermetallic phases and their different morphologies in an A356 alloy (Al-7%Si-0.4%Mg) : (a) Chinese-script shape of the α–$Al_{15}(Fe,Mn)_3Si_2$, (b) platelet shape of the β–Al_5FeSi and (c) blocky shape of the π-phase [28].

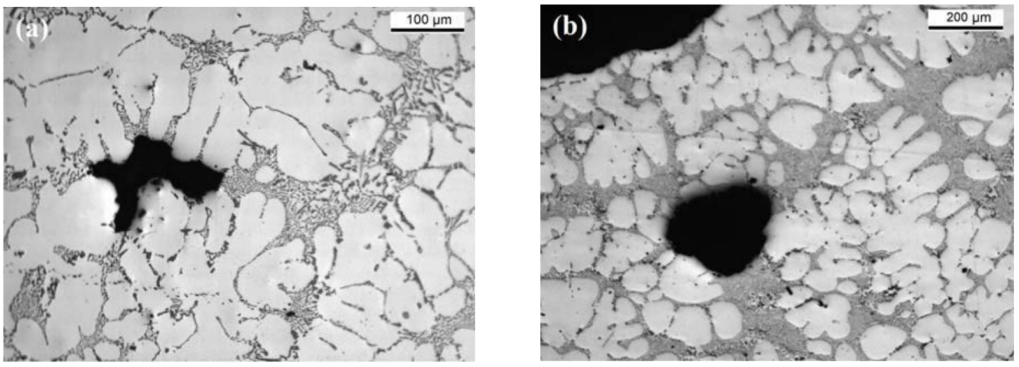

(a) (b)

Figure 1.7 – Micrographs of an Al-7%Si0.3%Mg alloy showing void defects : (a) shrinkage void and (b) gas porosity [30].

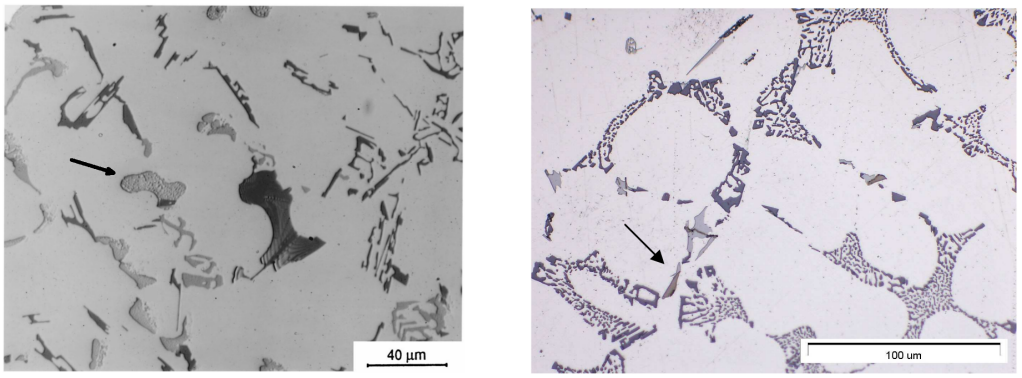

(a) (b)

Figure 1.8 – Hardening phases in the as-cast state : (a) micrograph showing the θ-Al_2Cu in an as-cast 319 alloy [31] and (b) micrograph showing a bulky β-Mg_2Si particle in an as-cast A356 alloy [32].

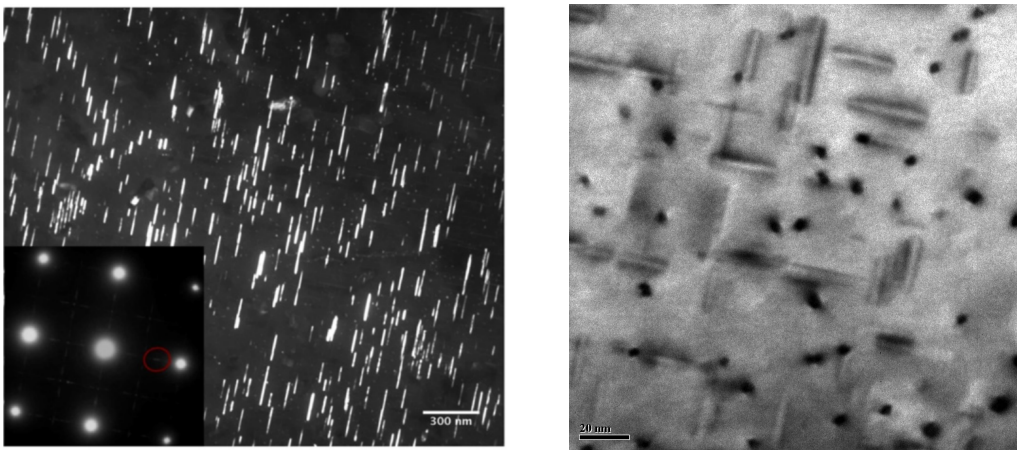

(a) (b)

Figure 1.9 – Hardening phases in heat-treated 3xx series aluminum alloys : (a) dark field TEM micrograph of θ'-Al_2Cu precipitates in a heat treated 319 alloy [33] and (b) Bright field TEM micrograph of β''-Mg_2Si precipitates in a heat treated A356+0.5Cu alloy (this study).

order to optimize the contribution of the precipitates to the yield strength, their size, distribution and their structure have to be controlled.

1.4.1 Heat treatments

Effective precipitation microstructures such as those presented in Figure 1.9 are obtained as a consequence of subjecting the alloy to heat treatments. For cast aluminum alloys, these heat treatments generally follow the steps hereafter:

Solutionizing: The alloy is exposed for a number of hours to high temperatures at which phases such as θ-Al_2Cu, β-Mg_2Si and Q are thermodynamically unstable (generally above 500°C).

This leads to their partial or full dissolution and the enrichment of the α-Al solid solution in solute atoms (Mg, Cu and Si). Since dissolution is diffusion controlled, the higher the solutionizing temperature the lower the duration at which the alloy has to be maintained under it. However, the as-cast condition being chemically heterogeneous, it is probable that certain areas in the alloy are at near-eutectic compositions which lowers their melting temperature. Therefore, solutionizing temperatures must be low enough to avoid incipient melting, i.e. localized melting of the alloy which has catastrophic effects on the mechanical properties.

In order to gain in high temperature exposure time (and therefore in energy cost), it is possible to perform step-solutionizing. A first step at low temperature begins the dissolution process while also homogenizing the composition therefore eliminating the risk of incipient melting. Then follows a second step at higher temperature which accelerates dissolution.

It is important to recall that exposure to such high temperatures is what allows the eutectic Si-phase to take its globular shape in a strontium-modified alloy.

Quenching: After solutionizing, the alloy is cooled rapidly, usually by immersion in a water bath. Rapid cooling prohibits the formation of phases due to the insufficient time for diffusion. Therefore, a thermodynamically unstable supersaturated α-Al solid solution is obtained.

It is worth noting that during quenching, residual stresses appear in the casting as a consequence of the thermal shock. The water baths are usually maintained at temperatures of 65 to 90°C to attenuate this shock.

Natural aging: The alloy is maintained at room temperature where the supersaturated solid solution can already start to decompose and nanometric clusters of solute atoms can form. These clusters are usually identified as the Guinier-Preston (GP) zones which can appear as disks of solute atoms in the aluminum matrix (Figure 1.10). Signs of precipitation hardening can already be observed at this stage.

Artificial aging: The alloy is exposed to temperatures ranging from 150 to 280°C. At these temperatures diffusion of solute elements is activated and the supersaturated solid solution starts transforming into the two-phase equilibrium given by the phase diagram. However, this transformation follows a specific path in cast aluminum alloys as it transits through multiple metastable states before arriving at the final equilibrium. If we consider an alloy in which an equilibrium phase P is to precipitate from a supersaturated α-Al solid solution ($\alpha^{(1)}$), the precipitation sequence usually takes the following form:

$$\alpha^{(1)} \rightarrow \alpha^{(2)} + \text{Clusters/GP zones} \rightarrow \alpha^{(3)} + P'' \rightarrow \alpha^{(4)} + P' \rightarrow \alpha^{eq} + P$$

where $\alpha^{(i)}$ represent different composition sets of the α-Al solid solution leading up to α^{eq}, the equilibrium composition at the aging temperature. P'' and P' are metastable precursors to the stable P phase. These precursors are generally coherent or semi-coherent with the aluminum matrix contrary to the stable phase which is incoherent. Although from a thermodynamic point of view the equilibrium involving the P phase has a lower total free energy than its metastable precursors, the energy barrier for nucleation is lower for the coherent and semi-coherent metastable precursors. This makes the transition through these metastable phases kinetically advantageous, thus explaining the precipitation sequence.

The duration of the artificial aging is chosen so as to obtain the desired phases with the required volume fraction. This categorizes aging heat treatments into three types: under-aging, peak-aging and over-aging. The notion of peak hardness will be explained in the following section.

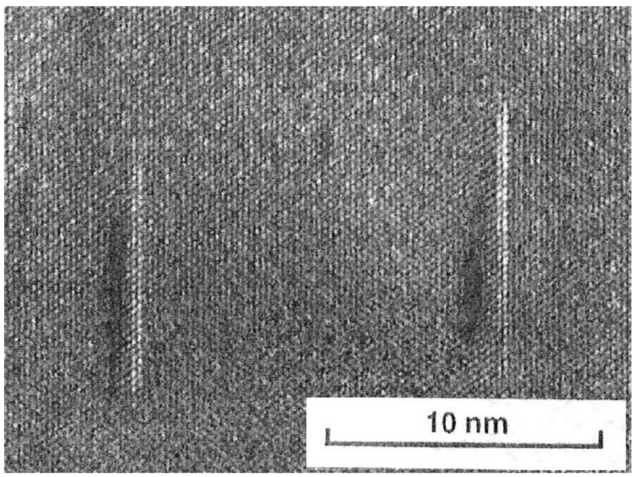

Figure 1.10 – High resolution transmission electron microscopy (HRTEM) micrograph showing Guinier-Preston zones in an Al-1.84%at. Cu [34].

Note that as a result of quenching, residual stresses are created in the material. The higher the cooling rate during quenching the higher these residual stresses. Artificial aging allows the relaxation of these residual stresses thus allowing for a better dimensional stability of the parts for the subsequent machining operations.

It is worth noting that these are the classical steps of the most widely used heat treatments in cast aluminum alloys for automotive applications. There are some heat treatments that replace quenching and subsequent aging with controlled air-cooling after solutionizing. It is also possible to perform two stage aging heat treatments at different temperatures triggering a second precipitation sequences and thus an additional hardening effect. Other heat treatments may also be limited to natural aging rather than artificial aging.

1.4.2 Peak hardness and nomenclature

During the aging treatment, a sequence of phase transformations takes place in the α-Al matrix. Right after quenching, the matrix is free of precipitates and only clusters/GP zones and solid solution strengthening contribute to the overall hardness. As shown in Figure 1.11, the hardness starts at a relatively low level because of the limited hardening capabilities of the GP zones which are easily sheared by dislocations (Figure 1.12). Figure 1.13a is a high resolution transmission electron microscopy (HRTEM) micrograph showing a sheared GP zone which appears like a step.

As the transformation continues, the coherent θ'' phase (a metastable precursor to the stable θ-Al_2Cu in Al-Cu alloys) starts to form and its volume fraction increases. The dimensions of this phase are larger than those of the GP zones and it precipitates in large numbers which renders shearing by dislocations more difficult thus raising hardness.

Then, the transition to the θ' phase takes place and the new precipitating phases start to lose coherence with the matrix and shearing becomes increasingly unlikely. Therefore, dislocations move across the precipitates according to a different mode known as the Orowan bypassing mechanism (Figure 1.12). Figure 1.13b is a HRTEM micrograph showing the cross section of a couple of metastable β' precipitates in an Al-Si-Mg alloy in the process of being bypassed by a dislocation according to the Orowan mechanism. These precipitates continue their growth and get increasingly further appart which decreases the stress necessary for a dislocation to glide through them as depicted by the size dependence in Figure 1.12.

The continued growth of precipitates at fixed volume fraction is known as Ostwald ripening and it consists of growth of large precipitates at the expense of the small ones. This phenomenon is driven by the reduction of the total free energy of the system by decreasing the total area of the precipitates/matrix interface. As ripening progresses, precipitates become larger and further apart which decreases their contribution to the hardness of the material. This process is accompanied by the final stage of the transformation, that of the formation of θ phase. At this point, coherence is lost entirely and hardness continues to decrease as a result of continued ripening.

A hardness peak is observable in Figure 1.11 which, for this 319 alloy, corresponds to the presence of the θ' phase. However, it is also possible for peak hardness to correspond to a mixture of two coexisting precursors to the stable phase [22]. A distinction between three types of aging heat treatments can therefore be made: under-aging (before peak hardness), peak aging (up to peak hardness) and over-aging (beyond peak hardness).

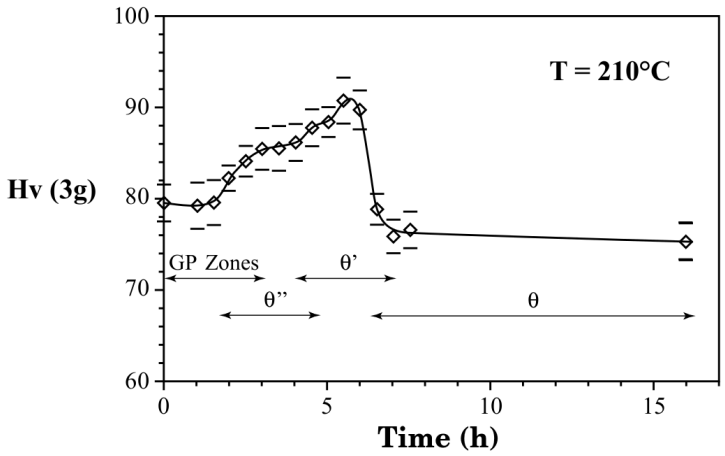

Figure 1.11 – Evolution of hardness in a 319 aluminum alloy as a function of aging duration at 210°C with the corresponding precipitation sequence [35].

The precipitation sequences taking place during different heat treatments are therefore fundamental for the evolution of mechanical properties. Heat treatments are designated with the letter "T" followed by differentiating digits. The most widely used heat treatments for cast aluminum alloys are described in the following:

- **T4:** solutionizing, quenching and natural aging,
- **T5:** controlled cooling after casting and artificial aging,
- **T6:** solutionizing, quenching and peak-aging,
- **T64:** solutionizing, quenching and under-aging,
- **T7:** solutionizing, quenching and over-aging.

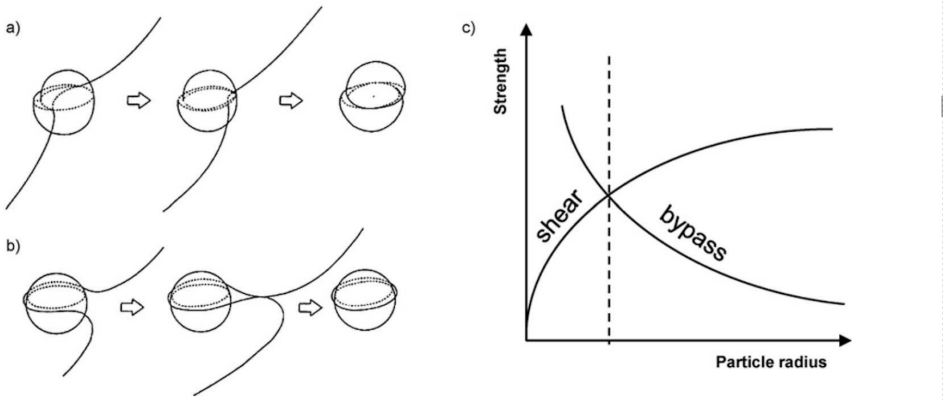

Figure 1.12 – Schematic representation of dislocation/precipitate interaction : (a) shearing, (b) bypassing and (c) the qualitative relationship between particle size and the stress necessary to activate each mechanism [36, 37].

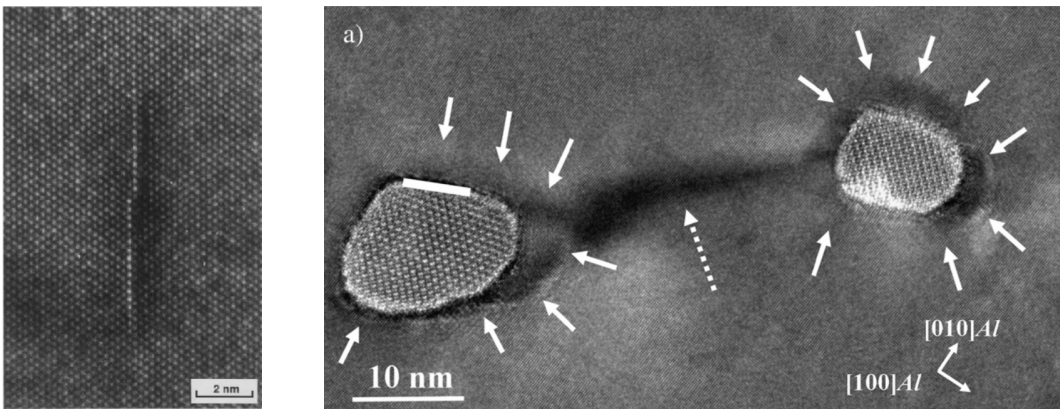

(a) (b)

Figure 1.13 – HRTEM micrographs showing precipitate crossing mechanisms : (a) sheared GP zone in an Al-1.84 at.% Cu alloy [38] and (b) dislocation bypassing two β'-Mg_2Si precipitates in an Al-Si-Mg alloy, the dislocation line is pointed to by the dotted arrow, the areas pointed to by solid arrows are the dislocation loops around the precipitates [39].

1.5 Precipitation sequences

In the previous section, a generic precipitation sequence was used for illustration. In this section the specific sequences for each cast aluminum alloy family will be specified according to various studies in literature.

1.5.1 Al-Si-Cu alloys

The pioneering studies revolving around precipitation hardening in aluminum alloys concerned the Al-Cu system [40]. In this alloy system the precipitation sequence is reported by Kelly *et al.* [41] as follows:

$$\alpha^{(1)} \rightarrow \alpha^{(2)} + \text{Clusters/GP zones} \rightarrow \alpha^{(3)} + \theta''\text{-Al}_3\text{Cu} \rightarrow \alpha^{(4)} + \theta'\text{-Al}_2\text{Cu} \rightarrow \alpha^{eq} + \theta\text{-Al}_2\text{Cu}.$$

Three types of Al-Cu precipitates are distinguished, each with its unit cell presented in Figure 1.14. In this system the key strengthening phases are θ'' and θ'. The crystallographic characteristics of the phases taking part in this sequence are summarized in Table 1.4. In these alloys, peak hardness is associated with either θ' or a mixture of θ' and θ''.

1.5.2 Al-Si-Mg alloys

For Al-Si-Mg alloys, the hardening phase system is β-Mg_2Si and it precipitates according to the following sequence reported by Shivkumar *et al.* [44] and Dutta *et al.* [45]:

Table 1.4 – Summary of the crystallographic characteristics of the phases belonging to the θ-Al_2Cu hardening system [42, 43].

Phase	Crystal structure	Coherency and orientation relationship with α-Al	Morphology
θ''-Al_3Cu	Bulk-centered tetragonal $a_{\theta''} = 0.404$ nm ; $c_{\theta''} = 0.768$ nm	Coherent $(001)_{\theta''}//(001)_\alpha$ $[100]_{\theta''}//[100]_\alpha$	Disks
θ'-Al_2Cu	Bulk-centered tetragonal $a_{\theta'} = 0.404$ nm ; $c_{\theta'} = 0.580$ nm	Coherent (broad faces) $(001)_{\theta'}//(001)_\alpha$ $[100]_{\theta'}//[100]_\alpha$ Semi-coherent (edges)	Plates
θ-Al_2Cu	Bulk-centered tetragonal $a_\theta = 0.607$ nm ; $c_\theta = 0.487$ nm	Incoherent	Plates

$$\alpha^{(1)} \rightarrow \alpha^{(2)} + \text{Clusters/GP zones} \rightarrow \alpha^{(3)} + \beta'' \rightarrow \alpha^{(4)} + \beta'\text{-Mg}_{1.8}\text{Si} \rightarrow \alpha^{eq} + \beta\text{-Mg}_2\text{Si} + \text{Si-phase.}$$

The sequence begins with magnesium-rich GP zones that quickly transform into the coherent β'' phase. This phase is reported by Mortsell *et al.* [46, 47] to have a chemical composition of $Mg_{6-x}Al_{1+x}Si_4$ with $0 \leqslant x \leqslant 2$. This phase is responsible for peak hardness of alloys of the A356 type.

Further aging leads to the formation of the semi-coherent β'. At this stage, other phases have been reported by other authours to either replace the β' phase or coexist it. The B' phase was observed by Edwards *et al.* [48] in an Al-0.80%Mg-0.79%Si-0.18%Cu and Miao *et al.* [49] observed the same phase in a 6022 wrought aluminum alloy. Furthermore, Andersen *et al.* [50, 51] reported the U1 and U2 phases in a 6082 wrought alloy. The exact precipitation sequence depends on the composition and heat treatment parameters (temperature, heating rate, duration). Finally, the incoherent stable phase β appears and replaces its metastable precursors. The crystallographic characteristics of the phases taking part in this sequence are summarized in Table 1.5. Figure 1.15 shows schematics of the unit cells of each one of the phases of the β system.

1.5.3 Al-Si-Mg-Cu alloys

The addition of copper to Al-Si-Mg alloys is known to have an accelerating effect on the precipitation kinetics of the β'' phase as well as increasing its volume fraction. Copper can also participate in the formation of a variety of quaternary phases. The precipitation sequence is therefore significantly more complex and many transition phases are still not completely distinguished and identified. Saito *et al.* [47] summarized the precipitation sequence for quaternary alloys as follows:

$$\alpha^{(1)} \rightarrow \alpha^{(2)} + \text{GP zones} \rightarrow \alpha^{(3)} + \beta'' + \text{L/C/QP/QC} \rightarrow \alpha^{(4)} + \beta' + \text{Q}' \rightarrow \alpha^{eq} + \text{Q.}$$

Perovic *et al.* [59] studied the precipitation sequence in Al-Mg-Si alloys where silicon is in excess in comparison to the copper additions. They proposed a simpler

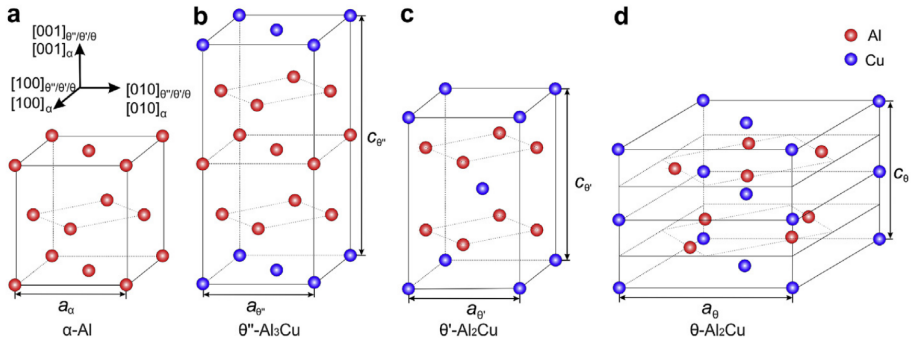

Figure 1.14 – Unit cells of FCC α-Al and the precipitates from the θ system [42].

Table 1.5 – Summary of the crystallographic characteristics of the phases belonging to the β-Mg_2Si hardening system [48, 49, 52, 53, 54, 55].

Phase	Crystal structure	Coherency and orientation relationship with α-Al	Morphology
β''-$Mg_{6-x}Al_{1+x}Si_4$ $0 \leqslant x \leqslant 2$	Monoclinic a = 1.516 nm ; b = 0.405 nm c = 0.674 nm ; β = 105.3°	Coherent $(010)_{\beta''}//(001)_\alpha$	Needles/rods
β'-$Mg_{1.8}Si$	Hexagonal a = b = 0.715 nm c = 0.405 nm	Semi-coherent $(001)_{\beta'}//(001)_\alpha$	Rods
β-Mg_2Si	Cubic a = 0.635 nm	Incoherent	Plates
B′-$Mg_9Al_3Si_7$	Hexagonal a = b = 1.04 nm c = 0.405 nm	Semi-coherent close to $(001)_{B'}//(001)_\alpha$	Lathes
U1-$MgAl_2Si_2$	Trigonal a = b = 0.405 nm c = 0.674 nm, $\gamma = 120°$	Semi-coherent $(100)_{U1}//(001)_\alpha$	Needles
U2-MgAlSi	Orthorhombic a = 0.675 nm ; b = 0.405 nm c = 0.794	Semi-coherent $(010)_{U2}//(001)_\alpha$	Needles

precipitation sequence for such alloys which is as follows:

$$\alpha^{(1)} \rightarrow \alpha^{(2)} + \text{Clusters/GP zones} \rightarrow \alpha^{(3)} + \beta'' \rightarrow \alpha^{(4)} + \text{Q}''(\lambda, \text{L}) + \beta' + \text{Q}' \rightarrow \alpha^{eq} + \text{Q}.$$

The crystallographic and morphological characteristics of the phases taking part in this sequence are summarized in Table 1.6.

Adding Cu to ternary Al-Si-Mg alloys reportedly improves them in a twofold manner. On the one hand, Cu increases the number density of β'' precipitates which allows the alloy to reach a higher hardness peak. On the other hand, Cu additions delays softening of the alloy during service at high temperatures. It does

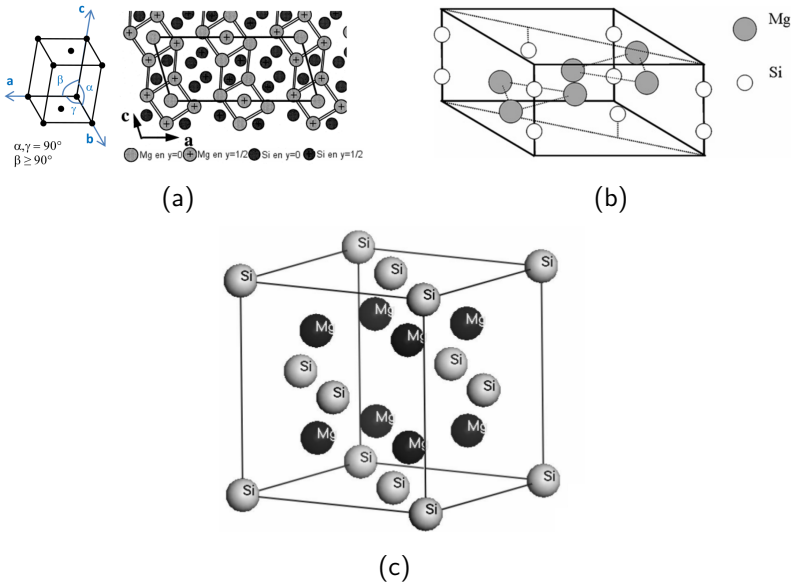

Figure 1.15 – Unit cells of the precipitates from the β system : (a) β'' [56], (b) β' [57, 50] and (c) β [58].

so by altering the precipitation sequence which provides more thermally stable Cu-containing hardening phases (Q′, Q, etc..) [46]. When an alloy is over-aged, the hardening phase dominance transitions from the β system to the Q system. This delays the softening effect of ripening and the transition to the stable and incoherent phases stage of the precipitation sequence.

The unit cells of Q and Q′ are identical and differ only slightly in parameter values. A representation of this unit cell is shown in Figure 1.16.

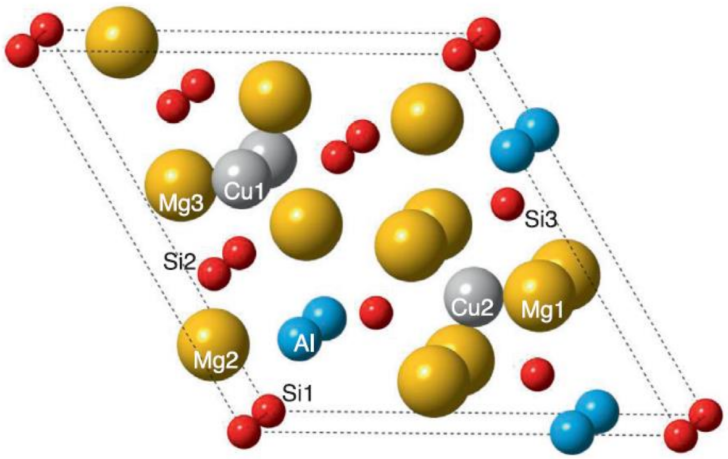

Figure 1.16 – Unit cell of Q and Q′ [62].

Table 1.6 – Summary of the crystallographic characteristics of the phases belonging to the Q-phase hardening system [60, 54, 55, 61].

Phase	Crystal structure	Coherency and orientation relationship with α-Al	Morphology
Q′-$Al_3Cu_2Mg_9Si_7$	Hexagonal a = 1.032 nm , c = 0.405 nm ; $\gamma = 120°$	Semi-coherent $(001)_{Q'}//(001)_\alpha$	Lathes
Q-$Al_3Cu_2Mg_9Si_7$	Hexagonal a = 1.039 nm c = 0.4017 nm ; $\gamma = 120°$	Incoherent	Lathes
L	Disordered	-	Lathes
QP and QC	Hexagonal	Semi-coherent	Lathes
C-$Mg_4AlSi_{3.3}Cu_{0.7}$	Monoclinic a = 1.032 nm ; b = 0.405 nm c = 0.810 nm ; $\beta = 100.9°$	Semi-coherent	Plates

1.6 Conclusion

Cylinder heads are very complex parts of the internal combustion engine and are therefore manufactured using casting processes. These parts are also the most heavily stressed both mechanically and thermally. Aluminum alloys of series 3xx have multiple properties that make them suitable for cylinder head applications. In relationship to the manufacturing process, alloys of this series have good a low melting temperature, good castability and machinability, low shrinkage and adequate hot-tear resistance. Regarding behavior, aluminum alloys have a high thermal conductivity thus improving the efficiency of cooling and they possess good mechanical properties.

The necessary in-service mechanical properties for the cylinder head application are obtained as a result of appropriate heat treatments. These heat treatments trigger precipitation sequences which produce microstructures rich in fine and finely dispersed metastable precipitates. Each family of alloys is characterized by a specific precipitation sequence. For an alloy of type A356+0.5Cu, hardening is ensured mainly by the β-Mg_2Si hardening system and, for long aging heat treatment durations, by the Q-phase system.

In the next chapter, the studied alloy of type A356+0.5Cu will be presented.

The results of the transmission electron microscopy study conducted on it at different aging conditions will be presented. This microstructural characterization will be complemented by a tensile test campaign which will associate microstructure to mechanical behavior.

Chapter 2

Experimental study of the A356+0.5Cu alloy

Résumé

L'alliage de cette étude est du type A356+0.5Cu. Dans ce chapitre, cet alliage ainsi que les résultats de la campagne expérimentale de son comportement en vieillissement sont présentés. Des échantillons ont été coulés et ils ont été assujettis à un traitement thermique de mise en solution, trempe à l'eau et revenu à 200°C pour des durées différentes (0.1, 1, 10 et 100 heures).

Ces échantillons ont été examinés par MET afin d'étudier la séquence de précipitation ayant lieu et d'obtenir des distributions de tailles expérimentales. Ces dernières ont été utilisées par la suite dans la validation et la calibration du modèle de précipitation.

Finalement, des essais de traction ont été effectués pour ces conditions de vieillissement afin d'obtenir l'évolution de la limite d'élasticité de l'alliage en fonction de la durée du revenu à 200°C. Ces résultats ont été utilisés par la suite pour la validation et la calibration du modèle d'estimation de la limite d'élasticité.

2.1 Studied alloy: A356+0.5Cu

The studied alloy is a primary Al-Si-Cu-Mg alloy of type A356+0.5Cu, the chemical composition of which is presented in Table 2.1. The real composition was measured using spark ionization mass spectrometry and was averaged over multiple areas in a sample. This is a comparatively low-alloyed cast aluminum alloy with less than 1%wt. total additions (Si excepted). This prevents the loss in thermal conductivity which can be observed in other alloys such as the 319 alloy containing more than 3%wt. Cu [63]. As mentioned in the previous chapter, this quaternary alloy has a higher hardness peak and an improved resistance to softening thanks to Cu additions.

The phase diagram of the alloy was computed by Thermo-Calc using the TCAL5 database. Figure 2.1 shows a plot of the volume fraction of the different phases as a function of temperature. The solidus temperature is 562°C and the liquidus temperature is 607°C . The solvus temperature of the β-Mg_2Si is 446°C , thus defining the solutionizing heat treatment temperature window between 446 and 562°C . Solvus temperatures of the phases in the diagram as given by the Thermo-Calc are compared to values from literature in Table 2.2. This serves as validation of the representativeness of the TCAL5 database regarding the studied alloy system.

Figure 2.1 shows that up to temperatures as high as 407°C , the Q-phase is the stable phase, which is commensurate with the precipitation sequence reported in literature. It can also be observed that the θ-Al_2Cu phase can coexist with the Q-phase at low temperatures ($<$266°C).

Table 2.1 – Chemical composition of the studied A356+0.5Cu alloy in %wt.

	Si	Cu	Mg	Sr	Fe	Ti	Other
Nominal	7	0.5	0.3	0.01	< 0.15	< 0.15	< 0.1
Measured	6.63	0.52	0.36	0.0067	0.114	0.136	0.054

Table 2.2 – Comparison between calculated solvus temperatures of phases using the TCAL5 database and experimental values from literature.

Phases	Solvus temperature of phase (°C)		References
	TCAL5	Literature	
β-$Al_9Fe_2Si_2$	566	567.2	[6, 64]
Si	568	577.9	[65]
Q-phase	407	421.5	[35]
β-Mg_2Si	446	441.3	[66]

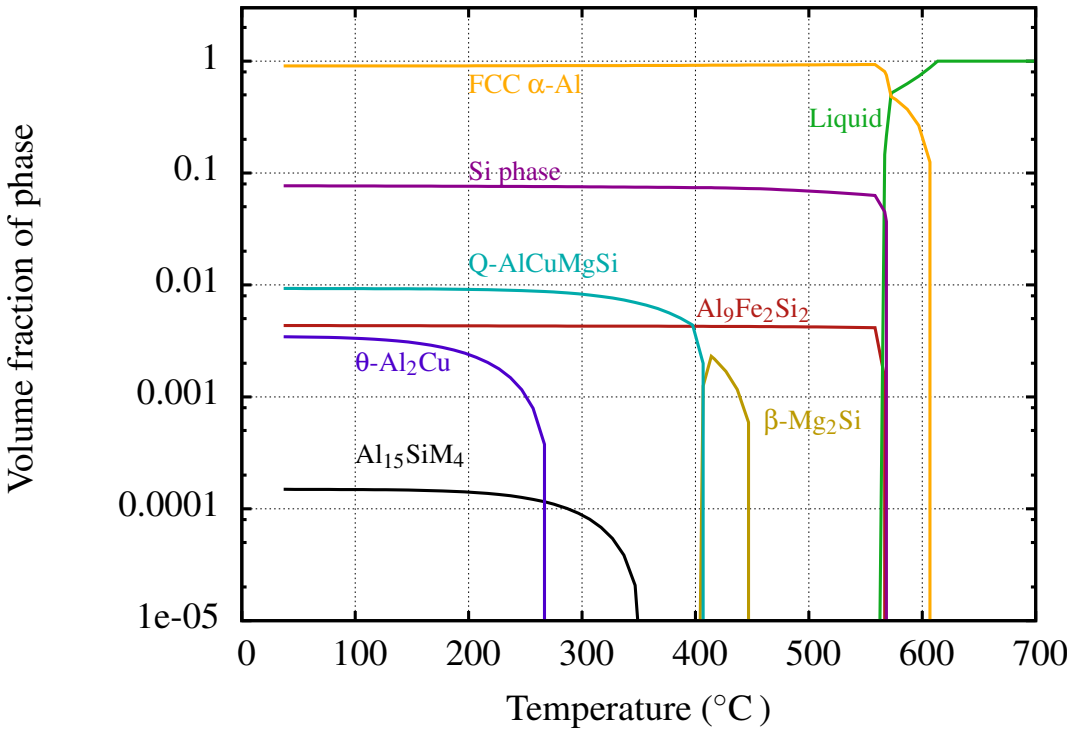

Figure 2.1 – Volume fraction of phases as a function of temperature for an A356+0.5Cu alloy calculated with Thermo-Calc using the TCAL5 database.

2.2 Specimen preparation

The studied alloy was characterized using TEM and tensile tests. The objectives of this experimental work are in summary:

1. Investigating the precipitation sequence occuring in the alloy when it undergoes an aging heat treatment.
2. Produce statistically viable experimental size distributions of precipitates to be compared to the simulations in order to calibrate and validate the precipitation model.
3. Measure yield strength at different aging conditions to be compared to the simulations in order to calibrate and validate the yield stress model.

The samples were extracted from AFNOR[1] normalized cast aluminum alloy specimens (Figure 2.2). They were then solutionized for 5 hours at 540°C, water quenched and artificially aged at 200°C for durations of 0.1, 1, 10 and 100 hours. The solutionizing heat treatments were conducted in a salt bath (60%wt. KNO_3 + 40%wt. $NaNO_2$), while the artificial aging treatments were conducted in an oil bath. The use of baths for the heat treatments allows a more efficient and homogeneous heat transfer.

[1] *AFNOR: Association Française de NORmalisation* (French Normalization Association)

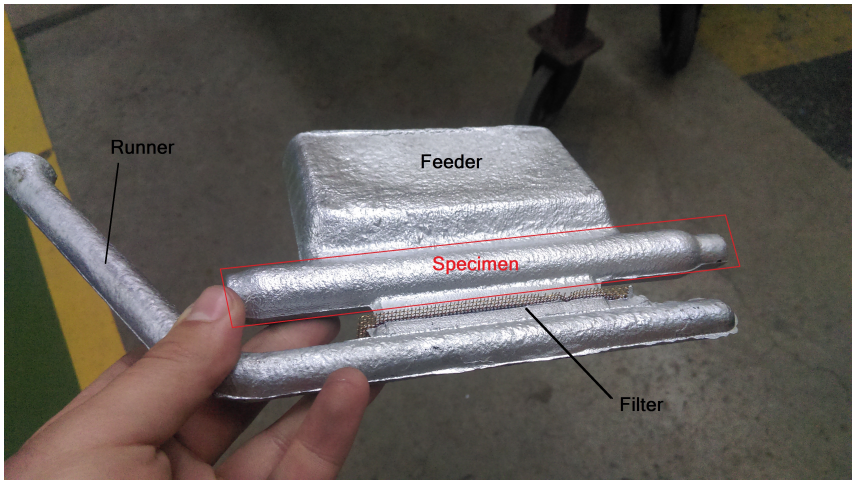

Figure 2.2 – AFNOR cast aluminum alloy specimen in the experimental study.

2.3 Precipitates characterization

2.3.1 Experimental procedure for TEM study

For each one of the studied aging conditions, small sheets were extracted from the bulk samples. The TEM foils were then cut from these thin sheets and mechanically polished to a thickness of 80-100 μm. Finally, the samples were twin-jet polished.

Jet polishing was performed in a 30% nitric acid + 70% methanol solution, at 15 V in a temperature ranging from -30 to -40°C . The thin foils were examined in a Philips CM-12 transmission electron microscope operated at 120 kV. These observations were performed at the Canadian Centre for Electron Microscopy (CCEM) of McMaster University in Hamilton Ontario. The contributions of Xiang Wang in the observations and detailed reports are greatly appreciated.

Contrary to the stable phases, the metastable phases are known to be either coherent or semi-coherent with the aluminum FCC matrix. These phases form on the $\{100\}$ planes of FCC aluminum solid solution (Tables 1.4, 1.5 and 1.6). Therefore, in order to observe them using TEM, the aluminum matrix was oriented along a $\langle 001 \rangle_\alpha$ zone axis. Figure 2.3 presents a drawing of an elementary cube of the aluminum matrix containing rod-shaped precipitates, oriented along the $\langle 001 \rangle$ directions. In the viewing direction, the precipitates can either be seen as round cross sections or elongated edge sections.

It is worth noting that this has been particularly challenging in this Si-rich alloy. This is due to the scarcity of sufficiently thin areas the orientation of which is close enough to $\langle 001 \rangle_\alpha$. The high volume fraction of the eutectic constituent in the alloy is responsible for the substandard quality of the electrolytic jet polishing results. Figure 2.4 shows a comparison between the resulting jet polished areas for the studied A356+0.5Cu alloy and a typical 6xxx series wrought alloy containing significantly less Si.

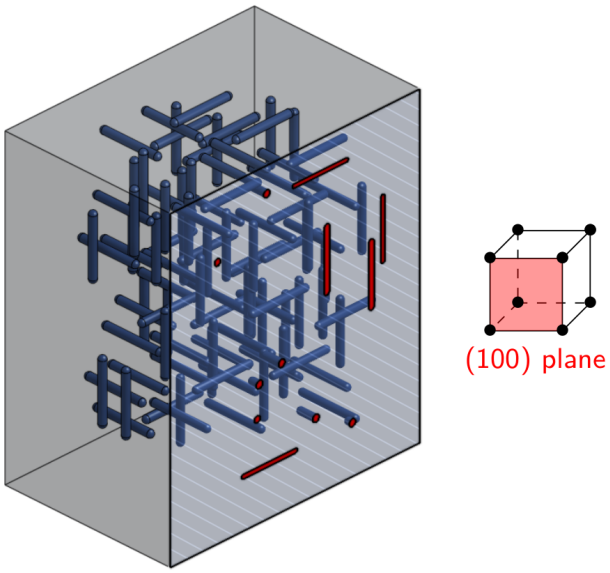

Figure 2.3 – Schematic of the expected morphology and orientation of the precipitates as observed with TEM along a $\langle 001 \rangle_\alpha$ zone axis.

2.3.2 Nature and morphology of precipitates

Figure 2.5 presents bright field and dark field micrographs as well as the corresponding selected area diffraction (SAD) patterns for samples aged 0.1 hr at 200°C with a $\langle 001 \rangle_\alpha$ zone axis. A large number of very fine homogeneously distributed precipitates are observed thanks to their roughly circular cross sections. The corresponding SAD patterns exhibit streaks of diffuse spots parallel to the $\langle 100 \rangle_\alpha$ and $\langle 010 \rangle_\alpha$ directions. The fine precipitates and the SAD pattern are commensurate with coherent rod-shaped short β'' precipitates oriented along $[100]_\alpha$ directions.

Although the SAD patterns point to the presence of short elongated precipitates, their edge sections are not observable on the micrographs. It is worth noting that the chemical composition of the β'' phase has an average atomic number close to that of aluminum. Thus, chemical contrast is almost inexistant. The edge sections of precipitates are visible mostly thanks to the coherence strain field around the precipitates which is due to the misfit between them and the aluminum matrix. Since the artificial aging for these samples lasted only 6 minutes, the precipitates are still in the early formation stage and their length is small. This results in a low strain field around them which makes the contrast too low to be observable. It is to be acknowledged that the possibility of the presence of spherical GP zones at such an early stage of precipitation cannot be entirely overruled.

In the samples aged for 1 hr, a large number of fine homogeneously distributed precipitates is observed (Figure 2.6). The corresponding SAD patterns exhibit streaks of sharp spots parallel to the $\langle 100 \rangle_\alpha$ directions. The precipitates are rod-shaped β'' precipitates oriented along $[100]_\alpha$ directions.

In these images, precipitates are presented as roughly circular cross sections and

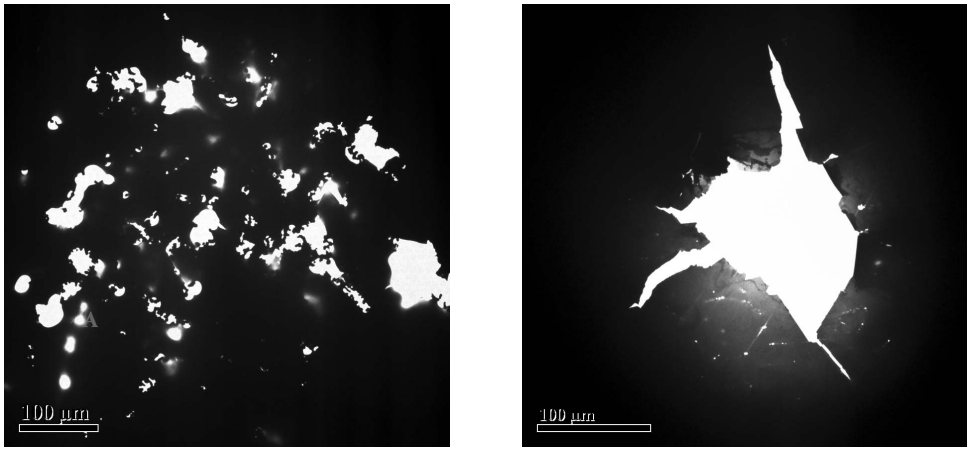

(a) (b)

Figure 2.4 – Micrographs showing the result of electrolytic jet polishing : (a) in the studied A356+0.5Cu alloy and (b) in a typical 6xxx series wrought alloy containing less Si.

elongated edge sections. The longer duration of the artificial aging in this condition allows further growth of the precipitates. Thus, the length of these precipitates is sufficient for there to be a strong enough strain field contrast allowing their observation.

After aging for 10 hours at 200°C , a large number of relatively coarser and homogeneously distributed precipitates are observed (Figure 2.7). The precipitates are rod-shaped β'' precipitates oriented along $[100]_\alpha$ directions.

A different type of precipitates can be observed in significantly smaller number. These lath-shaped precipitates are recognized by their rectangular cross sections (BF images) and their comparatively bigger lengths (DF images). These precipitates are believed to be the Q′/Q″ phases.

A more complex microstructure is observed after aging for 100 hrs. Observations were performed along a near $\langle 001 \rangle_\alpha$ zone axis and they show a majority of fine lath-shaped precipitates with a roughly rectangular cross sections (Figure 2.8). Two alignment families can be observed: a majority of precipitates oriented at 10° to 12° away from $\langle 001 \rangle_\alpha$ directions, and a minority of precipitates oriented along the habit $\langle 001 \rangle_\alpha$ directions (pointed to in Fig. 2.8a). The SAD patterns (Figures 2.8g and 2.8h) are in accordance with the simulated SAD pattern for the Q′ phase (Fig. 2.8i). Phases similar to the minor phase were observed in an AA6111 [67] and an Al-Si-Mg alloy with high Cu content [68] and were identified as Q″ and L respectively. Due to their small size, quantitative EDS measurements on these precipitates is not attainable since signal from the surrounding matrix is also picked up. Qualitatively however, as displayed in Figure 2.9, it can be seen in comparison to the matrix that these phases are rich in Al, Si, Mg and Cu. Thus, based on all these elements of observation, these lath precipitates are identified as majoritarily the Q′ phase coexisting, in smaller numbers, with the Q″ phase.

Rod-shaped small precipitates are still observable but in significantly fewer

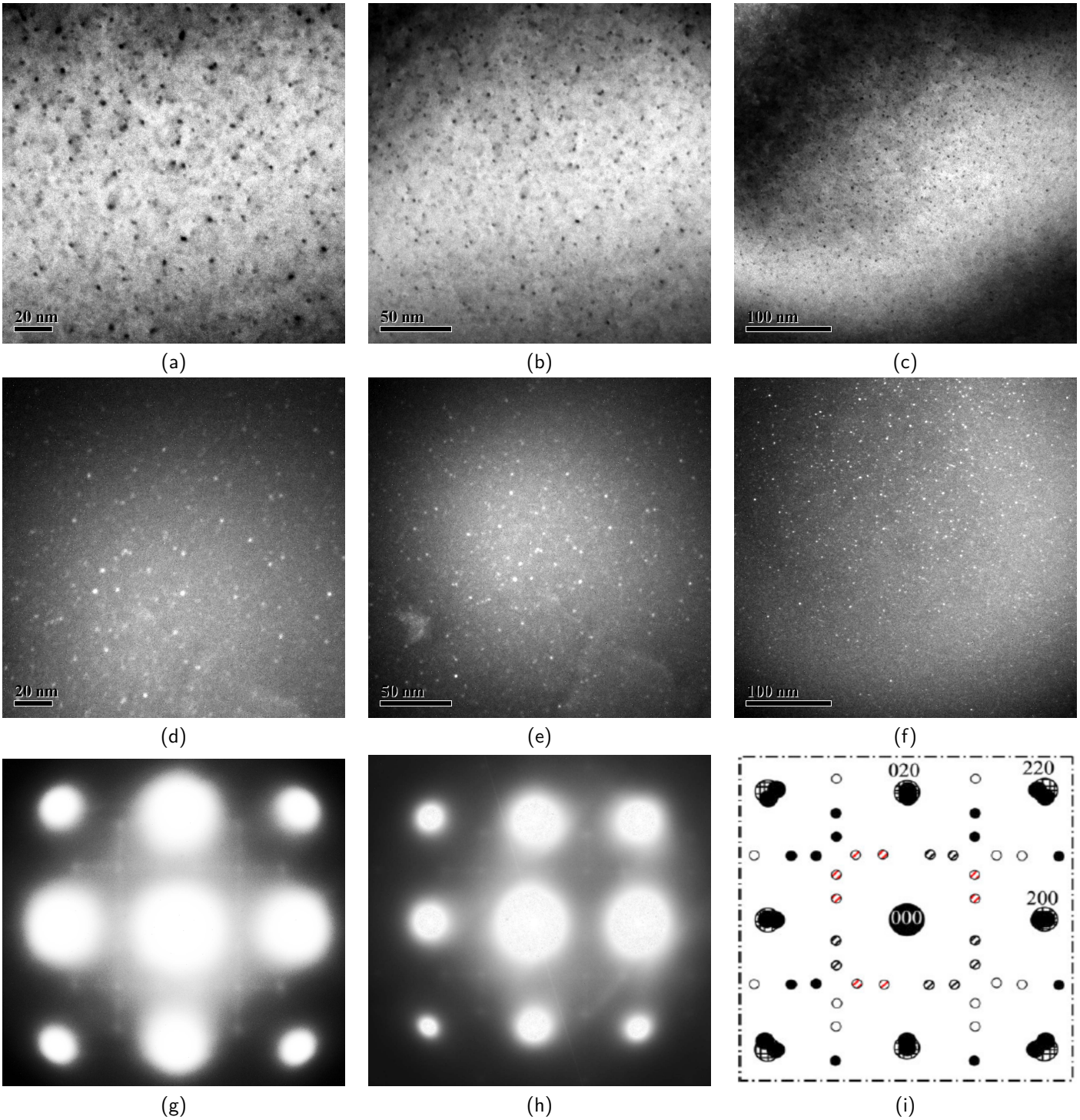

Figure 2.5 – TEM observations along the $\langle 001 \rangle_\alpha$ zone axis for samples aged 0.1 hr at 200°C (a) through (c): bright field images (d) through (f): dark field images (g) through (i): SAD patterns and the simulated pattern for β''.

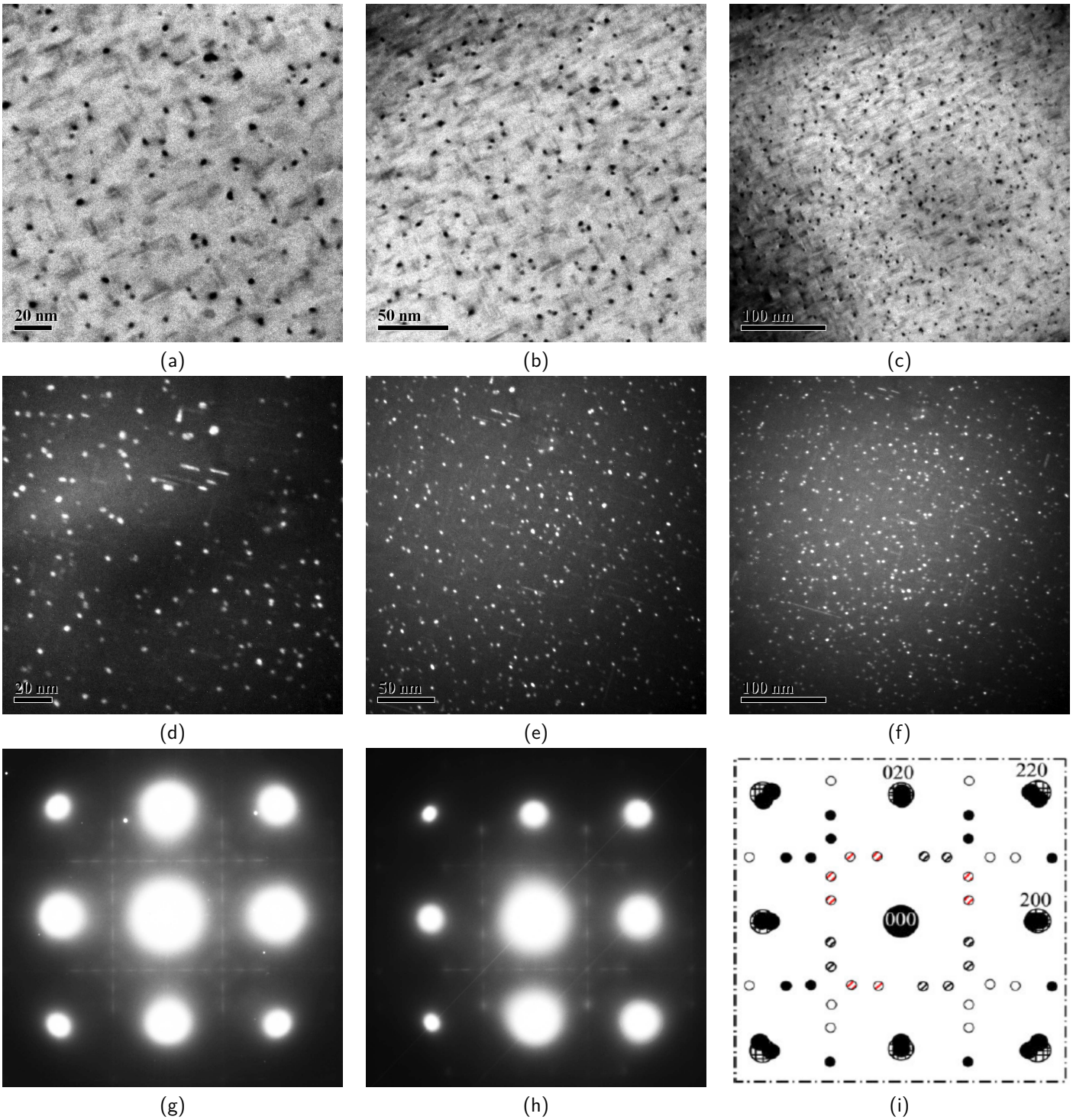

Figure 2.6 – TEM observations along the $\langle 001 \rangle_\alpha$ zone axis for samples aged 1 hr at 200°C (a) through (c): bright field images (d) through (f): dark field images (g) through (i): SAD patterns and the simulated pattern for β''.

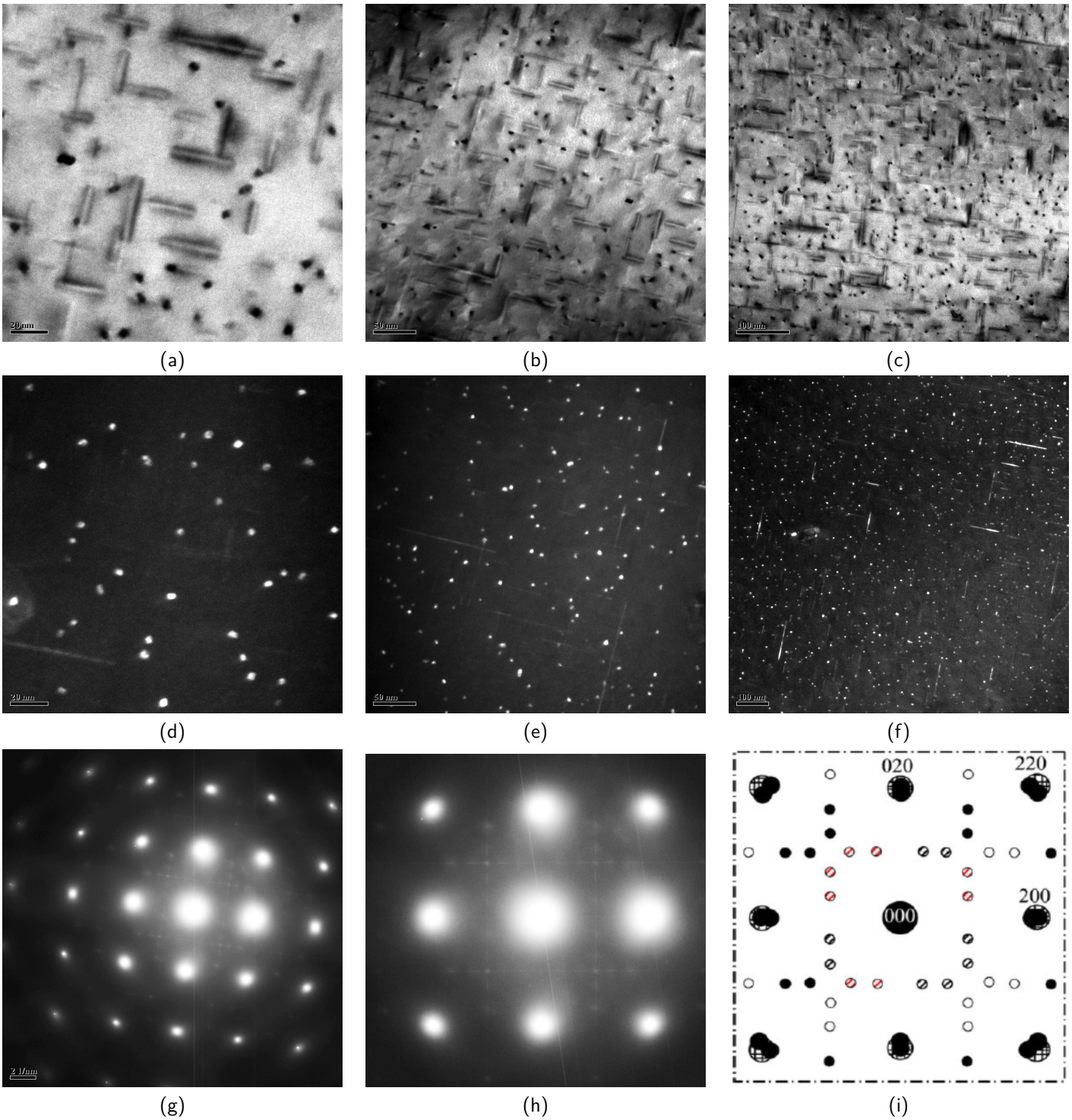

(a) (b) (c)

(d) (e) (f)

(g) (h) (i)

Figure 2.7 – TEM observations along the $\langle 001 \rangle_\alpha$ zone axis for samples aged 10 hrs at 200°C (a) through (c): bright field images (d) through (f): dark field images (g) through (i): SAD patterns and the simulated pattern for β''.

Table 2.3 – Summary of precipitate predominance for each aging condition in the studied A356+0.5Cu alloy.

Duration of aging at 200°C (hr)	β''	Q′/Q″
0.1	++++	Not observed
1	++++	Not observed
10	++++	+
100	+	++++

numbers. Their scarcity is also reflected by the absence of their trace in the SAD pattern.

In general, the aforementioned precipitates appear to be homogeneously distributed. Nevertheless, evidence of heterogeneous precipitation can be seen on multiple instances presented in Figure 2.10. Precipitates appear aligned in "string" which suggests preferential nucleation on dislocation lines.

In addition to the fine precipitates, coarse precipitates of different morphologies are observed (Fig. 2.11). Elongated, cuboidal, globular and irregular shapes are present. EDS spectra of such coarse precipitates shows high Si content (Fig. 2.12). Further SAD analysis and indexation allowed the identification of the Si diamond structure. It was concluded that these coarse precipitates are the Si phase.

2.3.3 Size distributions of precipitates

In addition to the identification of the nature of precipitates, quantitative measurements were carried out in order to obtain experimental size distributions for different aging conditions. These size distributions were used to calibrate and validate the precipitation kinetics model that was developed in this study. Table 2.3 presents a summary of precipitate predominance for each aging condition.

Length and diameter distributions for rod-shaped β'' precipitates were made for samples aged at 200°C for 0.1, 1 and 10 hrs. Length, width and thickness distributions for lath-shaped Q′ precipitates were made for samples aged for 100 hrs. It is important to note that it was not possible to measure the dimensions in more than one direction for the same precipitate due to their morphology and orientation. Thus, an average aspect ratio for precipitates cannot be extracted from this data. It is then the mean aspect ratio of the average measured precipitate in each distribution that was used in the model.

The TEM images were imported into commercial ImageJ software. After calibration, precipitate dimensions were measured manually and saved to produce size distributions. The distributions are expressed as number fractions with respect to size bins of equal amplitude. Table 2.4 presents the type of TEM images used for the measurement of each dimension, and the number of measured precipitates to produce valid statistics for each one of them. For each size distribution, a total number ranging from 285 to 520 precipitates were measured.

Table 2.5 references the experimental size distribution of rod-shaped β'' for

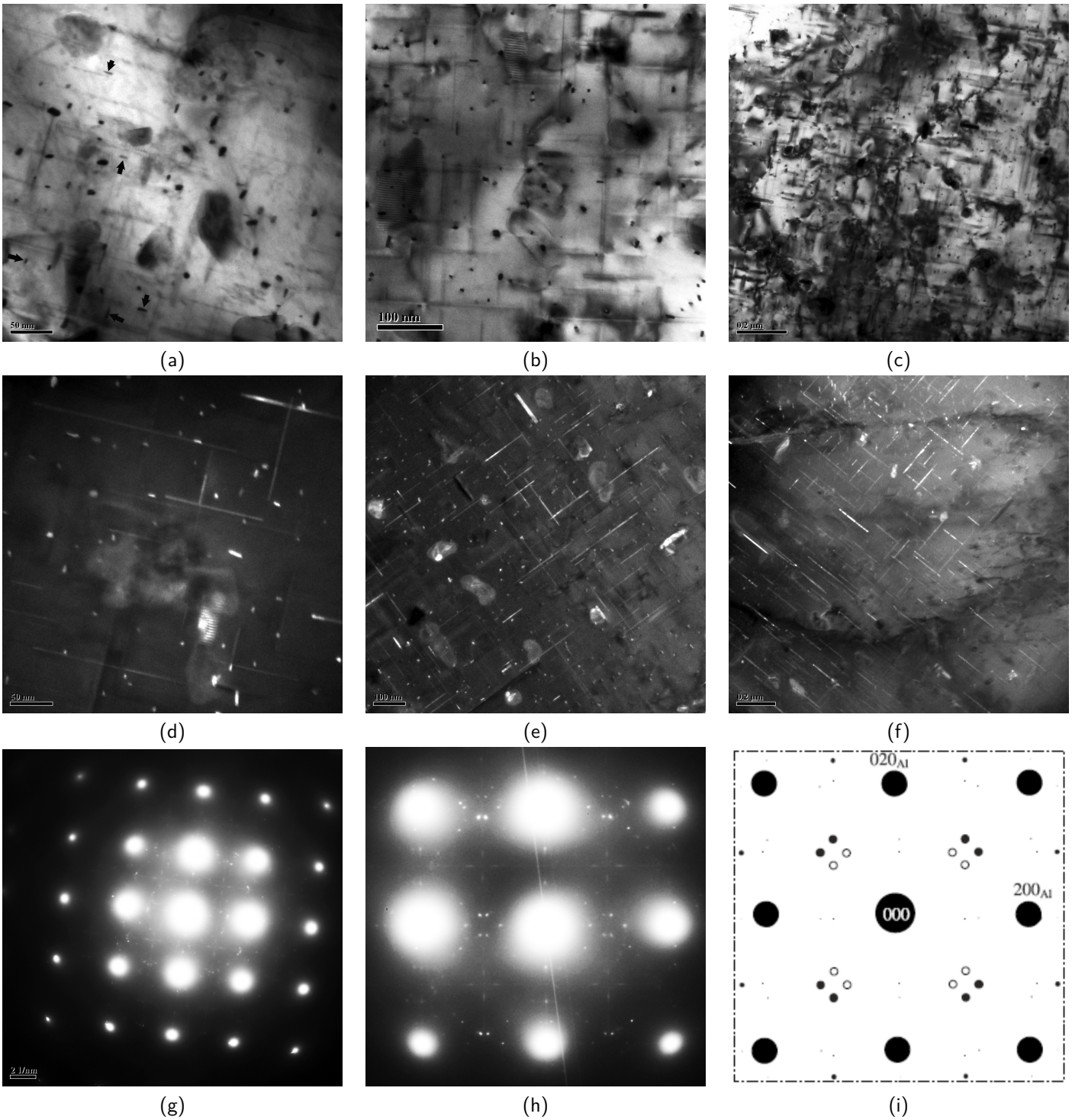

Figure 2.8 – TEM observations along the $\langle 001 \rangle_\alpha$ zone axis for samples aged 100 hrs at 200°C (a) through (c): bright field images (d) through (f): dark field images (g) through (i): SAD patterns and the simulated pattern for Q′.

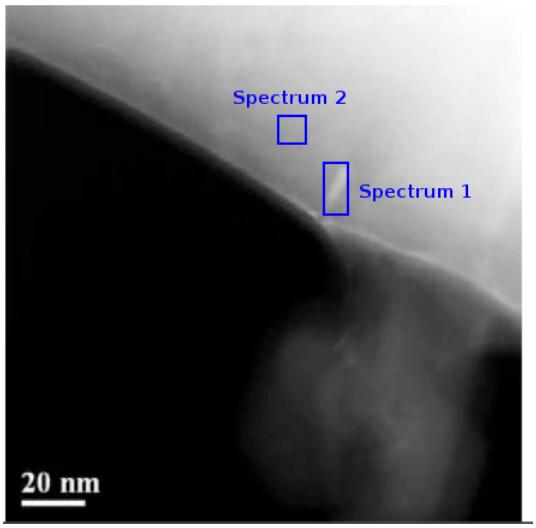

at. %	Mg	Si	Cu	Al
Precipitate (spectrum 1)	5.5	7.2	2.4	85
Matrix (spectrum 2)	0.7	2.4	1.4	95.4

Figure 2.9 – EDS analysis of phase composition for the matrix and fine precipitate in sample aged for 100 hrs at 200°C .

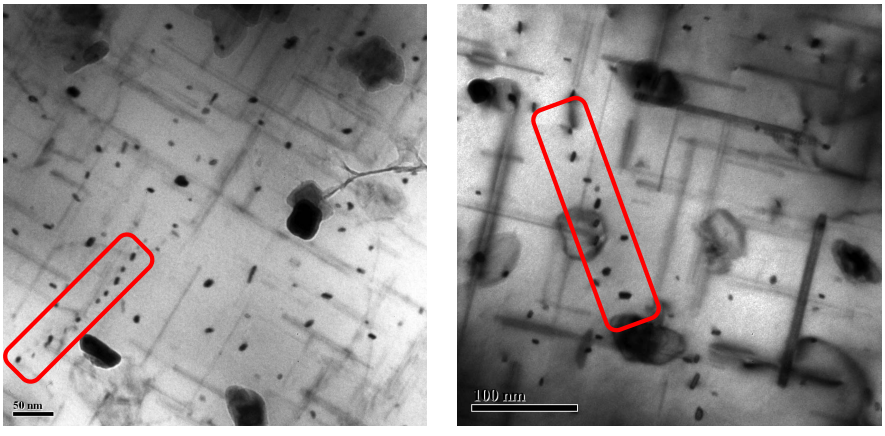

(a) (b)

Figure 2.10 – Bright field images of heterogeneously distributed precipitates in sample aged 100 hrs at 200°C .

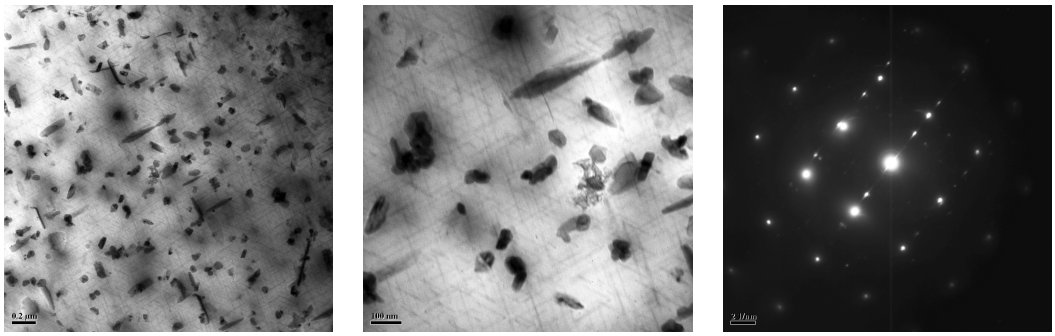

(a) (b) (c)

Figure 2.11 – Bright field TEM images of coarse Si phase precipitates and the corresponding SAD pattern.

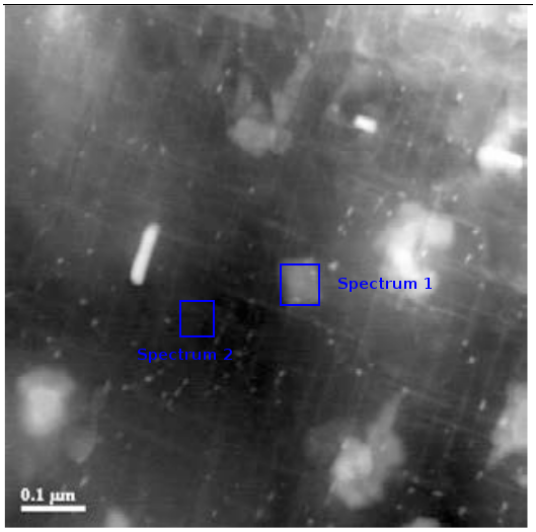

at. %	Mg	Si	Cu	Ti	Al
Precipitate (spectrum 1)	0.4	9	0.6	0.2	90
Matrix (spectrum 2)	0.8	0.6	1	0.2	97

Figure 2.12 – EDS analysis for the matrix and a coarse cuboidal precipitate in sample aged 100 hrs at 200°C .

Table 2.4 – Details of the procedure of measurement of precipitate size distributions.

Duration of aging at 200°C (hrs)	Precipitate	Dimension	TEM images used	Number of measurements
0.1	β'' rods	Diameter	DF	305
		Length	-*	-*
1	β'' rods	Diameter	DF	520
		Length	BF	343
10	β'' rods	Diameter	DF	445
		Length	BF	323
100	Q′ laths**	Width	DF	443
		Thickness	DF	463
		Length	DF	285

* length of β'' precipitates could not be measured for this condition due to insufficient strain field contrast

** for samples aged 100 hrs at 200°C , the predominant precipitates are Q′ and very few β'' precipitates could be observed

each sample in terms of diameter and length, with the exception of length for samples aged for 0.1 hr for reasons previously discussed. As aging duration becomes longer, the growth process moves the size distributions towards higher sizes. It is also noticeable that the distributions widen and flatten as aging duration increases. The average diameter evolves from 1 nm for an aging duration of 0.1 hr to 2.8 nm for 10 hrs, and the average length evolves from 10.7 nm for an aging duration of 0.1 hr to 20 nm for 10 hrs (Table 2.6). The aspect ratio of the average precipitate shows a slight evolution from 6.3 to 7.1.

Figure 2.13 references the experimental size distribution of lath-shaped Q′ precipitates for samples aged for 100 hrs at 200°C in terms of thickness, width and length. The distributions appear to have a log-normal shape with thickness, width and length averages of 3.1, 6.0 and 84 nm.

2.4 Tensile tests

2.4.1 Experimental procedure

The tensile tests were carried out on the studied A356+0.5Cu alloy for the same aging conditions that were investigated using TEM. The heat treated samples were machined to confer to them the designed geometry.

The tests were performed on a MTS servo-hydraulic tensile test machine of the mechanical testing laboratory of the department of materials engineering at UBC. The samples and the grips used to secure them to both ends of the machine were designed specifically for these tests. The test sequence was displacement-

Table 2.5 – Experimental size distributions of β'' precipitates in the studied A356+0.5Cu aged for 0.1, 1 and 10 hrs at 200°C .

Aging duration (hrs)	Diameter statistics (bin size = 0.2 nm)	Length statistics (bin size = 2.0 nm)
0.1	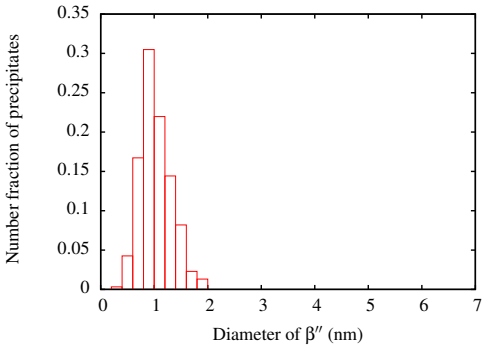	Unavailable
1	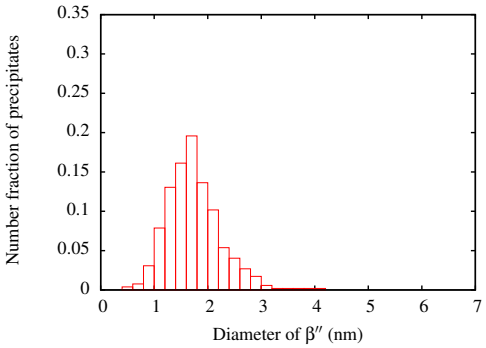	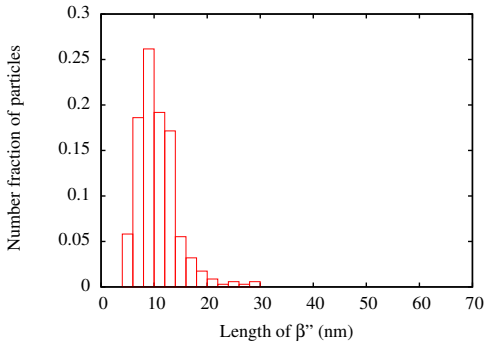
10	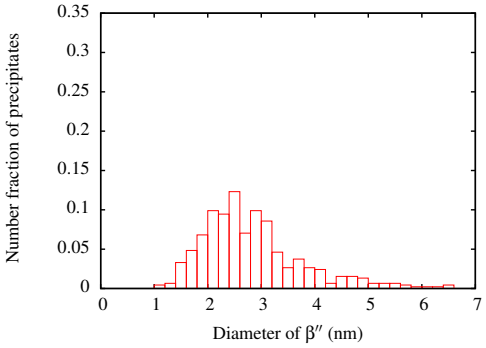	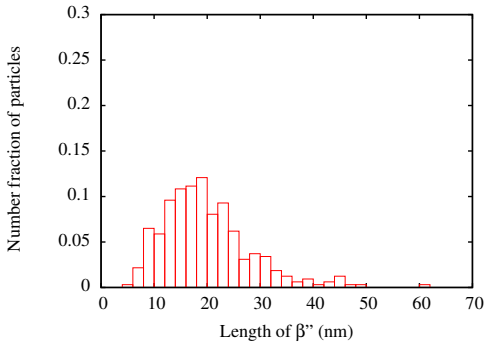

Table 2.6 – Aspect ratio of the average β'' precipitate.

Aging duration at 200°C (hrs)	Average length $< L >$ (nm)	Average diameter $< D >$ (nm)	Aspect ratio , $\lambda = \frac{<L>}{<D>}$
0.1	-	1.0 (std=0.3)	-
1	10.7 (std=3.8)	1.7 (std=0.5)	6.3
10	20.0 (std=8.3)	2.8 (std=0.9)	7.1

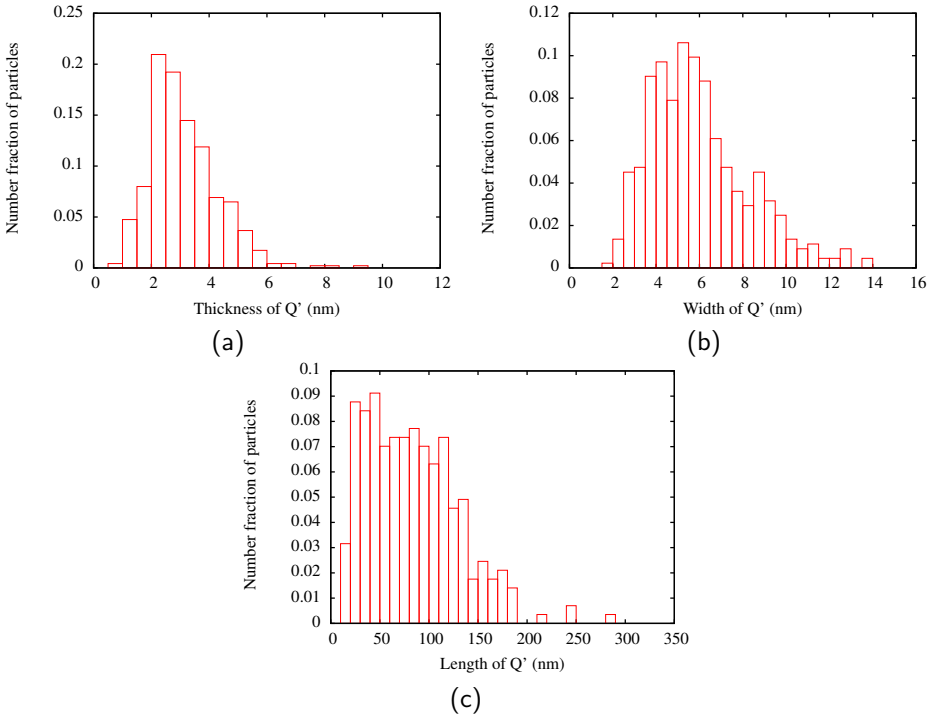

Figure 2.13 – Experimental size distributions of Q′ precipitates in the studied A356+0.5Cu alloy aged 100 hrs at 200°C ; bin sizes for thickness, width and length are 0.5, 0.5 and 10 nm respectively.

controlled at a rate of 0.06 mm/s. A reduced section diameter of 6 mm was chosen to eliminate any potential scale effects and obtain representative data. A 3D model of the setting (sample+grips) as well as a drawing of the sample is presented in Figure 2.14.

For each heat treatment condition, tests at three temperatures were carried out : room temperature, 100 and 200°C . Each test was repeated three times for statistical validity. Therefore, a total of 36 tests were carried out.

The machine was equiped with two heating cells on each end, both operated by PID controllers. The sample is then conduction heated and its temperature is continuously tracked thanks to attached thermocouples. For the sake of thermal isolation, the sample is wrapped with a thick layer of fiber glass wool. The tests were started as soon as target temperature is reached in the sample. Reaching target temperatures lasted three to six minutes and the tests themselves laster under a minute. This was taken into account when comparing the results of these tensile tests to the model output.

Data from the load cell and the position sensor in the hydraulic piston was acquired. For the room temperature tests, since no thermal insulation was needed, an extensometer was used to track sample strain. For the tests at 100 and 200°C , temperature was also recorded.

An example of a raw data plot is given in Figure 2.15a. The data for which the load is lower than 1 kN are omitted, seeing as one can observe effects due to

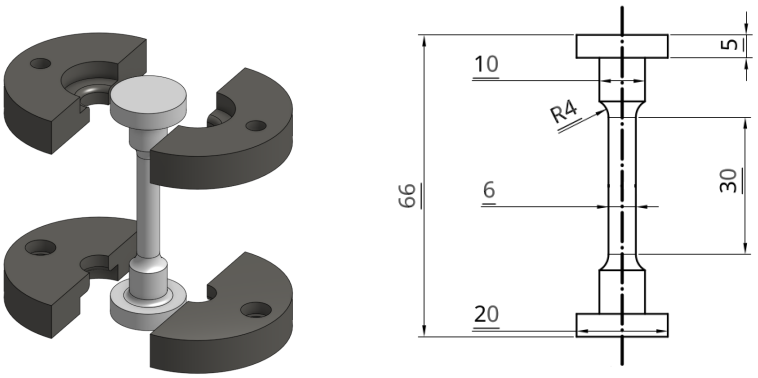

(a) (b)

Figure 2.14 – Tensile test sample geometry : (a) 3D model of the setup showing the sample with the specially designed grips and (b) drawing of the sample.

sample seating in the grips in the start of the test. The cleaned up data plot is given in Figure 2.15b. This data consists in shifting the raw data curve by the initial position and shifting it again once data below 1 kN is removed.

More importantly, the engineering stress-strain curves (Figure 2.15c) were corrected for machine and grips compliance following equation 2.1:

$$\Delta l_s = \Delta l_m - F \times M_c. \tag{2.1}$$

Where Δl_s is the actual sample elongation, Δl_m is the measured elongation, F is the load, and M_c the machine+grips compliance given by equation 2.2:

$$M_c = \frac{Ks - K}{K \times Ks} \tag{2.2}$$

where K_s is sample stiffness, K the sample+machine+grips stiffness (measured on load-position curves).

Values for K_s were chosen so as to give measured Young Moduli in accordance with the FCC metals properties review by Frost and Ashby given in Appendix A. Considering a melting temperature of 886 K (provided by Thermo-Calc/TCAL5) and a Poisson ratio of 0.334 these values are 68, 65 and 61 GPa for 20, 100 and 200°C respectively.

The 0.2% offset proof stress was then measured and is used as the comparison value to the model (Figure 2.15d).

2.4.2 Test results

Figure 2.16 shows the engineering stress/strain curves for the tensile tests conducted at room temperature. When aged for 0.1 hr at 200°C , the alloy yields at a relatively low stress level. The alloy becomes significantly stronger as the aging duration increases. However, the curve corresponding to the 100 hrs aging

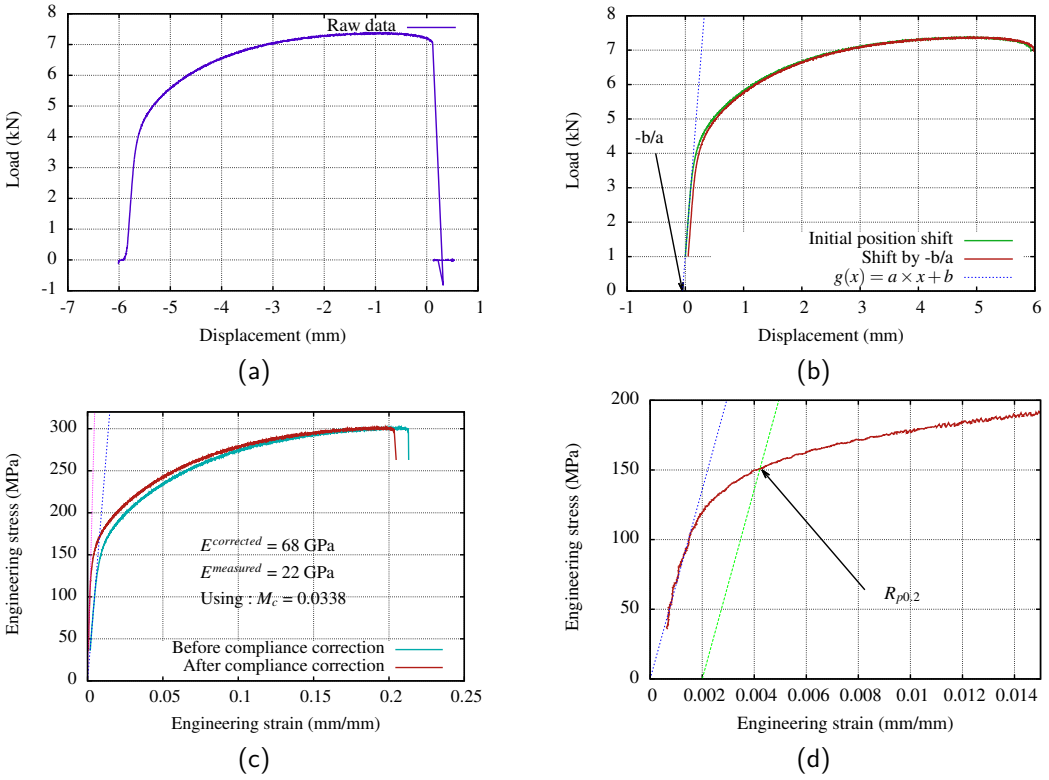

Figure 2.15 – Example of the data correction and interpretation procedure for the conducted tensile tests : (a) Raw Load/Position data, (b) Cleaned-up Load/Position data, (c) Correction for machine+grips compliance and (d) 0.2% offset proof stress reading on corrected plot.

duration shows a decline in the strength of the alloy. The curves for the 1 hr and 10 hrs aging conditions being almost identical suggest that the hardness peak occurs somewhere in between these two durations. It can be stated that the 0.1 hr and 1 hr conditions are underaged and the 10 hrs and 100 hrs are overaged states. This is of course backed up by the previously shown TEM study results.

This well expected trend is replicated in the results of tests conducted at 100°C. However, the alloy yields at slightly lower stress levels due to the higher test temperature. The same can be seen for the 200°C test temperature. In this case, the high test temperature decreases the yield stresses considerably.

Overall, the tests appear to have good repeatability with some exceptions. This resulted in values of yield stress that show little dispersion. The disparity in the ultimate elongation is characteristic of cast aluminum alloys as fracture is closely linked to defects in the microstructure. The ultimate elongation will not be measured as it is not of interest for the purposes of this study.

The aging curve is presented in Figure 2.19 and it shows the evolution of the 0.2% proof strength, $Rp_{0.2}$, as a function of the duration of aging at 200°C. A well expected behavior is observed. Up to a peak value between the durations of 1 h and 10 hrs, artificial aging increases the yield stress of the alloy. Then, the alloy softens as it over-ages thus decreasing its yield stress.

The microstructure-informed yield stress model used in this work will be calibrated and validated using the yield stress values obtained in this section.

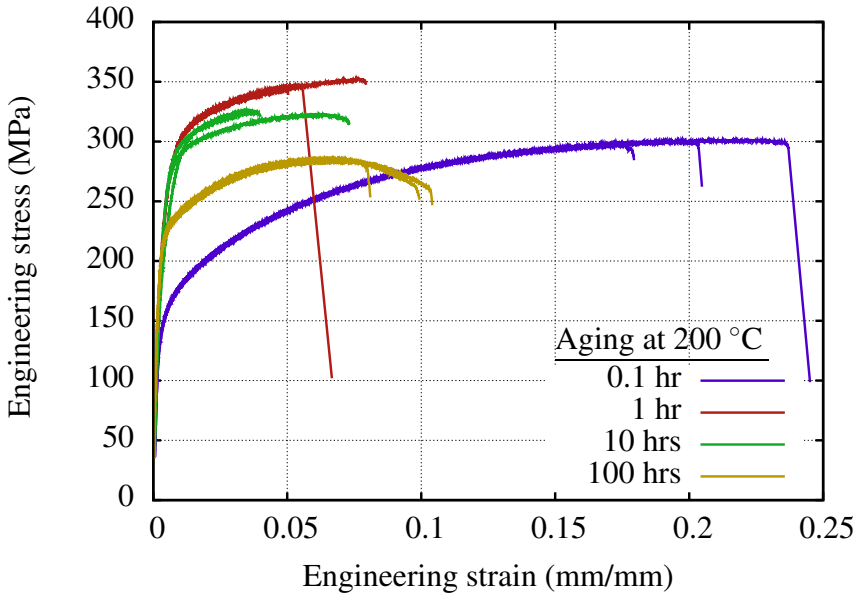

Figure 2.16 – Engineering stress/strain curves for the tensile tests conducted at room temperature on the studied A356+0.5Cu alloy aged for different durations at 200°C.

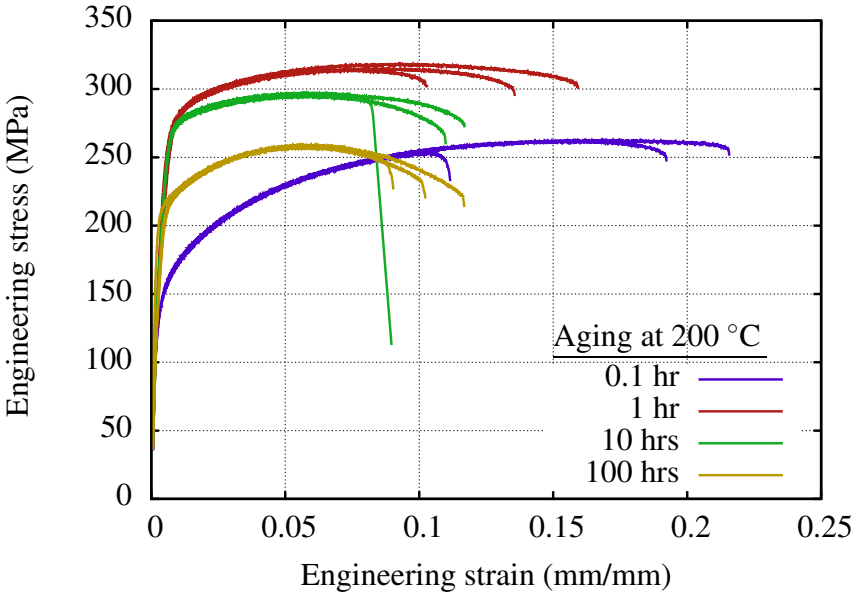

Figure 2.17 – Engineering stress/strain curves for the tensile tests conducted at 100°C on the studied A356+0.5Cu alloy aged for different durations at 200°C.

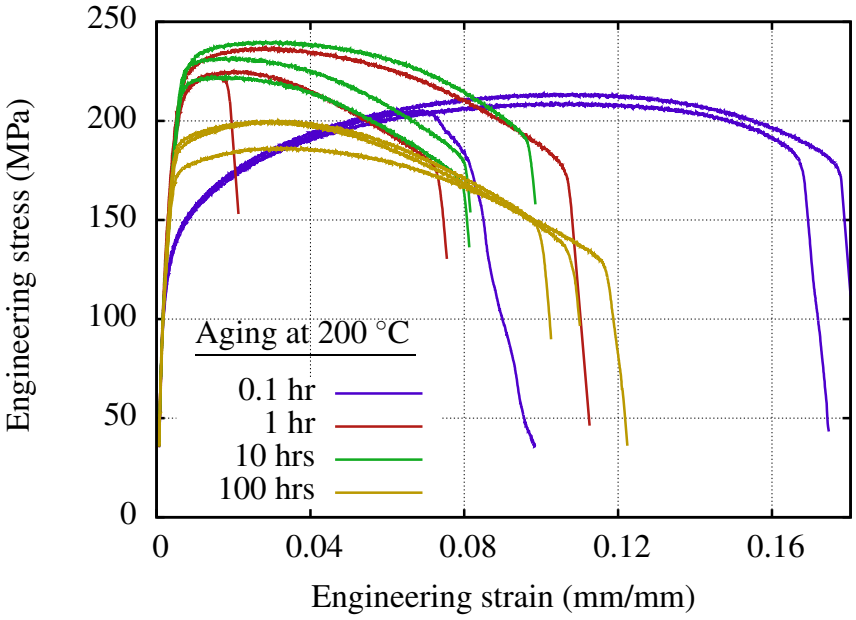

Figure 2.18 – Engineering stress/strain curves for the tensile tests conducted at 200°C on the studied A356+0.5Cu alloy aged for different durations at 200°C.

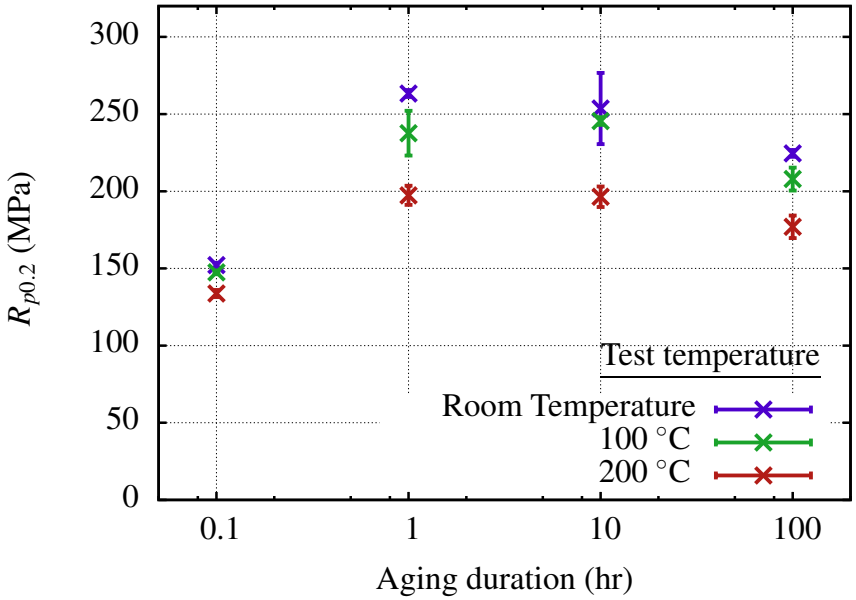

Figure 2.19 – Evolution of the measured 0.2 % offset proof yield stress for the studied A356+Cu alloy as a function of aging duration at 200°C for each test temperature.

2.5 Conclusion

The studied alloy of type A356+0.5Cu was characterized using transmission electron microscopy and tensile testing. This experimental study was conducted on this alloy subject to a solutionizing, quenching and aging heat treatment of different durations at 200°C .

The objectives of the microstructural study were to investigate the precipitation sequence taking place and obtain statistically valid size distributions of precipitates. In summary the conclusions of this study are:

1. Homogeneously distributed precipitates in samples aged 0.1, 1 and 10 hrs at 200°C were characterized as rod-shaped β'' by comparing experimental and simulated SAD patterns.

2. Samples aged for 10 hrs were characterized by the coexistence of these rod-shaped β'' with lath-shaped Q′ or Q″ precipitates in significantly fewer numbers.

3. When observed along a $\langle 100 \rangle_\alpha$ zone axis, the β'' precipitates appear aligned along the $\langle 100 \rangle$Al directions. The ones aligned along the viewing direction are visible due to their round cross-sections. The others are visible edge-on due to the elongated strain field around them.

4. Samples aged for 0.1 hr contained very small precipitates, therefore the strain field around them is very small. This provided a contrast that is too low to

allow them to be visible edge-on.

5. Quantitative measurement of precipitate size distributions of rod-shaped β'' in terms of diameter and length was conducted for samples aged for 0.1, 1 and 10 hrs with the exception of length for samples aged for 0.1 hr.

6. Samples aged 100 hrs at 200°C presented a complex microstructure with both fine and coarse precipitates. The predominant homogeneously distributed fine precipitates have the characteristics of the Q′ phase, i.e. a rectangular cross-section with habit plane 10° to 12° away from $\langle 100 \rangle_\alpha$. Q″ precipitates with rectangular cross-sections with habit plane $\langle 100 \rangle_\alpha$ are also observed in fewer numbers. Coarse precipitates with various shapes were recognized as the Si phase.

7. Very few β'' (possibly β') precipitates are observable in samples aged for 100 hrs.

8. Some heterogeneous precipitation could also be observed in sample aged for 100 hrs.

9. Quantitative measurement of precipitate size distribution of lath-shaped Q′ and Q″ in terms of length, thickness and width was conducted for this sample.

In addition to microstructural investigation, tensile tests were conducted for the same aging conditions at room temperature, 100°C and 200°C . The value of yield stress was the mechanical property of interest and it was measured for each condition. The alloy showed a well expected behavior with measured yield stresses starting at relatively low values for samples aged for 0.1 hr, going up to a peak between the cases aged for 1 and 10 hrs and then continuing the decrease for the case aged for 100 hrs.

In the next chapters the precipitation kinetics and yield stress models will be presented and they will be confronted to the results of this experimental study. These results will be used to validate and calibrate the parameter values of the model.

Chapter 3

Precipitation kinetics model

Résumé

La cinétique de précipitation de la phase β''-Mg_2Si a été modélisée en utilisant une approche théorique. Il s'agit d'une approche basée sur la théorie classique de la germination et croissance et la méthode KWN (Kampmann-Wagner-Numerical).

Dans ce chapitre, les équations gouvernant ce modèle sont présentées et développées en explicitant les hypothèses et les simplifications adoptées. Les instances de couplage indirect avec le logiciel Thermo-Calc sont également décrites. La méthode de résolution numérique est ensuite détaillée.

Le modèle a été validé et calibré en comparant les distributions de tailles des précipités simulées aux résultats expérimentaux du chapitre 2. La confrontation du modèle à ces résultats expérimentaux est présentée. Les variables cinétiques calculées par le modèle sont présentées et décrites.

Precipitation kinetics models usually consist in describing three major processes: nucleation, growth and coarsening. In this chapter, each one of these processes will be presented as well as its governing equations. The hypotheses and assumptions will be discussed and the resulting choices will be determined.

It is worth recalling that the final aim of this work is engineering scale calculations using the finite element method. It is therefore important that calculation costs be kept as minimal as possible while keeping an acceptable level of representativeness of physical phenomena.

Three major approaches to modelling precipitation kinetics can be found in literature: phase field, molecular dynamics and particle size distribution models. For the purposes of this study, the calculation cost of the first two is not viable. Therefore, the modelling effort pursued a size distribution based model.

The input variables to the precipitation kinetics model are the thermal history and certain thermodynamic quantities such as the driving force for precipitation, equilibrium concentrations and others. The values of these variables for the composition of the studied A356+0.5Cu alloy were accessed through indirect coupling with the Thermo-Calc software equipped with the TCAL5 database.

The model uses a number of physical parameters such as the diffusivities of chemical elements. With the exception of the precipitate/matrix interfacial energy, the values for all these parameters are drawn from literature. The value chosen for the interfacial energy was determined so as to provide the best possible fit to the experimental values.

All output variables pertaining to the kinetics of precipitation are made available by the model. Precipitate size distributions, volume fractions and solute concentrations are subsequently utilized in the yield stress model.

3.1 Nucleation

The approaches used to model precipitate nucleation in literature are based on classical nucleation theory in almost every case. It starts out by the expression of the free energy variation resulting from the precipitation of a β phase from a homogeneous supersaturated α' phase (Figure 3.1a). This variation ΔG is expressed using equation 3.1 which splits into two terms: a volume term and a surface term:

$$\Delta G = \Delta g_v V + \gamma S. \tag{3.1}$$

The volume term consists of the volumetric chemical driving force for precipitation Δg_v and the volume V of the precipitating β phase. The surface term consists of γ, the α/β interfacial energy, and the surface S of this interface. These terms are in competition with one another, as the former is a negative contribution (supersaturation) and the latter a positive one (creation of an interface). Figure 3.1b shows a plot of ΔG with respect to the radius of the precipitate where these effects can be observed. Therefore, sufficient chemical driving force and size are necessary for the overall free energy variation to be negative. A negative energy variation

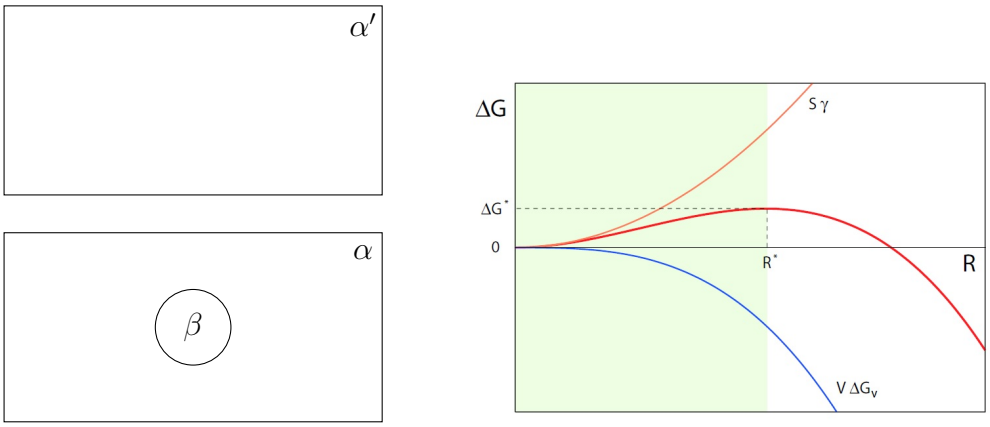

(a) (b)

Figure 3.1 – Nucleation of a particle of the β phase in an α matrix: (a) Schematic of the $\alpha' \rightarrow \alpha + \beta$ transformation and (b) Plot of the corresponding variation in the Gibbs free energy with respect to the radius of the precipitate.

implies that the transformation can occur and that the nucleus remains stable in equilibrium with the parent phase. It is important to note that equation 3.1 can generally have a third term accounting for elastic strain energy. In this work this contribution is considered negligible and is therefore omitted.

In order to express the critical size of nuclei, i.e. the size at which further growth minimizes the free energy must be determined. The critical size is therefore the root of the derivative of ΔG with respect to size. If one assumes a spherical shape of the β phase with a radius R, the critical radius for nucleation R^* is expressed with equation 3.2:

$$R^\star = \frac{-2\gamma}{\Delta g_v}. \tag{3.2}$$

The energy barrier ΔG^*, i.e. the free energy corresponding to a critical nucleus, can therefore be expressed using equation 3.3:

$$\Delta G^\star = \frac{16\pi\gamma^3}{3\Delta g_v^2}. \tag{3.3}$$

The number of stable nuclei that are added to the system at any given time is the nucleation rate J. This nucleation rate is given by equation 3.4 [69, 70]:

$$J = Z\beta^\star N \exp\left(\frac{-\Delta G^\star}{k_B T}\right) \exp\left(\frac{-\tau}{t}\right) \tag{3.4}$$

with k_B being the Boltzmann constant and T the temperature.

It is best viewed as the product of three factors. First, there is $N \exp\left(\frac{-\Delta G^\star}{k_B T}\right)$ which expresses the total number of nucleation sites which may have critical nuclei grown around them. It consists of the temperature dependent energy barrier term on the one hand. On the other hand, we find N which is the nucleation site

density in the matrix. If one assumes a homogeneous nucleation, i.e. the absence of preferential nucleation sites within the matrix, it can be expressed by equation 3.5. It simply considers that any atomic site in the crystal can be a potential nucleation site for the precipitating phase:

$$N = \frac{\mathcal{N}_A}{V^\alpha} \tag{3.5}$$

with $\mathcal{N}_A$ being the Avogadro number and V^α the molar volume of the matrix.

In the case of heterogeneous nucleation, an additional heterogeneous nucelation rate can be expressed with a number of nucleation sites depending on the nature of the heterogeneity (grain boundaries, inclusions, etc..). The term $S(\theta)$ in equation 3.6:

$$\Delta G^{\star,het} = \Delta G^\star S(\theta) \tag{3.6}$$

with θ being the wetting angle of the interface, is always smaller than 1 [71]. This expresses how heterogeneous nucleation has a lower energy barrier in comparison to homogeneous nucleation (Figure 3.2). This is due to the lowering of the positive surface term due to the pre-existence of an interface. In this work, in view of the homogeneous nature of the observed precipitation in the studied alloy, heterogeneous nucleation will be neglected.

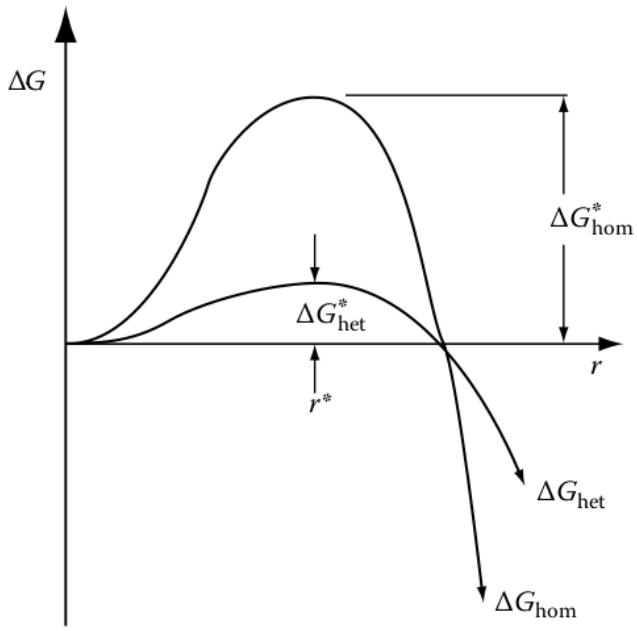

Figure 3.2 – The difference in energy barriers for homogeneous and heterogeneous nucleation [71].

The second factor $Z\beta^\star$ in equation 3.4 concerns the stochastic aspect of nucleation. Nuclei that are exactly at the energy barrier for nucleation are at an

unstable equilibrium, they can either dissolve or grow. The Zeldovitch factor Z (equation 3.7) expresses the probability that such nuclei have of growing:

$$Z = \frac{V^{\alpha} \Delta g_v^2}{8\pi(\gamma^3 k_B T)^{1/2}}. \tag{3.7}$$

The condensation rate $\beta^{\star}$ (equation 3.8) expresses the rate at which "monomers" of the precipitating phase attach to the growing nuclei:

$$\beta^{\star} = \frac{16\pi\gamma^2 D\bar{C}}{\Delta g_v^2 a^4} \tag{3.8}$$

with D being the diffusivity, $\bar{C}$ the mean solute molar fraction in the matrix and a the lattice parameter of the matrix.

The third and last factor, $\exp(-\tau/t)$, where t is time, is an incubation function that accounts for the thermal inertia of the nucleation process. The incubation period τ expresses the time necessary for the system to begin the transformation (equation 3.9):

$$\tau = \frac{8 k_B T \gamma a^4}{V^{\alpha} \Delta G_V^2 D\bar{C}}. \tag{3.9}$$

In fact, time as such is not a relevant variable in a constitutive equation. It can only appear by integrating an evolution equation along a particular path [72]. It is well understood, for example, that interrupting a test for a longer or shorter period of time should not change the result if this period is under conditions where the material does not evolve. A rigorous approach to taking incubation into account would be to introduce a specific variable with its own law of evolution, to be integrated as a function of temperature history. In our work, back-to-back heat treatment transient sequences of quenching and aging will be simulated. Inserting time explicitely in such an incubation function is therefore inconsistent as the phase transformation may occur in stages. Nevertheless simulations were carried out with and without this term and hardly any difference could be noticed. It was then decided to omit this incubation term in the final simulation.

One can see, the evaluation of these equations requires knowledge of the values of the volumetric precipitation driving force Δg_v. Thermo-Calc allows the calculation of Δg_m, the molar precipitation driving force of a phase for any alloy composition. It depends on temperature and the molar concentration of solute in the matrix. This value is then normalized using the molar volume of the precipitating phase in order to obtain the volumetric driving force Δg_v. Note that although the precipitates were identified as the β'' phase, the precipitation sequence will be collapsed into the equilibrium phase β for simplification. Thermodynamic data in TCAL5 is also far more reliable for stable phases than it is for metastable phases.

The model is given access to these values through indirect coupling. First, the values of the precipitation driving force of β-Mg_2Si as a function of temperature and solute content in the matrix are tabulated. Multiple calculations were performed in order to span a wide range of compositions and temperatures. Subsequently,

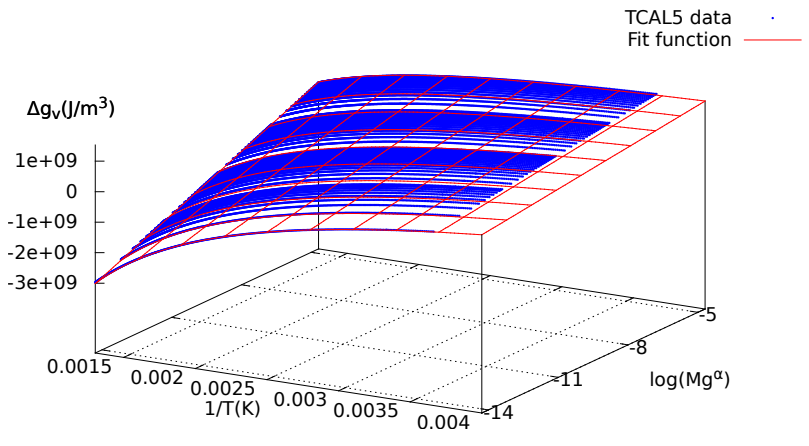

Figure 3.3 – Fit function of the precipitation driving force of β-Mg_2Si in the aluminum matrix extracted from Thermo-Calc/TCAL5.

all the results were mapped using a Taylor series fit function resulting in a simple equation which was implemented in the model (Figure 3.3). This numerical fit function is given by equation 3.10 with x and y representing the temperature inverse, $1/T(K)$, and the logarithm of the molar fraction of Mg in the matrix ,$\log(C^{\alpha}_{Mg})$, respectively.

$$\begin{cases} f(x,y) = ax^{-1} + by + cx^{-2} + dy^2 + eyx^{-1} + f \\ a = -3.65 \times 10^4 \ Jm^{-3}K^{-1} \\ b = -1.03 \times 10^7 \ Jm^{-3} \\ c = -4.45 \times 10^2 \ Jm^{-3}K^{-2} \\ d = -2.98 \times 10^4 \ Jm^{-3} \\ e = 4.46 \times 10^5 \ Jm^{-3}K^{-1} \\ f = 2.04 \times 10^9 \ Jm^{-3} \end{cases} \tag{3.10}$$

This indirect coupling scheme is costless to compute, contrary to direct coupling to Thermo-Calc which would induce large calculation costs rendering it impractical. Also, the process leading up to the determination of the indirect coupling fit equation was scripted and is straight forward. A commented example of a Thermo-Calc macro can be found in Appendix B.

3.2 Growth

3.2.1 The growth rate

A stable supercritical nucleus ($R > R^{\star}$) is capable of growing into increasingly larger sizes. It is therefore important to express the rate at which growth occurs.

The growth rate is expressed with respect to the radius R of precipitates which are assumed to be spherical. The corrections necessary to take into account the real morphology of precipitates will be addressed later on. At the atomic scale, growth is controlled by diffusion as atoms migrate to the precipitate/matrix interface. This process can therefore be described using Fick's laws [73]. The first law allows the expression of the diffusive flux J_i of solute element i as a function of the gradient of concentration C_i assuming an ideal solution (equation 3.11):

$$J_i = -D_i.\nabla C_i. \tag{3.11}$$

Fick's second law expresses how diffusive flux of atoms changes the concentration profile with respect to time. Assuming that the diffusivity is independent of coordinates, it can be written as equation 3.12:

$$\frac{\partial C_i}{\partial t} = D_i \Delta C_i. \tag{3.12}$$

In spherical coordinates, assuming steady-state ($\partial C_i/\partial t = 0$) and recalling that the concentration profile depends exclusively on the radius r ($C_i(r, \theta, \phi) = C_i(r)$), this law leads to a Cauchy ordinary differential equation 3.13:

$$\frac{\partial^2 C_i}{\partial r^2} + \frac{2}{r}\frac{\partial C_i}{\partial r} = 0. \tag{3.13}$$

The solution to such an equation takes the form given by equation 3.14 with a and b being constants to be determined using boundary conditions:

$$C_i(r) = a + \frac{b}{r}. \tag{3.14}$$

Setting:

- C_i^{∞} : concentration of element i in the matrix far from the interface;
- $C_i^{\alpha/\beta}$: concentration of element i in the matrix at the interface;
- $C_i^{\beta/\alpha}$: concentration of element i in the precipitate at the interface. Assuming a stoechiometric precipitate and no diffusion in the precipitate, this will be considered a constant C_i^{β}.

We can formulate the following boundary conditions:

- $C_i(r \to \infty, t) = C_i^{\infty}$;
- $C_i(r = R(t), t) = C_i^{\alpha}$, $R(t)$ being the radius of the precipitate at time t;
- $C_i(r < R(t), t) = C_i^{\beta}$.

This yields the expression of the concentration profile as a function of the distance from the center of the spherical precipitate:

$$C_i(r) = C_i^{\infty} + \frac{R(t)}{r}(C_i^{\alpha/\beta} - C_i^{\infty}) \quad , \quad r \geqslant R(t), \tag{3.15}$$

$$C_i(r) = C_i^{\beta} \quad , \quad 0 \leqslant r < R(t). \tag{3.16}$$

The total flux through the interface I in dt is responsible for the volume change dV of the particle according to equation 3.17 expressing mass conservation:

$$Idt = (C_i^{\alpha/\beta} - C_i^{\beta})dV \tag{3.17}$$

with $dV = 4\pi R(t)^2 dR(t)$. The total flux I is simply calculated by integrating the flux over the interface surface oriented along its normal (equation 3.18):

$$I = \iint_{int} -D_i \frac{\partial C_i(r)}{\partial n} dS. \tag{3.18}$$

Using equation 3.16 and considering the surface element dS of which the normal is radial and oriented to the exterior, equation 3.19 is obtained:

$$I = 4\pi D(C_i^{\alpha/\beta} - C_i^{\infty})R(t). \tag{3.19}$$

Finally, combining equations 3.17 and 3.19 leads to the growth rate expression that is widely used in literature (equation 3.20):

$$\frac{dR(t)}{dt} = \frac{D}{R(t)} \frac{(C_i^{\infty} - C_i^{\alpha/\beta})}{(C_i^{\beta} - C_i^{\alpha/\beta})}. \tag{3.20}$$

When modelling the precipitation of a phase where there is only one diffusing chemical element, equation 3.20 is sufficient. This was exemplified in the work of Martinez *et al.* [13] where coarsening of θ-Al_2Cu precipitates was modelled. Indeed, only the diffusion of Cu is to be considered when calculating the growth rate of these precipitates. Therefore, there is a single possible equilibrium concentration of Cu in the matrix at any given temperature.

However, when two chemical elements must diffuse within the aluminum matrix in order to form the precipitate, other considerations apply. This is the case for the β-Mg_2Si around which this work is centered. While the growth rate equation is still valid for each one of the two elements participating in the formation of the precipitate, there is a number of sets of possible equilibrium concentrations of Mg and Si in the matrix at any given temperature. This requires the addition of a thermodynamic and a kinetic constraint to fully define the growth rate.

The thermodynamic constraint consist of the tie-line equations in the Al-Si-Mg diagram expressing the equilibrium between α-Al and β-Mg_2Si. Tie-lines calculated using Thermo-Calc are shown in Figure 3.4a for temperatures ranging from 273.15 to 723.15 K. The solubility product K_s for the β-Mg_2Si is expressed according

to equation 3.21 as a function of mole fractions of Mg and Si in the matrix at equilibrium, $C_{Mg}^{\alpha,eq}$ and $C_{Si}^{\alpha,eq}$ respectively:

$$K_s = (C_{Mg}^{\alpha,eq})^2.C_{Si}^{\alpha,eq}. \tag{3.21}$$

Plotting $\log(K_s)$ against the temperature inverse collapses these tie-lines into one straight line that can be fitted with a simple linear function (Figure 3.4b). The obtained fit equation (equation 3.22) expresses the thermodynamic constraint that the equilibrium concentrations must respect:

$$\log(K_s) = -\frac{7144}{T} + 2.7. \tag{3.22}$$

The kinetic constraint consists of ensuring that solute flux is respective of the difference in diffusivities between Mg and Si and of the stœchiometry of the precipitating phase. Therefore, the growth rate expressed by equation 3.20 must be the same whether it be calculated using the Mg or Si supersaturations (equation 3.23):

$$\frac{dR(t)}{dt} = \frac{D_{Mg}}{R(t)}\frac{(C_{Mg}^{\infty} - C_{Mg}^{\alpha/\beta})}{(C_{Mg}^{\beta} - C_{Mg}^{\alpha/\beta})} = \frac{D_{Si}}{R(t)}\frac{(C_{Si}^{\infty} - C_{Si}^{\alpha/\beta})}{(C_{Si}^{\beta} - C_{Si}^{\alpha/\beta})}, \tag{3.23}$$

where D_{Mg} and D_{Si} are the diffusivities of Mg and Si respectively.

One of the adopted simplifications used in this work is the collapse of the precipitation sequence into a single equivalent phase considered to be β-Mg_2Si. The metastable precursors to this phase are therefore not considered and all the previously mentioned thermodynamic data are extracted for the stable phase. This simplification was used in the pioneering implementations of precipitation modelling by Myhr *et al.* [74, 75], Deschamps *et al.* [76] and Bréchet *et al.* [77]. Also, this phase is considered stœchiometric which defines the interfacial concentrations on the precipitate side C_{Si}^{β} and C_{Mg}^{β} (0.334 and 0.666 respectively). The concentrations far from the interface C_{Mg}^{∞} and C_{Si}^{∞}, can be considered as the mean solute concentrations in the matrix at any given time step. Therefore, the unknowns remaining to evaluate the growth rate are the matrix interfacial concentrations $C_{Si}^{\alpha/\beta}$ and $C_{Mg}^{\alpha/\beta}$.

3.2.2 Interfacial compositions

In the case of a curved interface α/β, the equilibrium between the two phases is modified due to capillarity effects, the so called Gibbs-Thomson effect. When assuming a local equilibrium modified by the Gibbs-Thomson effect, the interfacial compositions are the equilibrium compositions corrected for curvature. Indeed, the solute concentrations in the matrix near the α/β interface and far from it are different. The classical expression that is used in modelling precipitation kinetics is given in equation 3.24:

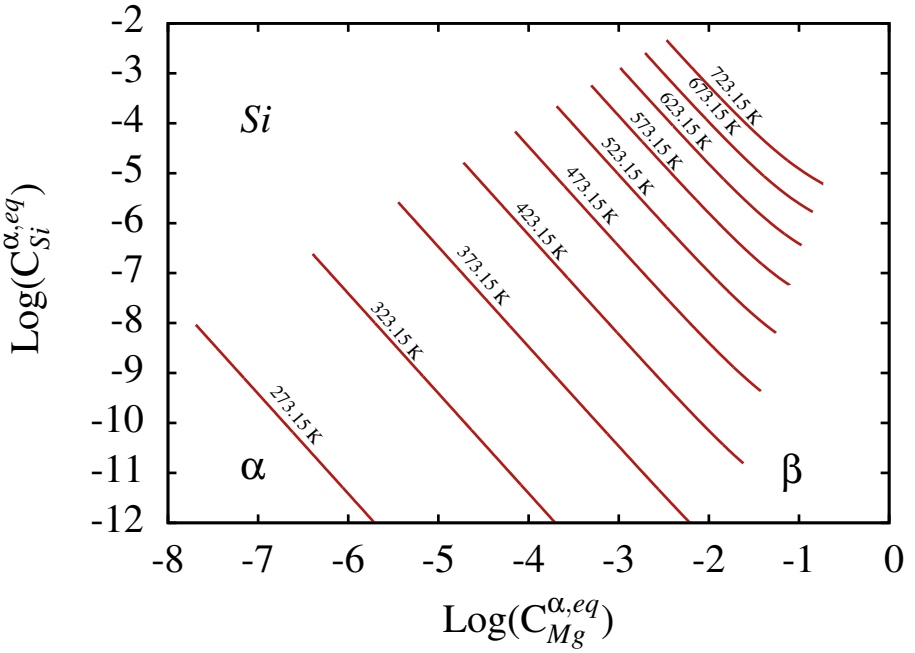

(a)

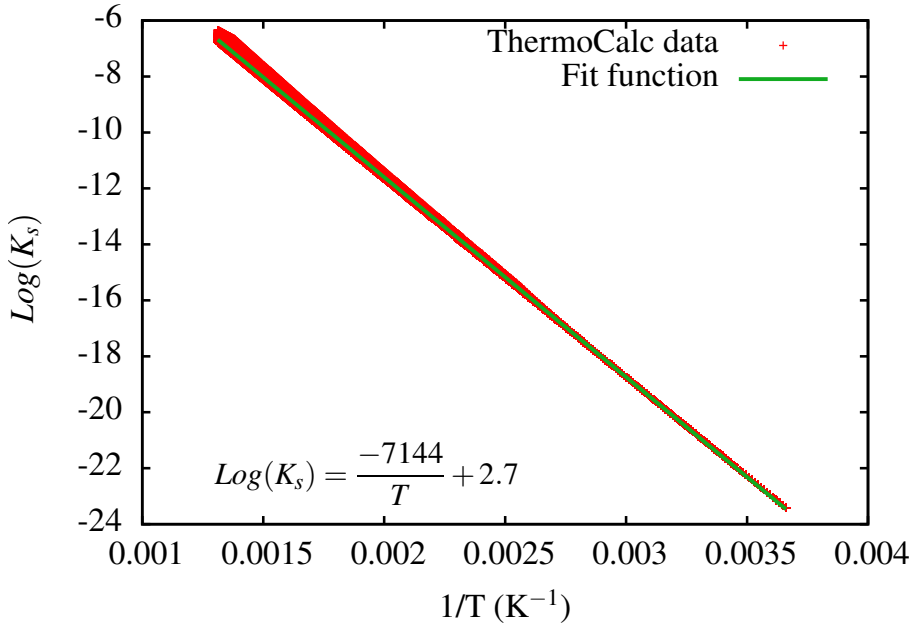

(b)

Figure 3.4 – Determination of the solubility product for β-Mg_2Si using Thermo-Calc/TCAL5: (a) Mg and Si concentrations in the matrix for different temperatures representing the phase diagram tie-lines and (b) logarithm of the solubility product K_s as a function of the temperature inverse with the corresponding fit function implemented in the model.

$$C_{i,R}^{\alpha/\beta} = C_{i,R=\infty}^{\alpha/\beta} . \exp\left(\frac{2.\gamma.V^{\beta}}{R.k_B.T}\right), \tag{3.24}$$

with $C^{\alpha}_{i,R=\infty}$ the concentration of solute i in the matrix for an infinite curvature (planar interface), V^{β} the molar volume of the precipitation β phase and R the precipitate radius.

Although this expression is commonly used, it is worth noting that it is obtained by using an approximation that does not always apply. Perez [78] showed how that solution of the Gibbs-Thomson equation is obtained under the assumption of a pure precipitating phase (i.e. C^{β}_{i}=1). In his publication the author also showed that there are other approximations that may be used to solve the Gibbs-Thomson equation.

Under the assumption of a low curvature effect, i.e. $C^{\alpha/\beta}_{i,R} \simeq C^{\alpha/\beta}_{i,R=\infty}$, there is a different solution given by equation 3.25:

$$C^{\alpha/\beta}_{i,R} = C^{\alpha/\beta}_{i,R=\infty}.\left(1 + \frac{2.\gamma.V^{\beta}}{R.k_B.T}\frac{1 - C^{\alpha/\beta}_{i,R=\infty}}{C^{\beta}_{i} - C^{\alpha/\beta}_{i,R=\infty}}\right). \tag{3.25}$$

Finally, by assuming a dilute solid solution whereby $C^{\alpha/\beta}_{i,R}$ and $C^{\alpha/\beta}_{i,R=\infty}$ are small compared to unity, a third solution given by equation 3.26 is provided:

$$C^{\alpha/\beta}_{i,R} = C^{\alpha/\beta}_{i,R=\infty}.\exp\left(\frac{2.\gamma.V^{\beta}}{C^{\beta}_{i}.R.k_B.T}\right). \tag{3.26}$$

In this work, this expression of the Gibbs-Thomson effect was used as it is the most coherent with the modelled precipitates. It is noteworthy that setting if $C^{\beta}_{i} = 1$ in equations 3.26 and 3.25, the former becomes exactly equation 3.24 and the latter becomes its first order Taylor expansion.

Du *et al.* [79] used a different approach to evaluate the effect of curvature on interfacial equilibrium concentrations. It consisted in constructing what they referred to as a "Gibbs-Thomson phase diagram" using Thermo-Calc. It is obtained by increasing the Gibbs free energy of the precipitating phase in the database by $2\gamma\kappa V_m$, with κ being the curvature and V_m the precipitate molar volume. The in-built energy minimization algorithm of Thermo-Calc then produces a new phase diagram taking into account curvature. Of course, this calculation is then performed for the whole range of curvature values to produce the full curvature-dependent diagram. The model then uses a table look-up technique to navigate the diagram and access the required values.

Another approach was demonstrated in [80] where the authors numerically integrated the differential form of the curvature-modified equilibrium condition of a multicomponent system. With knowledge of Gibbs energies of the matrix and the precipitating phase, they numerically integrated the tie-line equations with increments of curvature. Figure 3.5 demonstrates how the integration method produces results that are consistent with the Gibbs-Thomson phase diagram method calculated using Thermo-Calc.

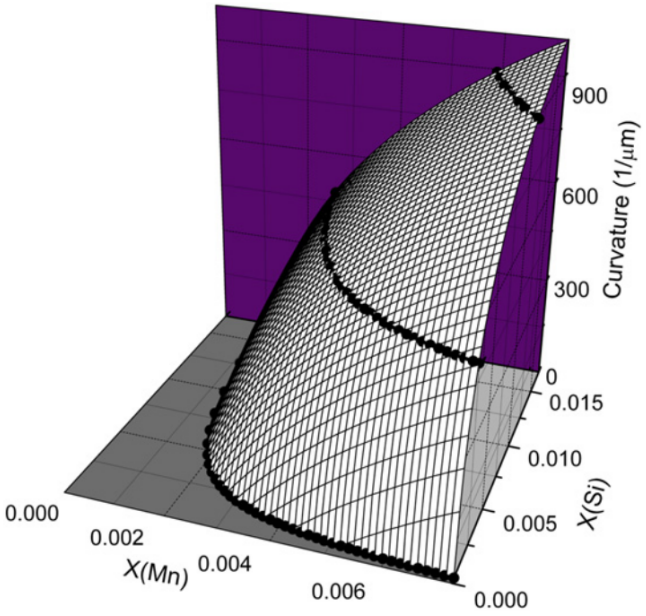

Figure 3.5 – Gibbs–Thomson phase diagram (surface showing matrix solute content vs. curvature) of the Al–Mn–Si system at 600°C calculated by the integration method together with the solubility limit lines (markers) for various curvatures calculated by Thermo-Calc [80].

3.2.3 Mean matrix composition

In the model, the solute concentrations in the matrix far from the interface C_{Mg}^{∞} and C_{Si}^{∞} are considered to be the mean matrix concentrations. The initial mean composition of the matrix is considered to be the equilibrium composition at the solutionizing temperature. As the volume fraction of the precipitating phase increases, this mean composition must be updated. To update these values, the mass balance equation 3.27 is used:

$$\bar{C_i^{\alpha}} = \frac{C_i^0 - f^{\beta}.C_i^{\beta}}{1 - f^{\beta}}, \tag{3.27}$$

with $\bar{C_i^{\alpha}}$ being the mean concentration in the matrix of solute i, C_i^0 its initial concentration, C_i^{β} its concentration in the precipitate and f^{β} the molar fraction of the β phase.

Figure 3.6 shows the evolution of the equilibrium concentrations of Mg and Si in the matrix with respect to temperature according to a Thermo-Calc calculation using TCAL5 for the studied A356+0.5Cu alloy. The Mg content in the aluminum matrix is almost constant for temperatures above the solvus of β-Mg_2Si. The observed decrease in Mg content below this solvus temperature is entirely due to the formation of the β-Mg_2Si. Therefore, since solutionizing temperatures are always higher than the solvus temperature, C_{Mg}^0 is considered constant.

The same cannot be said about Si because it contributes in the formation of

the Si phase alongside β-Mg_2Si. This is shown in Figure 3.7 where the yellow curve represents the equilibrium Si concentration in the matrix and the red curve the equilibrium molar fraction of the Si phase. Therefore, the amount of Si that is available to contribute in the formation of β-Mg_2Si is not a constant. The blue curve was obtained by eliminating the amount of Si that goes into the formation of the Si phase. This curve represents C^0_{Si} which in this case is temperature-dependent. It was fitted and implemented in the model as such. It is worth noting that this implies that the model considers that the Si phase forms and the matrix is depleted from Si instantaneously.

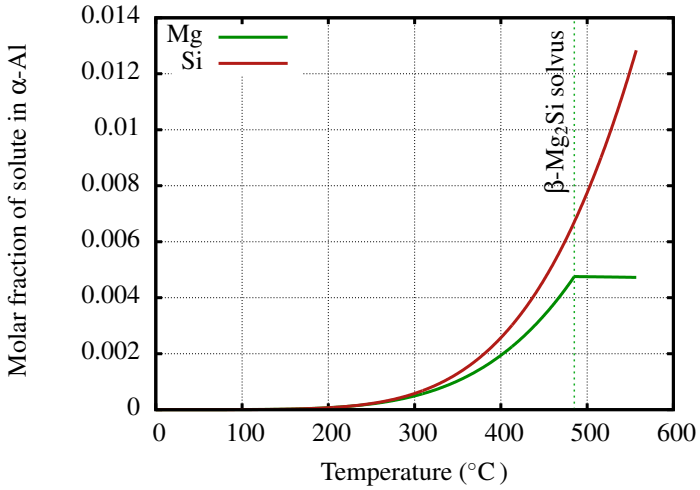

Figure 3.6 – Evolution of the equilibrium molar fraction of Mg and Si in the matrix with respect to temperature calculated using Thermo-Calc/TCAL5 for the A356+0.5Cu alloy.

3.2.4 Effect of precipitate morphology

As seen in the chapter 2, all observations of the β''-Mg_2Si phase indicate an elongated morphology (cf. Figure 2.7). This may lead to a breakdown in the results of the model when the aspect ratio of the precipitates becomes significantly large. However, the model as described so far is based on the assumption of a spherical morphology for the precipitating phase. Taking into account morphology has been addressed in literature in two different ways.

Considering a rod-shaped precipitate as given in Figure 3.8, the aspect ratio will be given by equation 3.28:

$$\lambda = \frac{l}{2.R} \tag{3.28}$$

with l and R being the length and radius of the precipitate respectively.

The nucleation and growth theoretical equations can all be rewritten as a function of λ and one of the dimensions (either l or R). This adds an unknown to the problem and therefore requires the description of the evolution of the aspect

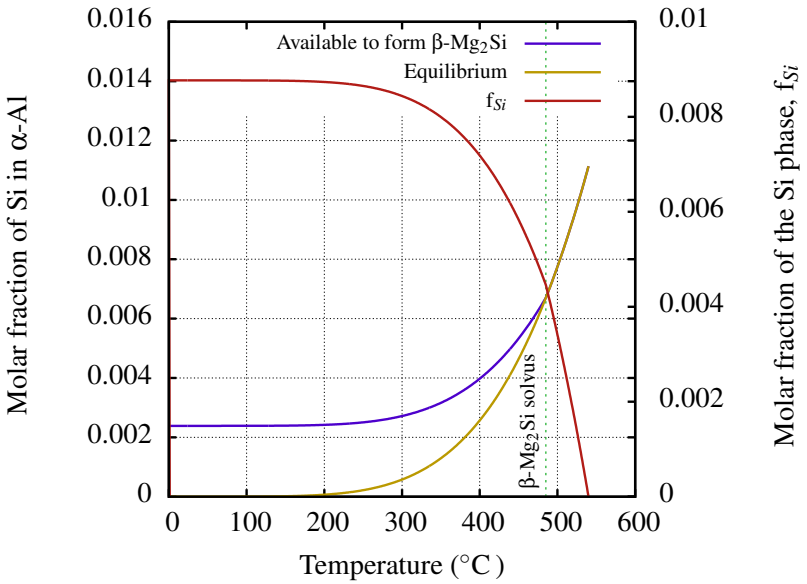

Figure 3.7 – Concentration of Si available to form β-Mg_2Si (blue curve) with respect to temperature, obtained using the equilibrium concentration of Si (yellow curve) and the molar fraction of the Si phase (red curve), calculated using Thermo-Calc/TCAL5.

ratio. It is for example possible to experimentally define a time-dependent function $\lambda(t)$ for a given isothermal heat treatment and implement it in the model. This of course limits the non-isothermal capacity of the model.

Another possibility was exemplified by Bardel *et al.* [8] in their precipitation model for non-isothermal treatments of a 6061 aluminum alloy. According to their experimental findings using small angle neutron scattering (SANS) for a wide range of temperatures, the aspect ratio remained relatively close to an average value of 11. Therefore, as a model simplification, they used a constant value for the aspect ratio $\lambda = 11$. The same approach was used by Chen *et al.* [10] in modelling precipitation in an Al-7Si-Mg alloy. In their work they measured the average radii and lengths for a set of aging conditions using TEM imagery and calculated an average aspect ratio of 7.

Figure 3.8 – Schematic of the elongated morphology of the β''-Mg_2Si precipitates.

The second approach consists in introducing analytically derived corrections to the growth rate (f in equation 3.29) and the Gibbs-Thomson effect (g in equation 3.30):

$$\frac{dR}{dt} = f\frac{D}{R(t)}\frac{(C_i^{\infty} - C_i^{\alpha/\beta})}{(C_i^{\beta} - C_i^{\alpha/\beta})}, \tag{3.29}$$

$$C_{i,R}^{\alpha/\beta} = C_{i,R=\infty}^{\alpha/\beta}.\exp\left(\frac{2.g.\gamma.V^{\beta}}{C_i^{\beta}.R.k_B.T}\right). \tag{3.30}$$

Holmedal *et al.* [81] introduced a generalization of the Kampmann-Wagner numerical (KWN) method to non-spherical precipitates. The shape of a prolate spheroid can be considered a good approximation of the rod morphology of the precipitates (Figure 3.9a). Therefore, in order to calculate the correction factor f they developed an analytical solution to the diffusion problem in the prolate spheroidal coordinates (ξ,η,ϕ). In this coordinate system, they derived the solute concentration profile by assuming it dependent only on ξ. Indeed, surfaces of a constant ξ form prolate spheroids and outward growth is represented by increases of this coordinate. Using that compositional profile they calculated the flux of solute through a prolate spheroidal interface according to Fick's law. By equating this flux to the flux through a volume-equivalent spherical interface mediating the correction factor f, an analytical expression for the latter was determined (equation 3.31):

$$f(\lambda) = \frac{2\sqrt{\lambda^2-1}}{\sqrt[3]{\lambda}ln(2\lambda^2+2\lambda\sqrt{\lambda^2-1}-1)}. \tag{3.31}$$

They also used the same approach for a needle-shaped cuboid (Figure 3.9b). In this case, although an analytical compositional profile can be expressed, calculating the flux through the surface had to be performed numerically. A different expression for the correction factor f was therefore derived (equation 3.32):

$$f(\lambda) = 0.1\exp(-0.091(\lambda-1)) + \frac{1.736\sqrt{\lambda^2-1}}{\sqrt[3]{\lambda}ln(2\lambda^2+2\lambda\sqrt{\lambda^2-1}-1)}. \tag{3.32}$$

Both these factors degenerate to a value of 1 for spheres, i.e. $\lambda = 1$. Figure 3.10 shows the evolution of these factors as a function of the aspect ratio. It shows how there is a positive influence of the aspect ratio on the growth rate, i.e. as a particle elongates, it grows faster. The authors reported that this is in contradiction with the results of the approach used by Bardel *et al.* and other studies they examined where the influence is negative.

The second correction factor g, is obtained under the assumption of shape conservation and quasi-constant evolution of the aspect ratio. The first assumption means that the surface of the particle is related to its volume. The Gibbs-Thomson modified chemical potential of a given alloying element in the precipitating phase can be written according to equation 3.33:

$$\frac{\partial G^{\beta}}{\partial n^{\beta}} = \mu_m^{\beta} + \gamma.\frac{\partial S^{\beta}}{\partial n^{\beta}} \tag{3.33}$$

with S^{β} being the particle surface, n^{β} the number of atoms in the particle, μ_m^{β} the chemical potential and γ the surface energy.

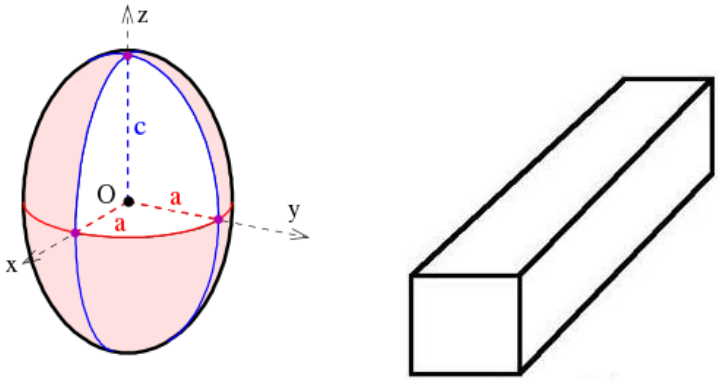

Figure 3.9 – Drawing of analytical shapes approximating the rod shaped β''-Mg_2Si precipitates: (a) Prolate spheroid characterized by c>a and (b) Needle-shaped cuboid.

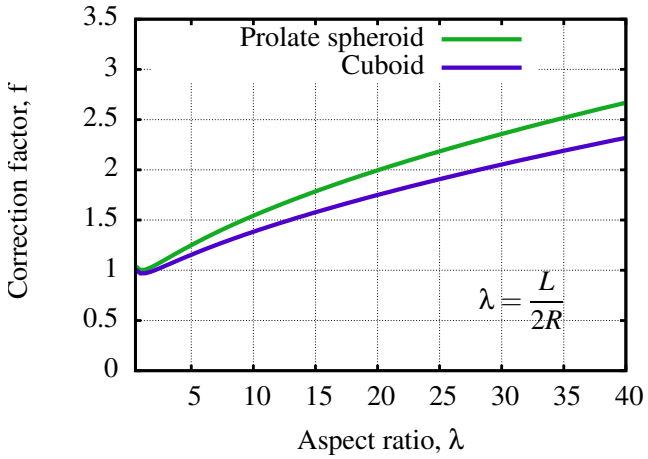

Figure 3.10 – Correction factor f [81], for different precipitate morphologies as a function of the aspect ratio λ.

Using $V^\beta = n^\beta.V_m^\beta$ equation 3.34 can be obtained. The correction factor g can therefore be obtained by equating the previous equation to its expression for a volume-equivalent sphere:

$$\frac{\partial G^\beta}{\partial n^\beta} = \mu_m^\beta + \gamma.\frac{\partial S^\beta}{\partial V^\beta}V_m^\beta = \mu_m^\beta + \frac{2.g.\gamma.V_m^\beta}{R}. \tag{3.34}$$

The correction factor g is then scaled so as to degenerate to a value of 1 for spheres (λ=1) and is therefore given by equation 3.35:

$$g = \frac{1}{2}R\frac{\partial S^\beta}{\partial V^\beta} = \frac{1}{8\pi R}.\frac{\partial S^\beta}{\partial R}. \tag{3.35}$$

Applying this equation to a prolate spheroid and a needle-shaped cuboid renders equations 3.36 and 3.37 respectively. Figure 3.11 shows the evolution of these factors as a function of the aspect ratio:

$$g(\lambda) = \frac{1}{2\lambda^{2/3}} \left(1 + \frac{\lambda^2}{\sqrt{\lambda^2 - 1}} sin^{-1} \left(\frac{\sqrt{\lambda^2 - 1}}{\lambda} \right) \right), \tag{3.36}$$

$$g(\lambda) = \frac{2\lambda + 1}{2\pi} \left(\frac{4\pi}{3\lambda} \right)^{2/3}. \tag{3.37}$$

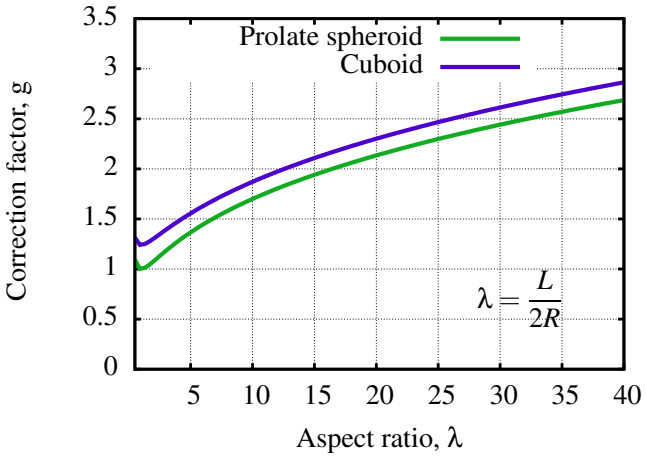

Figure 3.11 – Correction factor g [81], for different precipitate morphologies as a function of the aspect ratio λ.

All these corrections depend on the aspect ratio and therefore the same limitation discussed for the previous approach applies here. It is necessary to have a description of the evolution of the aspect ratio or treat is as a constant.

A subsequent paper by Du *et al.* [82] used this generalization to simulate an isothermal aging heat treatments of an Al-Mg-Si alloy. They performed three kinds of simulations : using the spherical assumption, using the corrections with a constant aspect ratio of 8 and using the corrections with a varying aspect ratio. Generally, they found that the introduction of the correction factors improved the agreement of the model with their TEM observations. It especially dealt well with the onset of ripening after long durations of aging. Regarding the size distributions, the correction factors produce wider distributions compared to the classical spherical case. Varying aspect ratio produces a faster evolution of the mean radius in comparison to the constant aspect ratio case. This effect was particularly significant for long exposure durations.

Introducing both corrections to the model results in a size-dependent competition between the diffusion acceleration and the suppression of the supersaturation by the modified Gibbs-Thomson effect. Figure 3.12 presents the growth rate normalized by the growth rate for a spherical particle as a function of the aspect ratio for different equivalent particle sizes. It shows that for a small particle size, the attenuation of the supersaturation by the modified Gibbs-Thomson effect has more weight than the accelerated diffusion. There is therefore an overall negative influence of the aspect ratio on the growth rate in comparison to the spherical

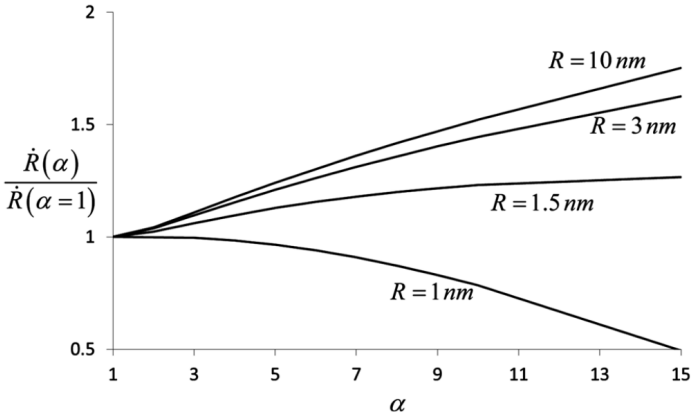

Figure 3.12 – Evolution of the normalized growth rate as a function of the aspect ratio, here noted α, for different equivalent precipitate radii R [82].

case. This dominance is inverted as size increases and the positive effect of the aspect ratio is established.

This approach was adopted in this work. The aspect ratio was considered constant and equal to the average value seen in chapter 2 ($\lambda = 6.6$).

3.3 The KWN method

In order to track precipitation kinetics it is possible to simply solve the equation system outlined earlier for the mean radius (a single size class approach). This is less costly but requires defining an additional law when ripening takes over and the supersaturation is null. It can be achieved by using Lifshitz-Slyozov-Wagner (LSW) theory which specifies a critical radius between dissolving and growing particles. The model has to transition from one regime to the other based usually on arbitrary terms. Using a single size class approach also results in a loss of information regarding the shape of the size distribution and its width. This is especially of importance if these size distributions are destined for use in a yield stress model. In such a model, it is desired to take into account the contribution of the entire distribution in impeding dislocation movement.

Another approach consists in uniformly discretizing the size space into a number of size classes. This approach is referred to as the Kampmann-Wagner Numerical method (KWN) after the two scientists who devised it [83]. Later on, this method was succesfully implemented in many precipitation modelling studies [84, 74, 75, 76, 7, 13, 8]. The discretization of the continuous size distribution results in a number of size classes i of similar width ΔR to which a number density ρ_i of particles of the same size R_i is associated. Figure 3.13 shows an example of such a discretization. It is therefore possible to calculate the growth rate as expressed in equation 3.29 for each size class. The temporal evolution of the number density of in any given size class therefore translates into a flux in the size space that must

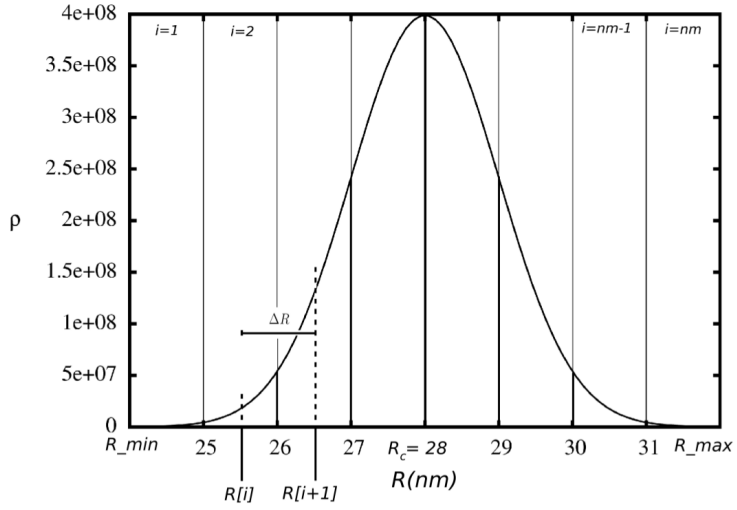

Figure 3.13 – Schematic of the discretization of the continuous size distribution [7].

be defined.

At any given time step, the mass in the system is regulated by equation 3.38:

$$\frac{d\rho(R)}{dt} = -\frac{dF}{dR} \tag{3.38}$$

with $\rho(R)$ being the number density of particles of radius R and F the particle flux in the size space.

The flux F can therefore be expressed as $\rho(R).v_t(R)$, with $v_t(R)$ is the rate of evolution for particles of size R. This rewrites equation 3.38 as:

$$\frac{d\rho(R)}{dt} = -\frac{d(\rho(R).v_t(R))}{dR}. \tag{3.39}$$

Using the aforementioned discretization of the size space and by applying a finite differences scheme, equation 3.40 can be written:

$$\frac{\rho_{t+\Delta t}(R) - \rho_t(R)}{\Delta t} = -\left[\frac{\rho(R+\Delta R).v_t(R+\Delta R) - \rho(R).v_t(R)}{\Delta R}\right]_\theta. \tag{3.40}$$

To ensure that the integration is stable and its convergence is not dependent on the value of the time step, a Euler implicit scheme is used ($\theta = t + \Delta t$) and it is given by equation 3.41:

$$\frac{\rho_{t+\Delta t}(R) - \rho_t(R)}{\Delta t} = -\left[\frac{\rho_{t+\Delta t}(R+\Delta R).v_t(R+\Delta R) - \rho_{t+\Delta t}(R).v_t(R)}{\Delta R}\right]. \tag{3.41}$$

This is simplified as follows:

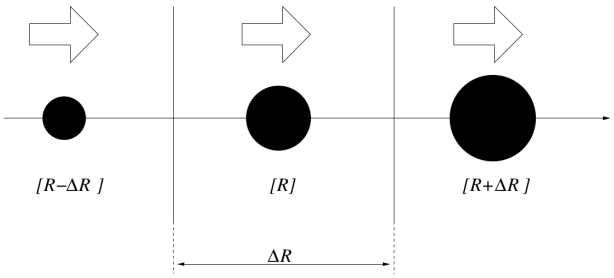

Figure 3.14 – Schematic of the particle flux management in the size space between size classes $R - \Delta R$ and $R + \Delta R$ [13].

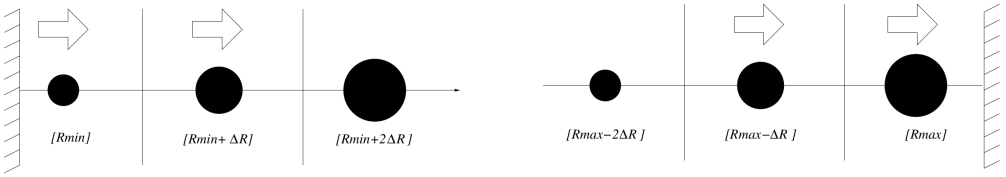

Figure 3.15 – Schematic of the particle flux management in the size space for the boundary cases: (a) The smallest size class of size R_{min} and (b) The biggest size class of size R_{max} [13].

$$\rho_{t+\Delta t}(R).[P] = \rho_{t+\Delta t}(R-\Delta R).[G] + \rho_{t+\Delta t}(R+\Delta R)[D] + \rho_t(R).\left[P^0\right], \quad (3.42)$$

with $[P]$, $[G]$, $[D]$, and $[P^0]$ being computation parameters. It is important to note at this point that each size class R exists in between two size classes $R-\Delta R$ and $R + \Delta R$. There is however two boundary cases at the extremities where the smallest and biggest size classes, R_{min} and R_{max} respectively, have only one neighboring size class.

For size classes within $]R_{min}, R_{max}[$ there are four flux management possibilities as displayed in Figure 3.14. The corresponding computation parameters are obtained by appreciating the direction of the fluxes in the size class and its neighbours. A summary of the resulting parameters for each case is given in Table 3.1.

For the boundary cases R_{min} and R_{max} (represented in Figure 3.15a and 3.15b respectively), the finite differences scheme must be decentered on $R + \Delta R$ and $R - \Delta R$ respectively. The same treatment for non centered schemes as the one presented in Table 3.1 is therefore used for these cases.

In order to solve equation 3.42 and obtain $\rho_{t+\Delta t}(R)$ for each size class, this equation is written in matrix form. Using the following notations:

Table 3.1 – Values of the parameters C, L, R and C^0 of equation 3.42 as a function of the directions of the fluxes for the particules in $]R_{min} : R_{max}[$ [13].

Direction of flux in $R-\Delta R$	Direction of flux in R	Direction of flux in $R+\Delta R$	Finite differences scheme	P	G	D	P^0
positive	positive	-	decentered on $R-\Delta R$	$\frac{\Delta R}{\Delta t}+v_t(R)$	$v_t(R-\Delta R)$	0	$\frac{\Delta R}{\Delta t}$
-	negative	negative	decentered on $R+\Delta R$	$\frac{\Delta R}{\Delta t}-v_t(R)$	0	$-v_t(R+\Delta R)$	$\frac{\Delta R}{\Delta t}$
positive	-	negative	centered on R	$\frac{2.\Delta R}{\Delta t}$	$v_t(R-\Delta R)$	$-v_t(R+\Delta R)$	$\frac{2.\Delta R}{\Delta t}$
negative	-	positive	centered on R	$\frac{2.\Delta R}{\Delta t}$	$v_t(R-\Delta R)$	$-v_t(R+\Delta R)$	$\frac{2.\Delta R}{\Delta t}$

$$\begin{cases} \rho_t(R) & = \rho_n^i, \\ \rho_{t+\Delta t}(R) & = \rho_{n+1}^i, \\ \rho_{t+\Delta t}(R+\Delta R) & = \rho_{n+1}^{i+1}, \\ \rho_{t+\Delta t}(R-\Delta R) & = \rho_{n+1}^{i-1}. \end{cases} \tag{3.43}$$

Equation 3.42 becomes:

$$\rho_n^i = \rho_{n+1}^{i-1}.\frac{[-G]}{[P^0]} + \rho_{n+1}^i.\frac{[P]}{[P^0]} + \rho_{n+1}^{i+1}.\frac{[-D]}{[P^0]}. \tag{3.44}$$

It shows how it is possible to build the term on the right as the sum of three matrices (diagonal, lower diagonal and upper diagonal). It can therefore be written in matricial form:

$$\begin{cases} \sum_j \delta_{[i,j]} = \mathbb{1}, \\ \sum_j \delta_{[i+1,j]} = M_{[i,j]}^{sup}, \\ \sum_j \delta_{[i-1,j]} = M_{[i,j]}^{inf}. \end{cases} \tag{3.45}$$

Matrix $M_{[i,j]}^{sup}$ is a matrix where terms for which $j = i+1$ are equal to 1 and 0 everywhere else. It is therefore associated to the upper diagonal term in equation 3.44. On the other hand $M_{[i,j]}^{inf}$ is associated to the lower diagonal matrix and $\mathbb{1}$ is associated to the diagonal term.

Factorising equation 3.44 leads to the general matrix form of the problem given by equation 3.46. Recall that the boundary conditions R_{min} and R_{max} are automatically taken into account by properly evaluating the computation the parameters. The general matrix form of the problem becomes:

$$\rho_n = \rho_{n+1}\left(-M_{[i,j]}^{inf}.\frac{[G]}{[P^0]} + \mathbb{1}.\frac{[P]}{[P^0]} - M_{[i,j]}^{sup}.\frac{[D]}{[P^0]}\right). \tag{3.46}$$

Which is equivalent to the following generic form:

$$\rho_n^i = \sum_j \mathcal{D}_{[i,j]} \rho_{n+1}^j \tag{3.47}$$

where the matrix $\mathcal{D}_{[i,j]}$ is a tridiagonal matrix defined as:

$$\mathcal{D}_{[i,j]} = \begin{pmatrix} \frac{P[1]}{P[1]^0} & -\frac{R[1]}{P[1]^0} & 0 & 0 \\ -\frac{L[2]}{P[2]^0} & . & . & 0 \\ 0 & . & . & -\frac{R[n-1]}{P[n-1]^0} \\ 0 & 0 & -\frac{L[n]}{P[n]^0} & \frac{P[n]}{P[n]^0} \end{pmatrix}.$$

It is therefore possible to compute ρ_{n+1}^j by inverting the tridiagonal matrix. This can be achieved numerically using a tridiagonal matrix algorithm (TDMA) which is an efficient algorithm. This constitutes one of the main advantages of the KWN method in tracking the evolution of size distributions of precipitates.

Another major advantage is its compatibility with nucleation theory. The size classes are filled using the particle flux described in the previous section. The model is therefore capable of handling the simultaneousness of the processes of nucleation and growth. It allows simulations of anisothermal heat treatments where nucleation events can occur multiple times during the treatment.

In addition to that, the transition to the ripening regime is done intrinsically. Even if the matrix supersaturation is close to 0, the Gibbs-Thomson effect still modifies the interfacial compositions in a size-dependent manner. Particles of small sizes dissolve and those with bigger sizes continue growing. It is also important to continuously evaluate the mean compositions as described earlier in order to ensure mass conservation in the system.

Recall that central element of this model is the growth rate of the precipitating particle. In light of what was presented so far, the system of non linear equations that determine it is as follows:

$$\begin{cases} \dfrac{dR(t)}{dt} = \dfrac{D_{Mg}^{\alpha}}{R(t)} \dfrac{(\bar{C}_{Mg}^{\alpha} - C_{Mg}^{\alpha/\beta})}{(C_{Mg}^{\beta} - C_{Mg}^{\alpha/\beta})}, \\ \dfrac{dR(t)}{dt} = \dfrac{D_{Si}^{\alpha}}{R(t)} \dfrac{(\bar{C}_{Si}^{\alpha} - C_{Si}^{\alpha/\beta})}{(C_{Si}^{\beta} - C_{Si}^{\alpha/\beta})}, \\ \log[(C_{Mg}^{\alpha,eq})^2 . C_{Si}^{\alpha,eq}] = -7144.T^{-1} + 2.7, \\ C_{Mg}^{\alpha/\beta} = C_{Mg}^{\alpha,eq} . \exp\left(\dfrac{2.g.\gamma.V^{\beta}}{C_{Mg}^{\beta}.R.k_B.T}\right), \\ C_{Si}^{\alpha/\beta} = C_{Si}^{\alpha,eq} . \exp\left(\dfrac{2.g.\gamma.V^{\beta}}{C_{Si}^{\beta}.R.k_B.T}\right). \end{cases} \tag{3.48}$$

Solving this system for the growth rate relies on finding a set of equilibrium concentrations $C_{Si}^{\alpha,eq}$ and $C_{Mg}^{\alpha,eq}$ that satisfy the kinetic and thermodynamic constraints. This is achieved using a Newton-Raphson numerical resolution scheme.

The equations in system 3.48 are combined to produce a single equation in which the only unknown is one of the equilibrium concentrations. This happens to come down to finding the roots of a third degree polynomial. The function is therefore regular and its derivative is simple. The algorithm is therefore set to find a root between 0 and 1 which it is capable of achieving quite efficiently.

Regarding the discretization of the size space, a minimum radius is introduced. Essentially, a particle the size of which is smaller than the lattice parameter is considered non-existent. The minimum radius is therefore set to 0.2 nm (i.e. a diameter of 0.4 nm, which is about one lattice parameter).

An adaptive time step management was also necessary in order to ensure that the solver respects a 1D Courant–Friedrichs–Lewy (CFL) type condition. This condition ensures that displacement in the size space, i.e. particles moving from one class to another, within the Δt timestep does not skip over classes. It is formulated according to inequality 3.49:

$$\Delta t \leq \frac{\Delta R}{\dot{R}} \tag{3.49}$$

where ΔR is the size space discretization step and $\dot{R}$ the calculated growth rate. Within the loop over the size classes, the maximal admissible value of the time step, Δt_{adm} is defined according to this condition. The timestep is therefore set with $\Delta t = u\Delta t_{adm}$, u being a precision coefficient between 0 and 1. An upper limit, Δt_u, is systematically set to avoid large leaps in time when the condition allows it. The solver algorithm for the entire precipitation model is presented in flow-chart form in Figure 3.16.

3.3.1 Model parameters

The model parameters and their values are compiled in Table 3.2. The diffusion coefficients for Mg and Si are assumed to be given by an Arrhenius law (equation 3.50):

$$D_i = D_i^0 . \exp\left(\frac{Q_i}{\mathcal{R}T}\right) \tag{3.50}$$

with D_i being the diffusivity of element i, D_i^0 its pre-exponential factor and Q_i its activation energy for diffusion.

The interfacial energy γ was split into two values, γ^{nuc} applying for the nucleation theory equations and γ^{gro} applying for the Gibbs-Thomson effect. This was found to make the model more capable of handling the transition from nucleation/growth to ripening.

There is a wide range of values in literature for the interfacial energies. In the publications where authors perform no comparison to experiments, this value is chosen arbitrarily within an acceptable range taking into account the nature of the phase and its coherence. In other publications where experiments are used as calibration, the values for the interfacial energy were chosen so as to give the best

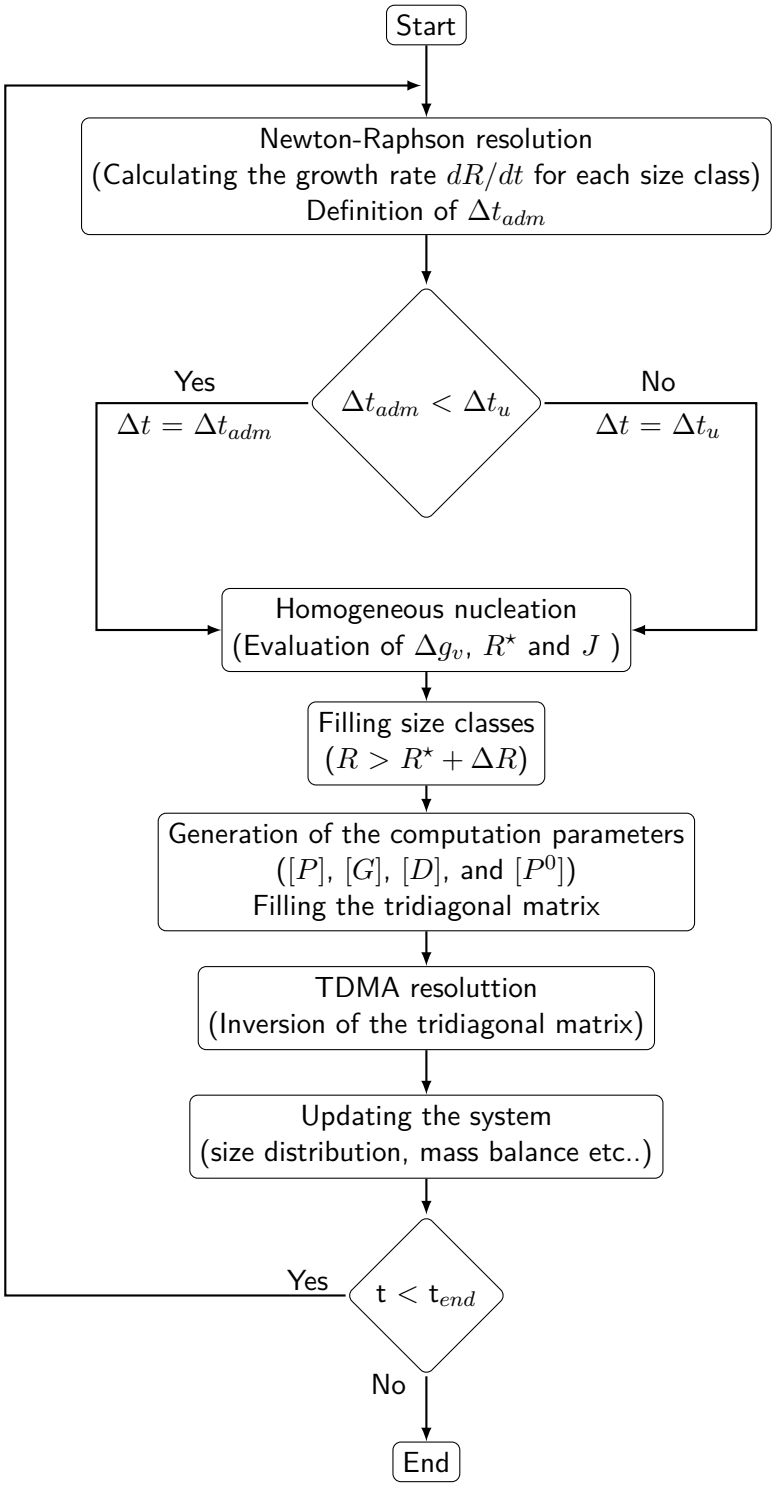

Figure 3.16 – Flow-chart describing the solver algorithm used for the precipitation model of β''-Mg_2Si in this work.

possible fit to said experiments. In this work, the values for the interfacial energy were chosen in this manner. The simulated size distributions were compared to

the experimental results presented in the previous chapter.

Table 3.2 – Summary of the precipitation model parameters and the values used in this work.

Model parameter	Symbol	Value	Unit	Source
α-Al lattice parameter	a	4.05×10^{-10}	m	[53]
Molar volume of α-Al	V_m^α	1.02×10^{-5}	$m^3.mol^{-1}$	TCAL5[1]
Molar volume of β-Mg_2Si	V_m^β	1.29×10^{-5}	$m^3.mol^{-1}$	TCAL5[1]
Activation energy for diffusion of Mg in α-Al	Q_{Mg}	120500	J	[85]
Activation energy for diffusion of Si in α-Al	Q_{Si}	117600	J	[85]
Pre-exponential factor of Mg diffusivity in α-Al	D^0_{Mg}	1.49×10^{-5}	$m^2.s^{-1}$	[85]
Pre-exponential factor of Si diffusivity in α-Al	D^0_{Si}	1.38×10^{-5}	$m^2.s^{-1}$	[85]
Molar fraction of Mg in β-Mg_2Si	C^p_{Mg}	0.666	-	Stoechiometry
Molar fraction of Si in β-Mg_2Si	C^p_{Si}	0.334	-	Stoechiometry
Interfacial energy for nucleation	γ^{nuc}	142	$mJ.m^{-2}$	This work[2]
Interfacial energy for growth	γ^{gro}	54	$mJ.m^{-2}$	This work[2]

[1]: averaged over temperatures between 20°C and 540°C.
[2]: fit parameters

3.4 Simulation results

To present the simulation results and compare them to the experiments, the model was given as input the same thermal history that was studied experimentally. This thermal history is given in Figure 3.17. It consists in quenching from a solutionizing temperature of 540°C down to room temperature with a cooling rate of 4.3°C/s, followed by a natural aging period and then heating to the aging temperature of 200°C with a rate of 0.2°C/s and holding for 100 hours. The dotted lines refer to the end of quenching, the beginning of the heating ramp and the beginning of the aging heat treatment. These dotted lines will be used in the same order for all the graphs depicting kinetic variables output by the model.

The response of the nucleation model is given in Figure 3.18. It shows that the model predicts two nucleation peaks, the first one occuring during quenching and the second one in the middle of the heating ramp from room temperature to 200°C. This explains the two-step increase in the total number density of precipitates, which is essentially the area under the nucleation peaks. The effect of these two nucleation rate peaks can also be observed in Figure 3.19. First, there is a two-step increase in the volume fraction as well which going hand in hand with the total number density of precipitates. Then there are two dips in the mean radius, each occuring as a result of the nucleation rate peaks. Indeed, with each nucleation rate peak, the system is flooded by a considerable number of precipitates of small size which explains this dip.

According to Figure 3.19, the volume fraction evolves in two sharp steps. However, right after the second step, there seems to be an episode of pure growth

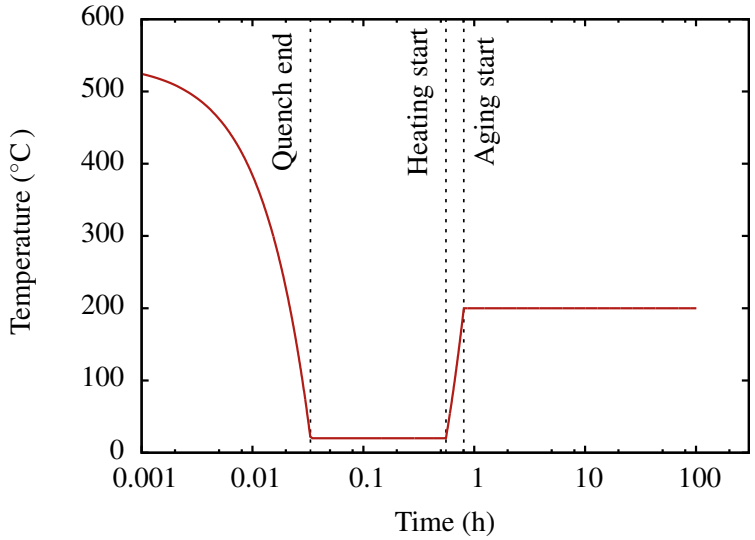

Figure 3.17 – Simulated thermal history for the solutionizing and aging heat treatment of the A356+0.5Cu alloy.

without any nucleation events. Volume fraction later stabilises at a value close to 0.009 which is nearly exactly the equilibrium volume fraction of the β phase predicted by Thermo-Calc at 200°C (metastable calculation where the Q-phase is suppressed).

Judging by Figure 3.18, it appears that ripening starts to take place early in the aging heat treatment. Indeed the total number density of precipitates starts to decrease progressively as aging duration increases. There is however no sharp distinction between the regimes of growth and coarsening. This can be explained by the fact that numerically, an actual equilibrium where the oversaturation is null and the volume fraction is strictly constant is never reached. This can be observed in Figure 3.20 where the oversaturation both in terms of Mg and Si does decrease as precipitation occurs, but without ever reaching zero.

As mentioned above, the interfacial energies were used as fitting parameters for the model. This fit was performed by qualitatively comparing the simulated and the experimental size distributions. The experimental size distributions were produced for the diameter and length of the rod shaped β'' precipitates. It is worth noting that the diameter and length were not measured for the same particles (different TEM viewing directions). This means that what is refered to here as the average aspect ratio is the aspect ratio of the average particle (i.e. $<\lambda>=<l>/<d>$).

In order to produce simulation variables comparable to the experiments, we start by equating the volume of the rod shaped particle, V^{Rod}, to that of a sphere of equivalent volume, V^{SEV} (equation 3.51):

$$V^{Rod} = V^{SEV}. \tag{3.51}$$

This leads to linking rod length l and diameter d to the radius of the sphere of equivalent volume R (i.e. the KWN radius) using equations 3.52 and 3.53. A

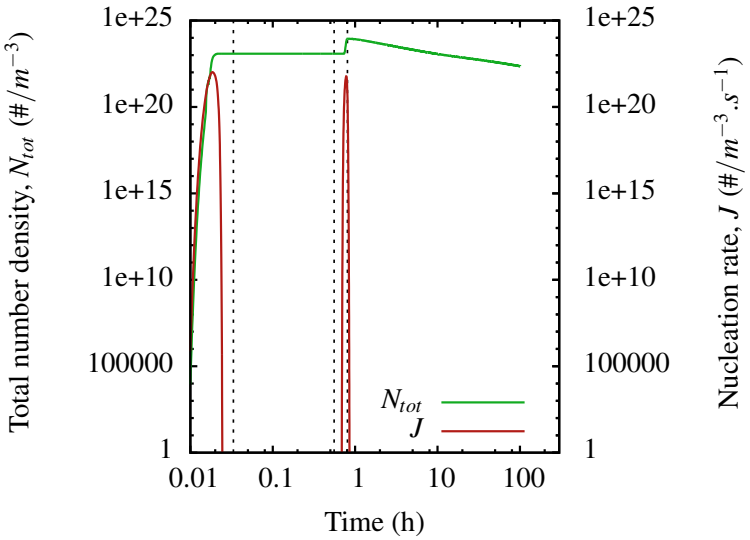

Figure 3.18 – Simulated evolution of the nucleation rate, J, and the total number density of precipitates, N_{tot}.

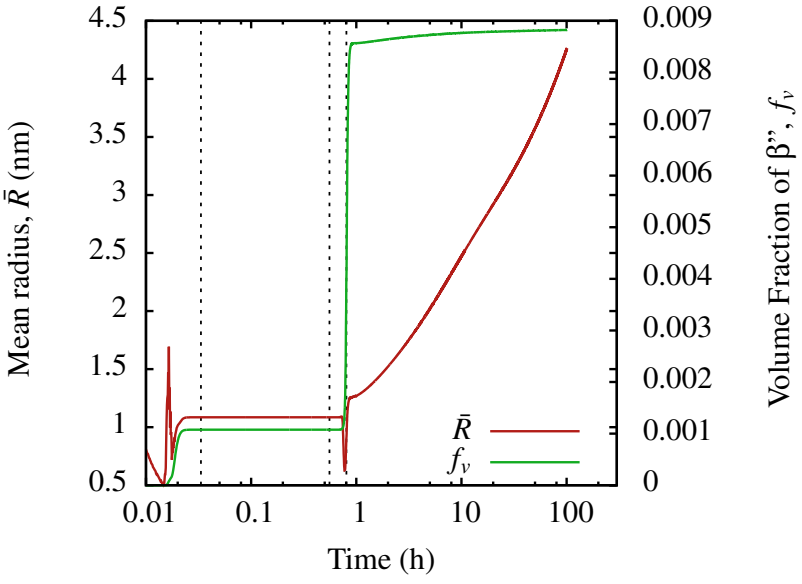

Figure 3.19 – Simulated evolution of the mean radius, $\bar{R}$, and volume fraction, f_v, of the precipitating phase β''.

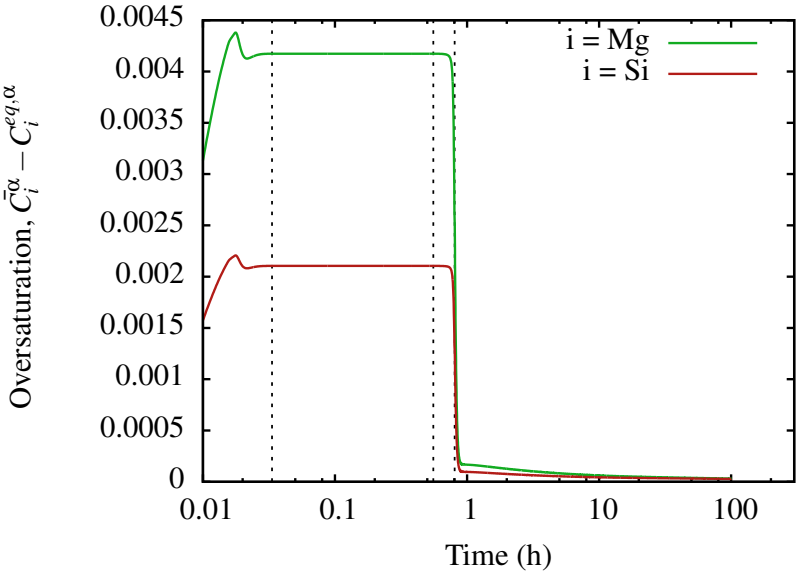

Figure 3.20 – Simulated evolution of the matrix oversaturation for solute elements Mg and Si.

simulated length and diameter can therefore be obtained by using the value of the average aspect ratio given in the previous chapter ($\lambda = 6.6$):

$$l = 2.R.\sqrt[3]{\frac{2}{3} < \lambda >^2}, \tag{3.52}$$

$$d = 2.R.\sqrt[3]{\frac{2}{3. < \lambda >}}. \tag{3.53}$$

The comparison between the experimental and simulated size distributions is given in figure 3.21. Recall that size distribution of length for the 0.1 hour aging duration was not determined experimentally. Overall, the model appears to be in good agreement with the experiments. The early stages of aging (the 0.1 and 1 hour cases) are very well represented. For the 10 hour case, the model gives good agreement in terms of the mean radius and length. However, the model gives a narrower distribution of radius and length in comparison to the experiments. This may be an indication of a breakdown due to the assumption of a constant aspect ratio. It was observed in the work of Du *et al.* [82] that using a varying aspect ratio produced slightly wider size distributions.

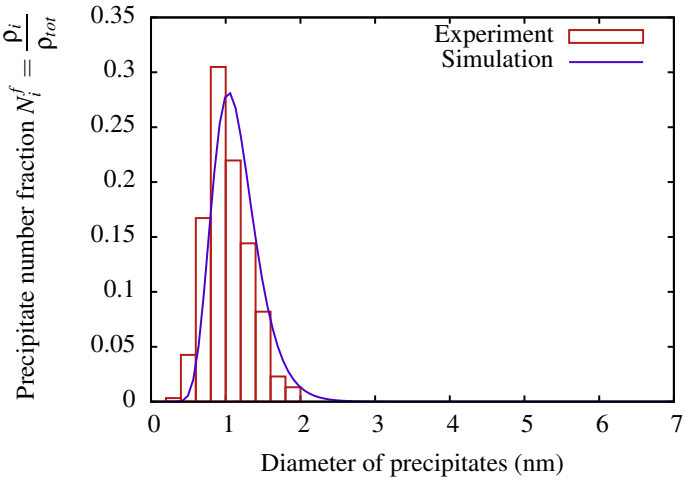

(a) Aged for 0.1 hr

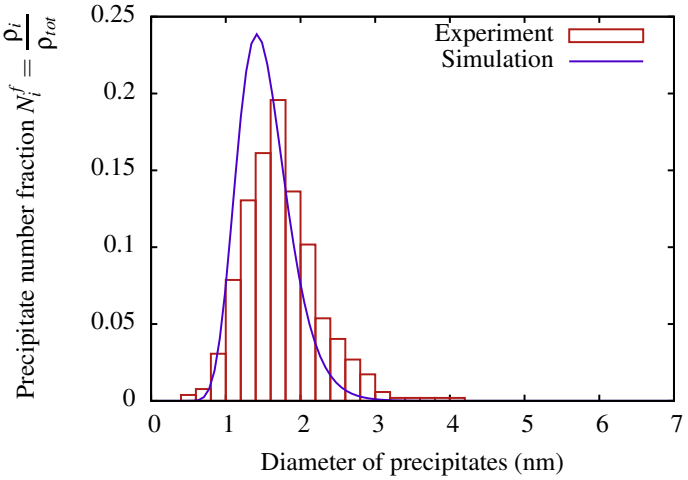

(b) Aged for 1 hr

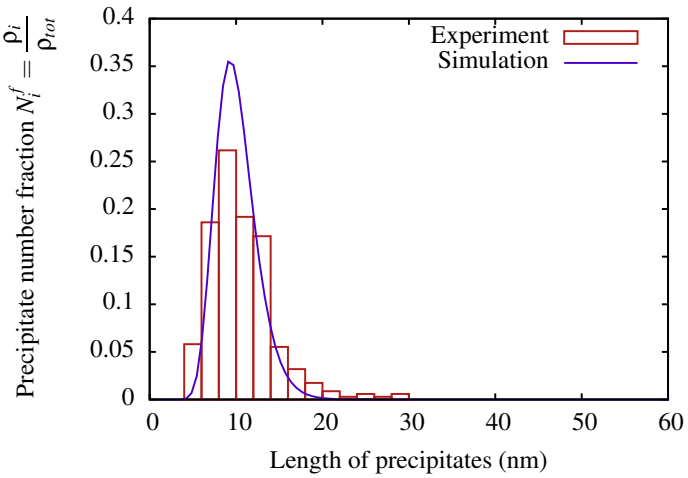

(c) Aged for 1 hr

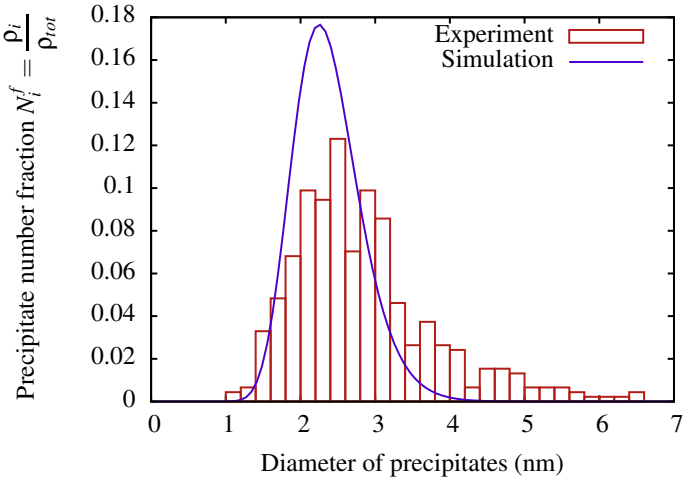

(d) Aged for 10 hr

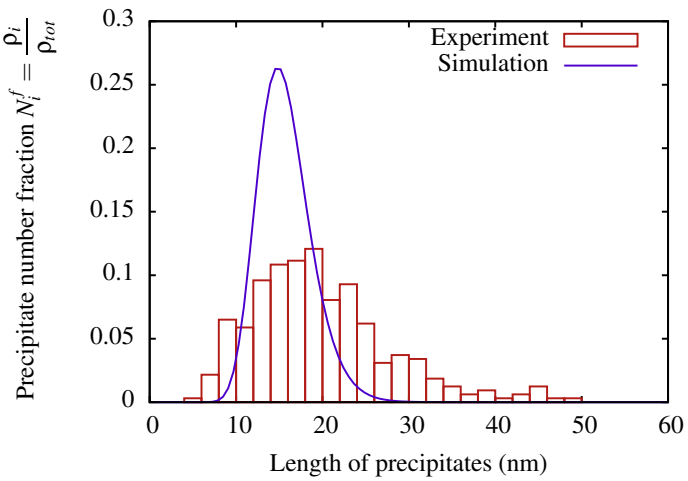

(e) Aged for 10 hr

Figure 3.21 – Comparison between the experimental and simulated size distributions of β''-Mg_2Si precipitates: (a), (b) and (c) diameter size distributions for aging durations of 0.1, 1 and 10 hr respectively, (c) and (e) length size distributions for aging durations of 1 and 10 hours at 200°C respectively.

3.5 Conclusion

The precipitation kinetics of the hardening phase β''-Mg_2Si in the studied A356+0.5Cu alloy was modelled using nucleation and growth theory. In the model, the precipitating phase was considered to be the stable β-Mg_2Si for the sake of simplicity. Correction factors were introduced in the growth rate equation and the Gibbs-Thomson effect equation to take into account the rod morphology of the precipitates. Modelling of compound phases where two elements diffuse in the matrix necessitated the formulation of thermodynamic and kinetic constraints in order to correctly evaluate the growth rate.

The precipitation driving force and the solubility product were both evaluated using Thermo-Calc/TCAL5. They were introduced in the model through indirect coupling whereby prior thermodynamic calculations were performed and numerically fitted. Parameters such as the molar volumes of precipitates were also calculated using Thermo-Calc.

The KWN method, paired with a Euler explicit finite differences scheme were used to write a matrix form of the time dependent size distributions of precipitates. Prior to that, a Newton-Raphson algorithm is used to evaluate the growth rate such that it abides by the thermodynamic and kinetic constraints.

The model was then utilized to simulate the heat treatment sequence that was experimentally studied. It was therefore calibrated by comparing simulated and experimental size distributions using the interfacial energy as fitting parameter. Two separate values of the interfacial energy were used, one for the nucleation equations and the other for the growth rate equations. Overall, the model was capable of correctly representing the size distributions, especially in terms of the mean diameter. The width of the distributions were slightly less well represented for the long aging duration of 10 hr.

In the following chapter, the results of the precipitation kinetics model will be used as inputs for a yield stress model. Indeed, outputs of the precipitation model such as the time-dependent size distributions, volume fraction and solute contents will be used. An estimation of yield stress will be provided on the basis of different contributions that are fully dependent on the precipitation state.

Chapter 4

Yield stress model and finite element computations

Résumé

La limite d'élasticité a été modélisée avec un modèle additif, prenant en compte la contribution de la résistance intrinsèque de la matrice aluminium, le durcissement par solution solide et la précipitation. Les équations évaluant ces diverses contributions se basent sur les résultats du modèle de précipitation présenté au chapitre précédent.

Dans ce chapitre, les équations servant à l'estimation de la limite d'élasticité de façon informée par l'évolution microstructurale sont présentées. Les simulations sont ensuite confrontées aux résultats expérimentaux de la limite d'élasticité afin de caler et valider la modélisation.

Le mode de couplage du modèle à la méthode des éléments finis est exposé. La chaîne de calcul comprenant la thermique, le modèle de précipitation et de limite d'élasticité et la mécanique est ensuite détaillée. Un calcul 2D a été effectué en utilisant cette chaîne pour démontrer sa capacité à représenter les gradients de propriétés et à estimer les contraintes résiduelles issues des traitements thermiques de trempe.

4.1 Origin of yield stress

Yield stress is the material property which expresses the stress at which the material starts to deform irreversibly (plastic deformation). At the atomic scale, considering a monocrystal, applying shear stress results in the displacement of dislocations within the crystal (Figure 4.1). Once a dislocation reaches a free surface, a step appears and the material is therefore permanently deformed. The movement of dislocations is activated by the applied shear stress and can also be assisted by temperature dependent diffusive mechanisms. It is worth noting that dislocation motion is not the only plastic deformation mechanism that exists. Twinning and phase transformation induced plasticity are additional mechanisms that will not be discussed in this work.

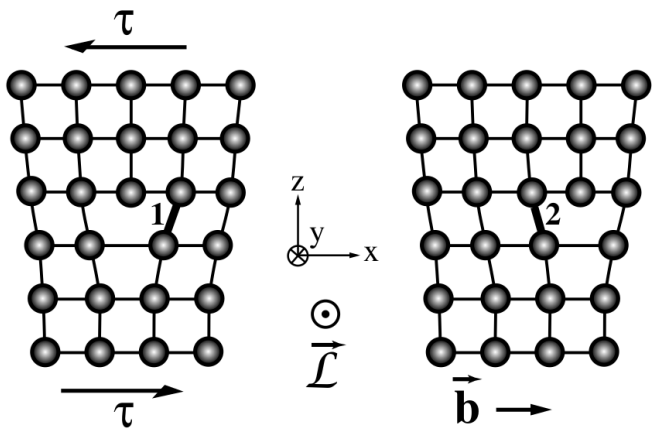

Figure 4.1 – Schematic of an elementary displacement of an edge dislocation under an applied shear stress τ. $\vec{L}$ is the dislocation line vector and $\vec{b}$ its Burgers vector [86].

Setting aside thermal activation, the applied shear stress required to move a dislocation is called the critical resolved shear stress (CRSS), τ_c which is dependent only on the crystal structure. The resolved shear stress is the projection of the applied stress on the dislocation slip plane and along its slip direction (Figure 4.2). Considering a monocrystal under a simple unidirectional tensile stress, Schmid and Boas [87] write the well known projection given by equation 4.1:

$$\tau = \frac{F}{S} \cos\phi \cos\lambda \tag{4.1}$$

with τ being the resolved shear stress, F the load, S the cross section normal to the tensile direction, ϕ the angle between the tensile direction and the normal to the slip plane and λ the angle between the tensile direction and the slip direction.

The Schmid factor, M_s, refers to the expression $\cos\phi\cos\lambda$ and has a maximum value of 0.5 (corresponding to a value of 45° for θ and λ). Dislocation slip systems in a crystal are characterized by a plane and a direction of slip. It is well

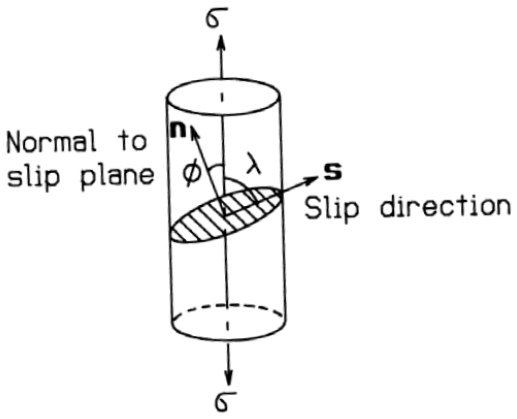

Figure 4.2 – Schematic of the projection of a tensile stress σ on the slip plane along the dislocation slip direction [87].

established that for any given crystal structure, slip occurs in the dense planes along dense directions. For FCC crystals, these systems consist of the 12 variations of $\frac{1}{2}\langle 1\bar{1}0\rangle\{111\}$. For any given stress direction, it is the slip system with the highest Schmid factor that will be engaged. A monocrystal is therefore inherently plastically anisotropic.

The transition from monocrystals to the polycrystals requires certain considerations. A polycrystal can be viewed as a collection of monocrystals (grains) having different crystallographic orientations. Therefore, in the absence of a strong texture, a polycrystal can be considered isotropic. This is because it is no longer possible to deform the material on only one slip system since grains of different orientations would deform heterogeneously under a given applied stress. For a dislocation to continue its movement across a grain boundary, the grains have to be "compatible", i.e. able to accommodate the dislocation. This constitutes a hindrance in the movement of dislocations meaning that the CRSS depends also on the geometric arrangement of crystals and texture.

The transition rules are based on hypotheses regarding the local stress and deformation fields in a material subject to a load. One hypothesis attributed to Sachs [88] is that of uniform stress across the polycrystal equal to the macroscopic applied stress. Assuming a large enough number of distinct crystallographic orientations and the absence of texture it is inevitable for some grains to be oriented such that their Schmid factor is maximal. The CRSS can therefore be considered as the stress required to activate the most favorably oriented slip systems in each grain. It can be shown that for a FCC material subject to unidirectional tensile stress, the ratio M_s between the applied stress and the resolved shear stress takes a value of 2.24. This value constitutes a lower limit to the yield stress.

A second hypothesis formulated by Taylor [89] is that of uniform plastic deformation across the polycrystal equal to the macroscopic plastic strain. This offers an upper limit to the yield stress and it can be shown that for an FCC material subject to unidirectional tensile stress $M_s = 3.06$.

Since yield stress is linked to the stress required for dislocation motion, the presence of obstacles to this motion provides strengthening. The effective yield stress can therefore be considered as the stress required to overcome the sum of the contributions of these obstacles in resisting dislocation motion.

4.2 Contributions to yield stress

4.2.1 Peierls-Nabarro stress

Dislocation slip consists in breaking atomic bonds along the dislocation line which requires energy [90]. This intrinsic resistance to dislocation motion is known as the Peierls-Nabarro stress [91]. It is intrinsic in the sense that it depends only on the properties of the dislocation core which in turn depend on the nature of the crystal. The Peierls-Nabarro stress, τ_{pn}, can be expressed using equation 4.2:

$$\tau_{pn} = \frac{\mu b^2}{\pi(1-\nu)} \exp\left(-\frac{2\pi\omega}{b}\right) \tag{4.2}$$

with μ being the shear modulus, b the magnitude of the Burgers vector, ν the Poisson ratio and ω the width of the dislocation core. In FCC materials this contribution is small, with reported orders of magnitude smaller than 10 MPa [92]. This contribution becomes increasingly insignificant as temperature increases since thermal agitation assists in breaking atomic bonds.

4.2.2 Solid solution strengthening

When solute atoms are introduced in a solid solution they represent point defects in the matrix. The interaction of these solute atoms with dislocations on multiple levels produces a strengthening effect. Firstly, the presence of an atom of a different size in a matrix creates an isotropic distortion of the crystal lattice around it. The magnitude of this distortion is characterized by the geometric misfit value, δ. The elastic strain field around the solute atom becomes more important as the misfit increases. Dislocations movement is hindered by the presence of these strain fields. Secondly, solute atoms change the interatomic bonding forces which locally changes the elastic modulus. This also results in a disturbance for dislocation motion. Thirdly, high solute concentrations can result in chemical segregation and clustering which makes for an even larger obstacle for dislocation motion. Finally, there can be electrostatic interactions between solute atoms and dislocations which are comprised of matrix atoms. For most crystalline materials, this effect is not as dominant as the previously mentioned elastic interaction effects.

At temperatures high enough to activate the diffusion of solute atoms, they can migrate to dislocation cores and produce a pinning effect. However, as high temperatures also assist dislocation motion, this effect can only occur if the velocity of dislocation motion is close to that of the diffusing atoms [93, 94]. Increasing the applied stress allows dislocations to gain in velocity and break free from the

solute atoms pinning them. Once free, the stress decreases and with it the velocity of the dislocation which allows solute atoms to regain its core and pin it anew. The repetition of this process known as the Portevin-Le Chatelier effect produces instabilities in the plastic region of the stress-strain response of the material [95].

Evidently, the contribution of solid solution strengthening, τ_{ss}, is more important when their concentration is increased [96]. For a dislocation of length L_d, τ_{ss} is given by equation 4.3 where k_{ss} is a scaling factor dependent on the chemical element and C the atomic concentration of this element:

$$\tau_{ss} = k_{ss}\frac{\mu b}{2L_d}C^{2/3}. \tag{4.3}$$

4.2.3 Precipitation hardening

Precipitates are three dimensional defects in the crystal structure of the matrix which constitute an obstacle for dislocation motion thus contributing in strengthening the material. When a mobile dislocation meets a precipitate in its slip plane it can either shear it or bypass it. Multiple considerations determine which of the two mechanisms takes place.

Chief among these considerations is the coherence of the precipitates with the matrix. Indeed, in order to shear a precipitate, the dislocation must be able to continue its motion through the precipitate thus requiring continuity between the atomic planes of the matrix and the precipitate. Coherent and semi-coherent precipitates can present this crystallographic continuity thus allowing them to be sheared. Incoherent precipitates cannot be sheared and are therefore bypassed according to the Orowan mechanism.

Even if a precipitate is shearable it is possible for the strain field around it to exert a repulsive force which acts at a distance [97]. This can prevent certain dislocations from reaching the matrix/precipitate interface. Also, considering a population of precipitates of a given size distribution and spacing in the slip plane, it is possible for it to be energetically favorable for a dislocation to bypass them rather than shear them.

Considering a normal distribution of equidistant spherical precipitates with a mean radius $\bar{R}$ and a standard deviation of $0.25\bar{R}$, Deschamps *et al.* [98] showed that the hardening contributions of shearable precipitates, τ_{sh}, and non-shearable precipitates, τ_{by}, can be written according to equations 4.4 and 4.5 respectively:

$$\tau_{sh} = 0.7k^{2/3}\mu\sqrt{\frac{f_v\bar{R}}{b}}, \tag{4.4}$$

$$\text{and} \quad \tau_{by} = 0.6\mu b\frac{\sqrt{f_v}}{\bar{R}} \tag{4.5}$$

with f_v the volume fraction and k a constant that can be determined by evaluating the critical radius R_{crit} of transition between shearing and bypassing.

By equating the shearing and bypassing forces given by equations 4.6 and 4.7 for a critical particle of radius R_{crit}, k can be written as per equation 4.8:

$$F_{sh} = k\mu bR, \tag{4.6}$$

$$F_{by} = 2\beta\mu b^2, \tag{4.7}$$

$$k = \frac{2\beta b}{R_{crit}} \tag{4.8}$$

with β being a scaling factor between 0.2 and 0.5.

4.2.4 Work hardening

Dislocations that are in motion in a crystal under shear stress interact via their strain fields. When the Burgers vectors of two dislocations of equal moduli are of opposite signs, these two exert an attractive force on each other. If they attract along a shared slip plane they can annihilate, i.e. the two half planes join to form a full plane and eliminating the two dislocations. Conversly, dislocations for which the Burgers vectors have the same sign exert a repulsive force on one another. Therefore, dislocations can themselves be obstacles to the propagation of other dislocations thus providing a strengthening effect. Evidently, the higher the number density of dislocations the more significant this strengthening becomes.

On the one hand, the number density of dislocations can decrease, as mentioned before, as a result of the annihilation of dislocations having opposite signs. This can be practically induced by subjecting the material to annealing heat treatments. These treatments lead to a softening of the material. On the other hand, it is possible to increase the number density of dislocations through deformation. The mechanism of multiplication of dislocations was described by Charles Frank and Thornton Read after whom Frank-Read sources were named. A Frank-Read source is represented in Figure 4.3 and it consists of a dislocation pinned in two points [99]. Subject to an increasing shear stress and its own line tension, the dislocation bows out into an arc and spirals around the pinning points. These spiralling edges eventually come together and cancel forming a dislocation loop and a new dislocation between the pinning points. A further increase in the shear stress expands the dislocation loop and repeats the multiplication process between the pinning points for the newly created dislocation.

The contribution of work hardening to the yield stress, τ_w, is expressed using equation 4.9 as a function of the dislocation number density, ρ_d, with α being a constant representing the interaction between mobile and immobile dislocations (it takes values between 0 and 1):

$$\tau_w = \alpha\mu b\sqrt{\rho_d}. \tag{4.9}$$

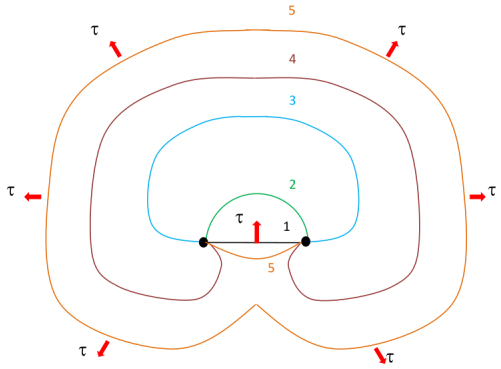

Figure 4.3 – Schematic of a Frank-Read source showing how applying shear stress τ on a pinned dislocation makes it multiply itself [8].

4.2.5 Grain size effect

In a polycrystal, grains have different orientations which can limit the range of motion of dislocations. Grain boundaries have a large atomic mismatch making it difficult for a dislocation to move from one grain to another. The grain boundaries therefore act as obstacles for dislocation motion. Once a dislocation is pinned at a grain boundary its repulsive stress field makes it more difficult for other dislocations to move in the same plane. Reducing the free range of motion can speed up the onset of this effect and it can be obtained by decreasing the size of the grains.

This effect is given by the Hall-Petch equation [100, 101] (equation 4.10) which phenomenologically expresses the strengthening contribution of grain size reduction, τ_{hp}, as a function of the average grain diameter, $\langle D \rangle$, and a material and temperature dependent parameter, k_{hp}:

$$\tau_{hp} = \frac{k_{hp}}{\sqrt{\langle D \rangle}}. \tag{4.10}$$

4.3 The yield stress model

The objective of the yield stress model is to be able to correctly represent the evolution of the yield stress of the studied A356+0.5Cu alloy subject to a heat treatment. The aim is to then reproduce in simulation the experimental aging curve obtained for the alloy for a temperature of 200°C. The yield stress model will be directly coupled to the previously described precipitation model. The calculated size distributions of precipitate, the volume fraction and solute concentrations at every time step will therefore serve as input variables for the yield stress model. A number of simplifications will be used to alleviate complexity and calculation cost.

Yield stress of a representative volume element of the FCC-Al phase will be considered as the macroscopic yield stress of the alloy. This means that the effect of the eutectic constituent will not be taken into account for simplification. As listed

before, there are multiple strengthening effects that contribute in the yield stress of the FCC matrix. However, not all of them will be explicitly taken into account. The contribution of initial work hardening will be neglected since the alloy is cast and heat treated without any applied plastic deformation. The Peierls-Nabarro stress and the Hall-Petch effect will be merged into a constant value σ_0 which will be chosen equal to 20 MPa.

The contributions that will be taken into account are those of precipitation hardening and solid solution strengthening. The superposition of these contributions will be done according to a simple additive rule given by equation 4.11 [102]:

$$\tau^q = \tau_1^q + \tau_2^q. \tag{4.11}$$

In this equation two contributions, τ_1 and τ_2 are summed according to a pythagorean law of exponent q. De Vaucorbeil *et al.* [102] used a dislocation line tension model to simulate the CRSS obtained when combining two distributions of obstacles of different strength. As shown in Figure 4.4, the authors constructed a map of values of q as a function of two different obstacle distribution strengths Φ_{1c} and Φ_{2c}. This strength is simply the breaking angle of the obstacle, i.e. the angle at which the dislocation must bow to around the obstacle to break free from it. It can be observed that when combining obstacle distributions of similar strength an exponent value of 2 must be used, and as the strength differential increases this exponent decreases all the way to a value of 1.

Applying this to the contributions that will be taken into account in this work, the addition law for yield stress will be written according to equation 4.12:

$$\sigma_y = \sigma_0 + (\sum_i \sigma_{i,ss}^2)^{1/2} + (\sigma_{sh}^2 + \sigma_{by}^2)^{1/2} \tag{4.12}$$

where σ_y is the yield stress, $\sigma_{i,ss}$ is the individual solid solution strengthening contribution of element i, σ_{sh} and σ_{by} are the contributions of shearable and bypassed precipitates respectively. Indeed, the solid solution strengthening contributions of different elements are added with an exponent of 2 as they are considered similar. The same treatment is applied for the different types of precipitates. However, the overall addition rule uses an exponent of 1 as the difference between precipitation hardening, intrinsic strength and solid solution strengthening is significant.

The individual contribution of solid solution strengthening will be accounted for according to Leyson *et al.* [103] who expressed it using equation 4.13:

$$\sigma_{i,ss} = M k_i \bar{C_i}^{2/3} \tag{4.13}$$

where M is the Taylor factor and $\bar{C_i}$ is the mean molar fractions of element i in the matrix. The authors determined the values of the coefficients k_i using first principles and the discrete Fourier transform method. They reported values of 342, 137, and 348 MPa/at%$^{2/3}$ for Mg, Si and Cu, respectively.

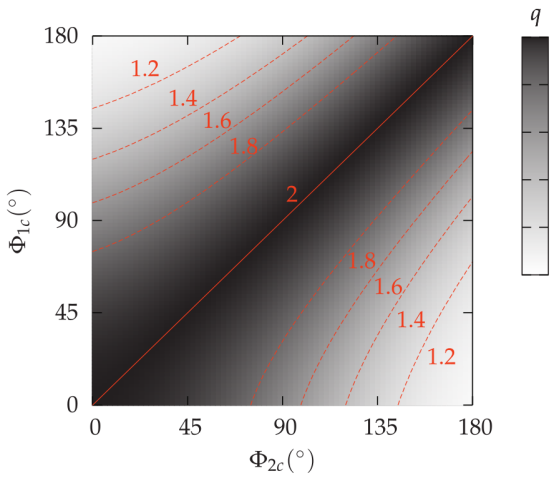

Figure 4.4 – The addition law exponent q as a function of the obstacle strength [102].

The strengthening effect due to precipitates will be calculated by assessing the contributions of the entire size distribution as proposed by Deschamps *et al.* [98]. Contrary to a mean radius approach, this approach is able to factor in the width of distributions as well as bimodal distributions. The necessary stress, σ_p, required for a dislocation to glide through a distribution of precipitates in its glide plane is given by equation 4.14:

$$\sigma_p = \frac{M\bar{F}^p}{b\bar{L}} \tag{4.14}$$

where $\bar{F}^p$ is the mean precipitate strength and $\bar{L}$ the average spacing between precipitates in the dislocation glide plane. The mean precipitate strength for a discretized size distribution of n classes can be written according to equation 4.15:

$$\bar{F^p} = \frac{\sum_i^n \rho_i F_i^p}{\sum_i^n \rho_i} \tag{4.15}$$

where ρ_i is the number density of precipitates in the size class i of radius R_i and strength F_i^p. Since the strengths of shearable and non-shearable precipitates are different (equations 4.6 and 4.7), the average strength of shearable precipitates $\bar{F_{sh}}$ and $\bar{F_{by}}$ can be written according to equations 4.16 and 4.17 respectively:

$$\bar{F_{sh}} = k\mu b \frac{\sum_{i<i_c} \rho_i R_i}{\sum_{i<i_c} \rho_i}, \tag{4.16}$$

$$\bar{F_{by}} = 2\beta\mu b^2 \tag{4.17}$$

where i_c is the size class corresponding to the critical radius for shearing, R_{crit}.

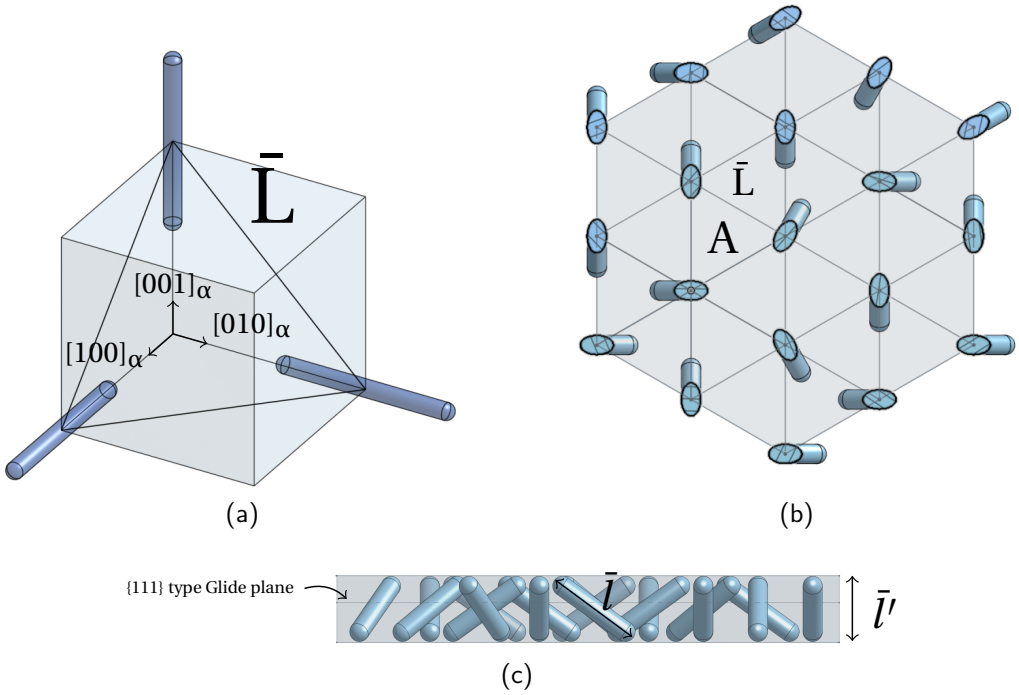

Figure 4.5 – Schematic representation of the β''-Mg_2Si precipitates : (a) cell constituted of the three families of orientations, (b) a section view of a population of precipitates cut with the dislocation glide plane of $\{111\}$ type and (c) side view of a population of precipitates of length $\bar{l}$.

The average precipitate spacing in the glide plane $\bar{L}$ is determined by considering a cell as shown in Figure 4.5a [11, 8]. In this figure, three precipitates belonging to each family of orientation (the three $[100]_\alpha$ directions) are positioned such that the spacing between them in the dislocation glide plane (111) is $\bar{L}$. The constituted triangle has an area given by equation 4.18 and it can be seen in Figure 4.5b that each precipitate is shared by 6 unit triangles:

$$A = \frac{\sqrt{3}}{4}\bar{L}^2. \tag{4.18}$$

The number of precipitates, n_A, in any given triangle is therefore exactly three sixths, i.e. $n_A = 1/2$. The precipitate number density per unit area is therefore $\rho_A = n_A/A$. Combining this with equation 4.18 leads to the expression of the average spacing according to equation 4.19:

$$\bar{L} = \sqrt{\frac{2}{\sqrt{3}\rho_A}}. \tag{4.19}$$

Figure 4.5c shows a population of precipitates of length $\bar{l}$ with a total number density of ρ being intersected by the dislocation glide plane. The number density per unit area can therefore be written according to equation 4.20, where P is the probability of intersecting at any given height:

$$\rho = P\rho_A. \tag{4.20}$$

The probability P is simply $1/\bar{l'}$, where $\bar{l'}$ is the height of the unit parallelepiped. This height is oriented along the [111] direction while $\bar{l}$ is oriented along [100] direction. They are therefore linked according to equation 4.21:

$$\bar{l'} = \bar{l}\cos([111],[100]) = \frac{\bar{l}}{\sqrt{3}}. \tag{4.21}$$

Combining equations 4.21 and 4.20 the number density per unit area can be expressed as follows:

$$\rho_A = \frac{\rho\bar{l}}{\sqrt{3}}. \tag{4.22}$$

Using $\rho = \sum_i^n \rho_i$ and $\bar{l} = \dfrac{\sum_i^n \rho_i l_i}{\sum_i^n \rho_i}$, equation 4.19 writes :

$$\bar{L} = \sqrt{\frac{2}{\sum_i^n \rho_i l_i}}. \tag{4.23}$$

This expression is valid only for bypassed precipitates as it is independent of the applied stress. Indeed, all bypassed particles have the same strength and the dislocation must form a complete loop around them to break free. The average spacing is therefore simply the center-to-center distance between precipitates in the dislocation glide plane given by equation 4.23. However, in the case of shearable precipitates, this average spacing depends on the precipitate strength.

According to the Friedel statistics [104, 105, 106] the average spacing between shearable precipitates is given by equation 4.24:

$$\bar{L}_{sh} = \frac{1}{\sqrt{\rho_A \cos\left(\dfrac{\Phi_c}{2}\right)}} \tag{4.24}$$

where Φ_c is the strength of the precipitate expressed as its breaking angle, i.e. the critical angle to which a dislocation must bow out to unpin itself. Figure 4.6 illustrates the equilibrium of forces acting on a precipitate about to be "broken" by a dislocation. Indeed the precipitate is subject to the dislocation tension, Γ, on both sides and its own resistance, F. The dislocation forms an angle of Φ_c around the precipitate at the unpinning moment. The equilibrium is such that equation 4.25 can be written:

$$F = 2\Gamma\cos\left(\frac{\Phi_c}{2}\right). \tag{4.25}$$

Combining equations 4.19, 4.24 and 4.25 leads to the expression of the average spacing between precipitates for the case of shearable precipitates (equation 4.26):

$$\bar{L}_{sh} = \sqrt{\frac{\sqrt{3}\Gamma}{\bar{F}}}\bar{L}. \tag{4.26}$$

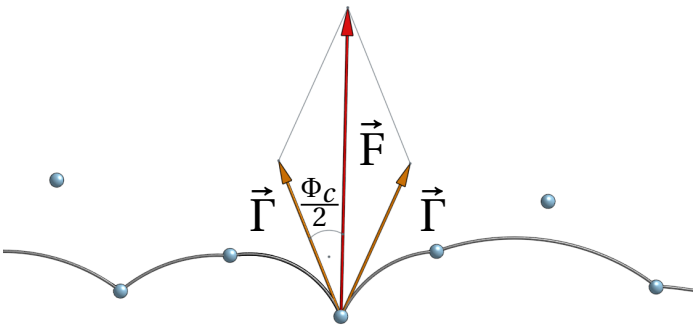

Figure 4.6 – Schematic illustration of the equilibrium of forces when a dislocation is pinned by an obstacle.

Finally, the set of equations presented so far leads to the expression of the contributions of shearable and bypassed precipitates to the yield stress of the material. By assuming a constant dislocation line tension $\Gamma = \beta\mu b^2$, equations 4.27 and 4.28 can be obtained to evaluate the hardening coming from sheared and bypassed precipitates:

$$\sigma_{sh} = M\mu \left(k \frac{\sum\limits_{i<i_c} \rho_i R_i}{\sum\limits_{i<i_c} \rho_i} \right)^{3/2} \left(\frac{\sum\limits_{i<i_c} \rho_i l_i}{2\sqrt{3}\beta b} \right)^{1/2}, \tag{4.27}$$

$$\sigma_{by} = \sqrt{2} M \beta \mu b \left(\sum_{i>i_c} \rho_i l_i \right)^{1/2}. \tag{4.28}$$

4.4 Simulation results

The yield stress model was calibrated using the tensile test results presented in chapter 2. The same thermal history used in the calibration of the precipitation model was simulated with the estimation of yield stress at each time-step (cf. Figure 3.17). The parameters of the yield stress model are summarized in Table 4.1.

Figure 4.7a shows the comparison between the simulated evolution of yield stress and the experimental results. Recall that the dotted lines represent, in order from left to right, the end of quenching (from 540°C to room temperature), the beginning of heating (from room temperature to 200°C) and the beginning of the hold at the aging temperature (200°C). The fitting strategy focused on getting the model to adequately represent the states in which the dominant strengthening precipitates are β'' (cf. Table 2.3). This corresponds to the first three data points

Table 4.1 – Yield stress model parameters and the values used in this work.

Model parameter	Symbol	Value	Unit	Source
Burgers vector magnitude	b	2.86×10^{-10}	m	[53]
Scale transition factor	M	2.24	-	[88]
Scaling factor	β	0.28	-	[8, 107, 108]
Intrinsic strength	σ_0	20	MPa	This work
Mg SSSC[1] scaling factor	k_{Mg}	342	MPa/at%$^{2/3}$	[103]
Si SSSC[1] scaling factor	k_{Si}	137	MPa/at%$^{2/3}$	[103]
Critical radius for shearing	R_{crit}	2.25	nm	This work

[1] solid solution strengthening contribution.

for which the durations of aging at 200°C were 0.1, 1 and 10 hours. Indeed, it was shown in the TEM study that the condition aged for 100 hours showed a predominance of the Q-phase hardening precipitates.

The fitting parameter here is the critical radius for shearing R_{crit} which was set at 2.25 nm to give the best possible fit. Figure 4.7a shows how, with the exception of the condition aged for 0.1 h, the model is in good agreement with the experimental values and the aging curve is adequately represented. The model predicts a significantly lower yield stress for the condition aged for 100 hours compared to the experiments. This is easily explained by the phase transformation occuring at long aging durations which switches the main hardening system from β'' to Q. The model does not contain any consideration of this phase transformation and the evolution of yield stress at longer aging durations is strictly controlled by the ripening process. Peak hardness is reached after 3 hours of aging at 200°C with a value of yield stress of approximately ∼280 MPa. After the peak, yield stress decreases to a value of ∼150 MPa after aging for 100 hours.

Yield stress follows the profile of the contribution of precipitates as they are the biggest contributors. This contribution sharply increases in two stages which are synchronized with the nucleation peaks. The less significant solid solution strengthening contribution evolves oppositely since solute atoms take part in forming the precipitates.

Figure 4.7b shows a breakdown of the contribution of precipitates into its two components (shearable and bypassed). This breakdown helps further understand the reason behind the inability of the model to fit the first experimental data point. Indeed, a very sharp peak in the contribution of shearable precipitates is observed in the first moments of the aging heat treatment. It corresponds with a large influx of small - and therefore shearable - precipitates into the system.

An alternative option is proposed which allows a perfect representation of the experimental results. It consists in considering only the contribution of the bypassed precipitates and completely dampening that of the shearable precipitates. For a value of the critical shear radius $R_{crit} = 1.6$ nm and a slightly adjusted value for $\beta = 0.26$, the evolution of the simulated yield stress is shown in Figure 4.8. In this case, the model accurately represents the aging curves fitting perfectly with

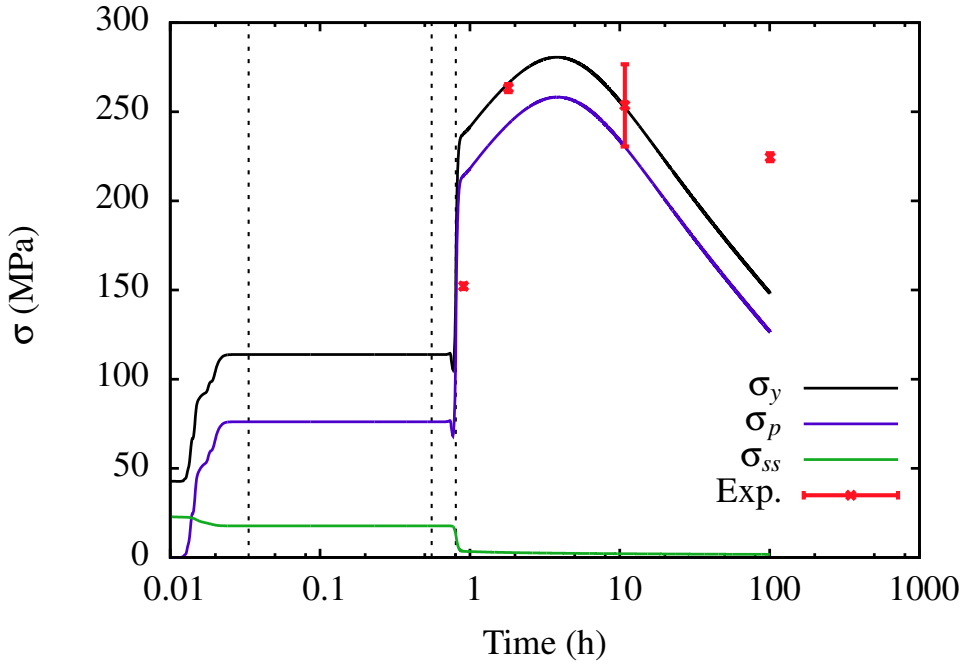

(a)

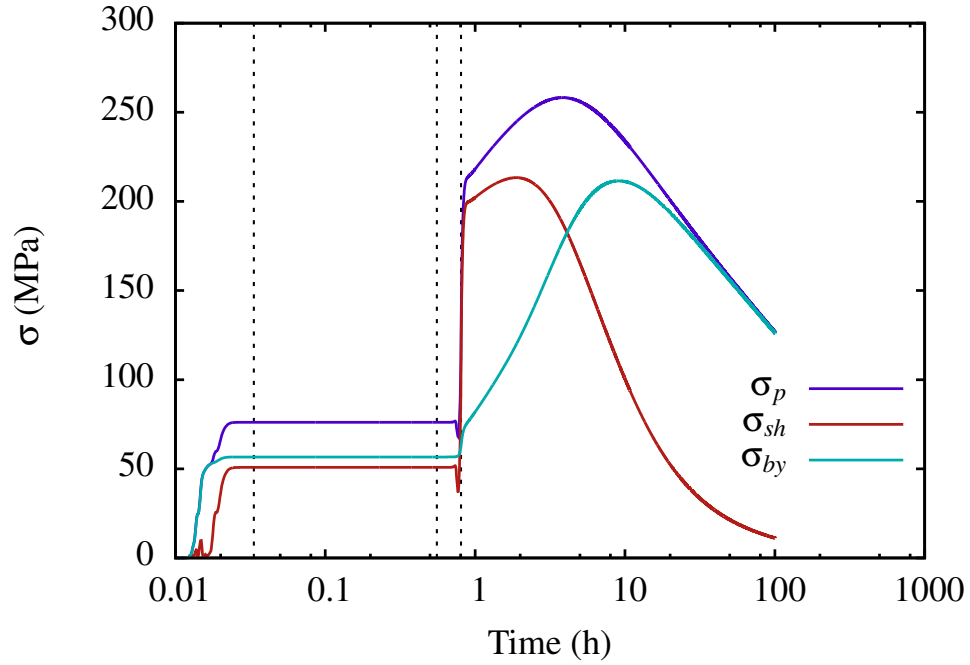

(b)

Figure 4.7 – Fitting of the simulated yield stress (σ_y) to experimental values (in red) using an R_{crit}=2.1 nm: (a) breakdown of the evolution of each contribution and (b) breakdown of the contribution of precipitates into shearable and bypassed.

the first three experimental data points. Peak hardness is reached earlier than the previous case after approximately 2.2 h of aging and its value is slightly higher ($\sim$ 290 MPa). After the peak, yield stress decreases to a value of $\sim$140 MPa after

aging for 100 h.

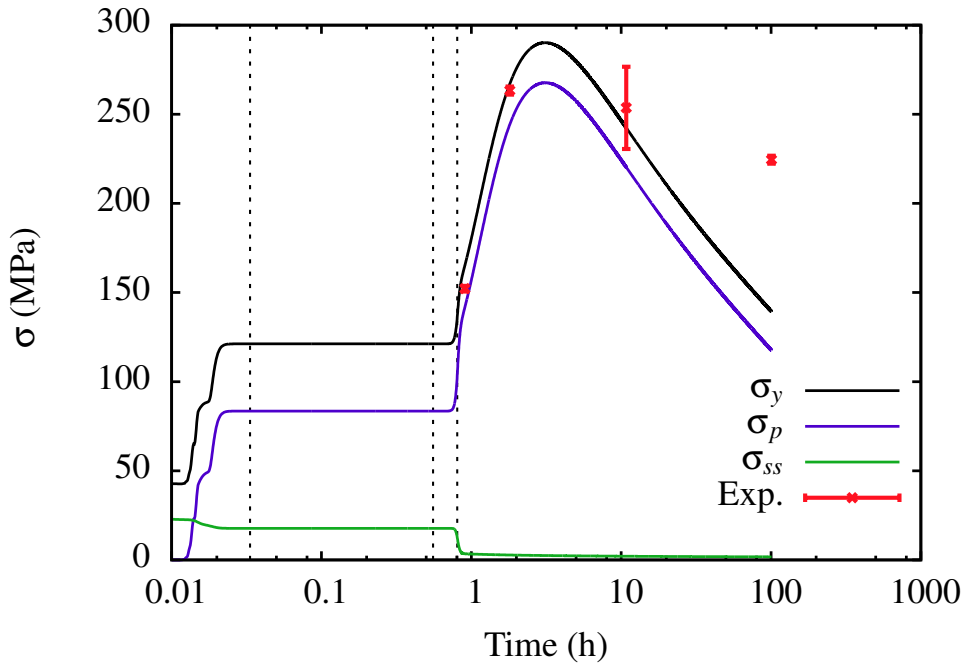

Figure 4.8 – Alternative fitting of the simulated yield stress (σ_y) to experimental values (in red) obtained by eliminating the contribution of shearable precipitates ($R_{crit} = 1.6$ nm).

4.5 Coupling to the finite element method

4.5.1 Coupling of the precipitation and yield stress models to FEM

The computation chain comprised of the precipitation and yield stress models was coupled to the finite element method. The aim is to perform calculations on parts in order to study the effect of heat treatment parameters on the yield stress gradient. As a result it will be possible to perform mechanical calculations which result in estimations of residual stresses induced by quenching and their subsequent relaxation during aging. It is assumed that the precipitation does not affect the material parameters of the thermal computation. The effect on the mechanical problem is represented by σ_y only.

Coupling was introduced in the form of a so called "local" post-processing plugin to Z-Set which was named `precipAlu`. Elements of the stand alone code are detailed in Appendix C. A local post-processing is a calculation that takes information on a given point (node or Gauss point), typically a stress and/or strain history, and delivers a result on the same point, typically an history of other variables, or a lifetime estimation (Figure 4.9). In the present case, it is to

be performed on the results of a thermal finite element calculation. A detailed presentation of the procedure is given in Appendix D.

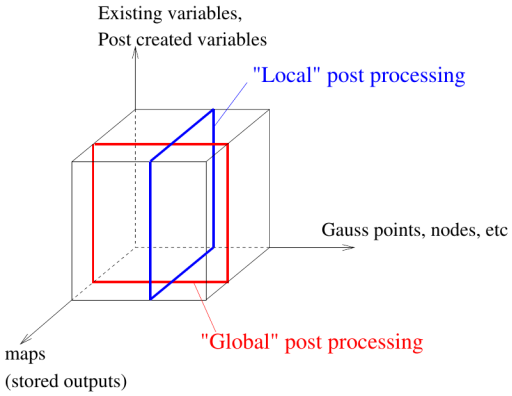

Figure 4.9 – Schematic representation of finite element post-treatments from the Z-Set manual.

Subsequent mechanical calculations are carried out in the framework of a classical unified elasto-viscoplastic model suitable for cyclic loading [109, 72]. Certain symbols hereinafter will have appeared earlier in the manuscript, aside from σ_y, the reader is invited to consider the definitions presented in the following. Under the assumption of small deformations, the strain can be decomposed into a thermoelastic component and an inelastic one $\underset{\sim}{\varepsilon} = \underset{\sim}{\varepsilon}^e + \underset{\sim}{\varepsilon}^p$. The introduction of isotropic and kinematic hardening leads to the following definition of the elastic domain (equation 4.29):

$$f(\underset{\sim}{\boldsymbol{\sigma}}, \underset{\sim}{\boldsymbol{X}}, R) = J(\underset{\sim}{\boldsymbol{\sigma}} - \underset{\sim}{\boldsymbol{X}}) - R - \sigma_y \leq 0 \tag{4.29}$$

where $\underset{\sim}{\boldsymbol{\sigma}}$ is the applied stress tensor, $\underset{\sim}{\boldsymbol{X}}$ is a non linear kinematic hardening variable, and R an isotropic hardening non-linear scalar. The second invariant J of the deviatoric effective stress, denoted by $(\underset{\sim}{\boldsymbol{\sigma}} - \underset{\sim}{\boldsymbol{X}})^d$ writes:

$$J(\underset{\sim}{\boldsymbol{\sigma}} - \underset{\sim}{\boldsymbol{X}}) = \sqrt{\frac{3}{2}(\underset{\sim}{\boldsymbol{\sigma}} - \underset{\sim}{\boldsymbol{X}})^d : (\underset{\sim}{\boldsymbol{\sigma}} - \underset{\sim}{\boldsymbol{X}})^d}. \tag{4.30}$$

The viscoplastic potential Ω of this model is defined by equation 4.31:

$$\Omega = \frac{K}{n+1}\left(\frac{f}{K}\right)^{n+1}. \tag{4.31}$$

The plastic flow rate is determined by the normality rule as follows (where $\dot{x}$ denotes the time derivative of x):

$$\dot{\underset{\sim}{\boldsymbol{\varepsilon}}}^{\boldsymbol{p}} = \frac{\partial \Omega}{\partial \underset{\sim}{\boldsymbol{\sigma}}} = \frac{\partial \Omega}{\partial f}\frac{\partial f}{\partial \underset{\sim}{\boldsymbol{\sigma}}} = \dot{p}\underset{\sim}{\boldsymbol{n}} \tag{4.32}$$

where $\dot{p}$ is the cumulated viscoplastic strain rate (equation 4.33):

$$\dot{p} = \sqrt{\frac{2}{3}\underset{\sim}{\dot{\boldsymbol{\varepsilon}}^{\boldsymbol{p}}} : \underset{\sim}{\dot{\boldsymbol{\varepsilon}}^{\boldsymbol{p}}}} = \left\langle \frac{f(\underset{\sim}{\boldsymbol{\sigma}}, \underset{\sim}{\boldsymbol{X}}, R)}{K} \right\rangle^{n} \tag{4.33}$$

and $\underset{\sim}{\boldsymbol{n}}$ defines the normality rule:

$$\underset{\sim}{\boldsymbol{n}} = \frac{3}{2} \frac{(\underset{\sim}{\boldsymbol{\sigma}} - \underset{\sim}{\boldsymbol{X}})^{d}}{J(\underset{\sim}{\boldsymbol{\sigma}} - \underset{\sim}{\boldsymbol{X}})}. \tag{4.34}$$

Two state variables are defined, $\underset{\sim}{\boldsymbol{\alpha}}$ for the kinematic hardening and q for the isotropic hardening:

$$\underset{\sim}{\dot{\boldsymbol{\alpha}}} = \underset{\sim}{\dot{\boldsymbol{\varepsilon}}^{\boldsymbol{p}}} - \frac{3D}{2C} \underset{\sim}{\boldsymbol{X}} \dot{p} \tag{4.35}$$

$$\dot{q} = (1 - bq)\, \dot{p}. \tag{4.36}$$

Hence, the hardening variables could be deduced:

$$\underset{\sim}{\boldsymbol{X}} = \frac{2}{3} C \underset{\sim}{\boldsymbol{\alpha}} \tag{4.37}$$

$$R = bQq. \tag{4.38}$$

It is customary to introduce several kinematic hardening variables in this type of model in order to allow it to precisely describe the shape of the stress-strain response of materials. For the sake of simplicity and CPU efficiency, the number of these variables here is restricted to two. In such a case, the stress-strain response of the model for pure tension writes:

$$\sigma = \sigma_y + K\left(\dot{\varepsilon}^p\right)^{\frac{1}{n}} + Q\left(1 - e^{-b\varepsilon^p}\right) + \frac{C_1}{D_1}\left(1 - e^{-D_1\varepsilon^p}\right) + \frac{C_2}{D_2}\left(1 - e^{-D_2\varepsilon^p}\right) \tag{4.39}$$

where C_i, D_i, b, K and n are parameters identified using cyclic tensile tests and are temperature dependent. The terms in the right hand side result respectively from the initial yield stress, the viscous effect, isotropic hardening, then kinematic hardening (two terms). The values used here were formerly identified on the studied aluminum alloy. Coupling to the precipitation and yield stress model concerns the yield stress parameter, σ_y.

The spatially heterogeneous temperature distribution resulting from the thermal finite element computation directly impacts the resulting yield stress maps. These maps are the output of the `precipAlu` post-processing and are used as an addition to the input material parameters file for the mechanical computation. The resulting finite element computation chain is represented in Figure 4.10 in the form of a flow-chart. The first step is a classical thermal calculation, which takes a geometric mesh, boundary conditions, material parameters, and delivers the history of the temperature fields at nodes (file `therm.node`) and Gauss points

(`therm.integ`). The second step is a post-processing of these results by means of the `precipAlu` code. The output consists in a file that contains the metallurgical variables (nucleation rate, mean radius, volume fraction and number density of precipitates), `therm.nodep` for nodes and/or `therm.integp` for Gauss points, together with the evolution of the initial yield stress. This value is used in the final step, where the mechanical calculation takes as inputs the yield stress history, the temperature history, the mechanical boundary conditions on the geometrical mesh and the material parameters of the elastoviscplastic behaviour. The final output consists in the stress and strain fields.

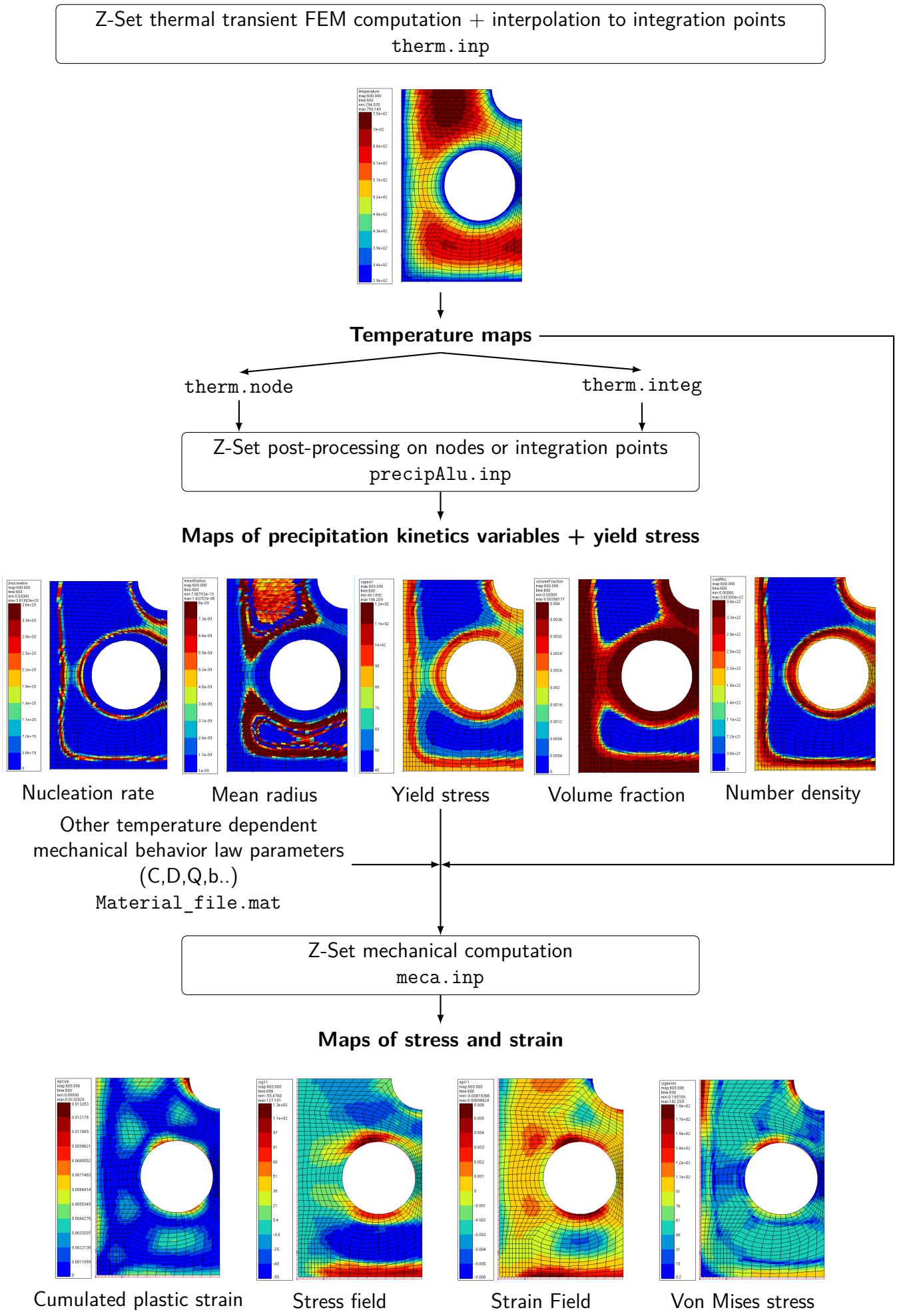

Figure 4.10 – Flow-chart describing the integrated FEM computation chain.

4.5.2 2D calculation setup

In order to demonstrate the proper functioning of the computation chain presented above, a simple 2D calculation is carried out. The geometry is a simplistic representation of a firedeck for a 4-valve cylinder of an internal combustion engine. It consists of a rectangle with five circular holes, one in the center representing the opening for the spark plug or the injector and the other four for the intake and exhaust valves. For obvious symmetry considerations, it is possible to perform this calculation on a quarter of this geometry.

The geometry is presented in Figure 4.11, together with the mesh which is made of 2D quadratic continuum elements with reduced integration (i.e. 8 nodes and 4 integration points per element).

A single boundary condition for the thermal transient calculation is applied to the nodes highlighted in yellow in Figure 4.11a. These nodes represent all the free surfaces that are in direct contact with the heat transfer fluids (water for quenching and the air circulating in the furnaces for heat treatments). This boundary condition is introduced in the form of a function depicting the heat treatment sequence that was used all throughout this work (cf. Figure 3.17). The Z-Set input file for the thermal calculation can be found in Appendix E. Note that the material parameters for the thermal behavior are simply included in the input file (under `***behavior thermal`).

Regarding the mechanical calculations, two boundary conditions were used to represent the geometrical symmetry (Figure 4.11b). Indeed displacement in the x_1 direction is set to zero for the node set on the right side (highlighted in yellow). Similarly, the displacement in the x_2 direction is set to zero for the node set on the top (highlighted in blue). No additional mechanical stresses or displacements are applied, thus depicting the effect of the heat treatment only. The mechanical computation is carried out under the assumption of plane stress. The material file used in this calculation can be found in Appendix F. All the material parameters of the constitutive equations are in this file with the exception of the initial yield stress which is given by the `precipAlu` post-processing. The Z-Set input files for the latter and the mechanical calculation can be found in Appendices G and H respectively.

In Appendix H, it can be noted that the mechanical computation reads the history of thermal and σ_y fields respectively in files `temperature.dat` and `sigmay.dat`. These files are generated by a post-processing of the thermal calculation and from the `precipAlu` results.

It is expected to have a significant difference in behavior between the core and the edges. Indeed the edges will be subject to sharp temperature gradients while at the core the gradients will naturally be more diffuse. In order to evaluate the effect of this difference, metallurgical and mechanical data will be extracted for two integration points IP 678/1 and IP 473/1 (this notation stands for the element number and the Gauss point rank in the element). Figure 4.12 shows the positions of these integration points, IP 678/1 being in the edge and IP 473/1 in the core.

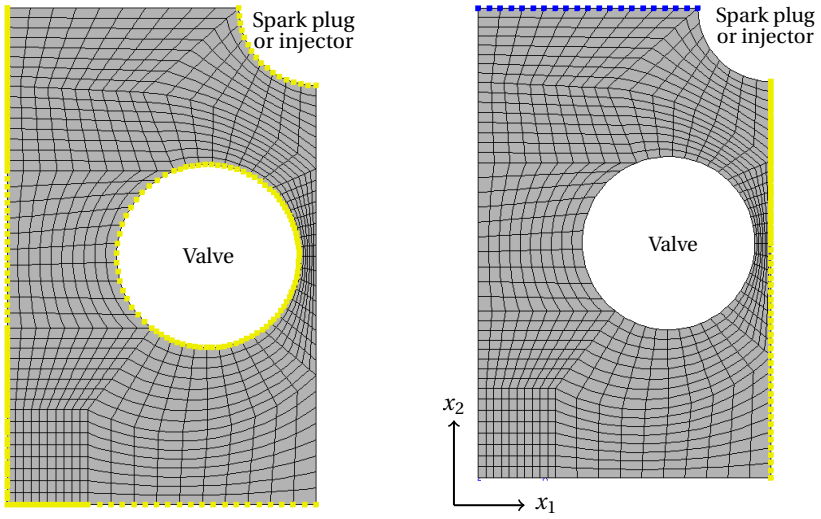

Figure 4.11 – Node sets on which boundary conditions are applied (a) in the thermal transient calculation and ,(b) in the mechanical calculation.

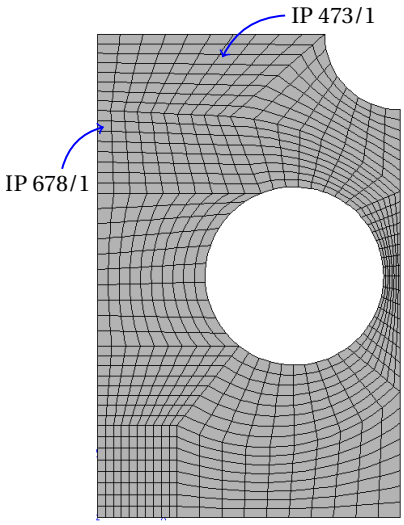

Figure 4.12 – Positions of integration points IP 678/1 and IP 473/1 for which output is analyzed.

4.5.3 Analysis of the `precipAlu` post-processing results

Maps of the interesting variables were extracted for three key moments in the thermal sequence: right at the end of the quench, in the beginning of the aging heat treatment plateau and after 2 hours of aging. Figure 4.13a shows the temperature distribution right after quenching. While the boundaries are cooled down to room temperature, it can be observed that temperatures are still high in core areas (around 480°C). The opposite is observed in Figure 4.13b right after the heating ramp. The boundaries reach the aging temperature of 200°C while the core is

lagging behind at around 80°C . Finally, the temperature hold at 200°C for 2 hours homogenizes temperature over the entire structure as is shown by Figure 4.13c.

In terms of the nucleation rate, right after quenching Figure 4.13d shows strings of nucleation events in areas where thermal conditions are optimal, i.e. below solvus of the precipitating phase and high enough for atomic mobility: the nucleation rate peaks for temperatures between 450°C and 120°C . This zone forms a ribbon which progresses inwardly from the edge to the core with the evolution of the temperature. Along this ribbon, the order of magnitude of the nucleation rate is 10^{20}. In the start of the aging heat treatment, nucleation is again activated as shown in Figure 4.13e. This reactivation is visible around the edges which are at a temperature of 200°C and the order of magnitude is the same as right after quenching (10^{20}). Once again, this reactivation progresses inwardly, reaching the core with considerable latency. Finally, after enough time at the aging temperature and as the oversaturation approaches zero, no more nucleation events are possible with the exception of some areas where thermal latency was at a maximum. However, the order of magnitude at this point is significantly lower (10^{5}). In accordance with the stand alone simulations shown in chapter 3, nucleation occurs in two peaks, one during quenching and the other during heating for the aging heat treatment.

The nucleation events directly impact the mean radius as can be observed in the global decreasing progression given by Figures 4.13g, 4.13h and 4.13i. Indeed, with each nucleation event, the mean radius decreases. Although growth also factors into the evolution of the mean radius, the large changes are mainly due to influxes of nuclei of small size into the system. Figure 4.13i clearly shows the contrast between areas where sharp temperature transients occured and others where transients were smoother. The resulting mean radii in the former are significantly smaller than those for the latter. In the edges, this is in agreement with the simulation result presented in Figure 3.19 of chapter 3, where the mean radius remains below 2 nm for low aging durations. At the core, the low temperature gradient significantly increases the mean radius where it reaches values around 7 nm.

Recall that the equilibrium volume fraction of the precipitating phase predicted by Thermo-Calc/TCAL5 at 200°C is around 0.88%. As shown in Figure 4.13l, this equilibrium value is reached after 2 hours of aging at 200°C . The evolution of the volume fraction occurs in two stages, one at the end of the quench and the other during the heating ramp for the aging heat treatment. Figure 4.13j shows that right after quenching, the areas close to the edges reach almost 50% of the equilibrium volume fraction. At the start of the aging heat treatment plateau, a sharp increase in the volume fraction is observed at the core (Figure 4.13k). It can be stated that this increase is mainly controlled by growth since no nucleation events occur in those areas as mentioned previously.

Regarding the total number density of precipitates, Figures 4.13m, 4.13n and 4.13o clearly show that areas with sharp temperature gradients contain a far greater number of precipitates that the areas with diffuse temperature gradients. This observation is fully consistent with the aforementioned observations related to the mean radius and volume fraction. Indeed, at the equilibrium volume

fraction, the edges are characterized by large number densities of very small precipitates. The orders of magnitude, starting from zero and then ranking from 10^{22} to 10^{23} after the two-hour plateau, is in agreement with the evolution reported in Figure 3.18 for the stand alone calculation. Contrarily, the core is characterized by smaller number densities of coarser precipitates.

It is therefore expected that the yield stress would be higher in the edges than it is at the core. This is exactly what is depicted by Figures 4.13p, 4.13q and 4.13r. The initial yield stress without precipitates is very low, as verified by the large area at 40 MPa at the end of quenching (Figure 4.13p). It increases rapidly, as demonstrated by the external boundaries on the same figure where it already reaches 100 MPa. Since the number of precipitates is still increasing, the initial yield continues to increase, and reaches 150 MPa at the beginning of aging (Figure 4.13q). The hardening effect of the aging period can be checked in Figure 4.13r, that shows "hard zones" at 250 MPa not far from the surface of the component. Meanwhile, the core remains relatively soft, with values still in the vicinity of 100 MPa.

The coherence of this finite element model is further accentuated by Figure 4.14, where these variables are plotted with respect to time for the two integration points IP 678/1 (near surface point) and IP 473/1 (core). Figure 4.14a shows the difference in thermal history seen by these two integration points. Indeed, IP 678/1 is subject to sharp thermal gradients while IP 473/1 is significantly more diffuse.

The impact of this on the nucleation rate is displayed in Figure 4.14b. The nucleation rates are significantly bigger, narrower and occur sooner at IP 678/1 compared to IP 473/1. This suggests that in the bulk, IP 473/1 evolves in a manner that is more near-equilibrium than IP 678/1 which is a near-surface point. This directly affects the mean radius and total number density in the previously discussed manner. Figures 4.14c and 4.14d show how IP 678/1 ends up with a high number density of small precipitates in contrast with IP 473/1. The equilibrium volume fraction is also reached a lot sooner at IP 678/1 than it is the case for IP 473/1 as per Figure 4.14e. This precociousness quickly transits IP 678/1 into the ripening regime where the total number density decreases. The aforementioned two stages of evolution of the volume fraction can also clearly be observed. The resulting yield stress is therefore considerably higher at the near-surface point IP 678/1 than in the core at IP 473/1. The onset of ripening at IP 678/1 decreases the yield stress.

4.5.4 Analysis of the mechanical calculation results

The mechanical calculation results are presented in Figure 4.15 in the same manner as for the post-processing results. The temperature fields are first reproduced (Figures 4.15a,4.15b and 4.15c) for the sake of comparison with the other fields contours.

Figures 4.15d, 4.15e and 4.15f show maps of the σ_{11} stress tensor component.

Along the vertical A-A line displayed on these figures, a case of self-balancing stresses can be observed. As a result of cooling, the middle of this line is under compressive stress (about -55 MPa) and its extremities are under tensile stress (about 110 MPa). These stresses then invert as a result of heating. The middle switches to a tensile stress of about 150 MPa while the extremities have a compressive stress of about -170 MPa. This stress distribution remains the same after aging for 2 hours at 200°C but decreases in magnitude considerably (from 150 to 80 MPa in the areas in tension and from -170 to -90 MPa in the areas in compression).

Figures 4.15g, 4.15h and 4.15i show maps of the ε_{11}^{p} deformation tensor component. As a result of cooling, plastic deformation is generated in accordance with the previously discussed distribution. The bulk of plastic deformation is produced at this stage with values ranging from -0.61% to 0.69%. Heating also produces plastic deformation within a considerably smaller range (-0.2% to -0.16%) which remains constant for the remaining aging time at 200°C . This point to plasticity no longer becoming possible as a result of the material gaining in hardness thanks to precipitation and, to a lesser extent, work hardening. The thermal transients are therefore responsible for generating stress and the subsequent aging heat treatment relaxes these stresses. The residual stresses in the x_1 direction are greater in regions close to the right boundary which is blocked in this direction.

The σ_{22} and ε_{22}^{p} components are presented in Figures 4.15j, 4.15k and 4.15l and Figures 4.15m, 4.15n and 4.15o respectively. Similar observations as before can be made in the x_2 direction. The stresses are self-balancing along the horizontal B-B line displayed on the figures. Cooling generates compressive stresses (about -65 MPa) in the middle and tensile stresses (about 180 MPa) at the extremities, which ends up inverting as a result of heating (-220 MPa and 160 MPa). After aging for 2 hours at 200°C , stress decreases in the most compression loaded areas to -140 MPa and to 87 MPa the most tension loaded areas. Plastic deformation follows the same trend observed for the x_1 component, i.e. peaking after quenching and remaining invariable during aging. Here, the residual stresses in the x_2 direction are greater in regions close to the upper boundary which is blocked in this direction.

The von Mises stress, σ_{mises}, is presented in Figures 4.15p, 4.15q and 4.15r. Throughout its evolution it can be seen that overall, it increases as a result of the thermal transients during quenching and heating. As a result of the isothermal aging, the von Mises stress decreases significantly as relaxation takes place.

Further analysis is carried out by examining the response at the integration points IP 678/1 and IP 473/1. Firstly, Figure 4.16a shows that the plastic strain is cumulated over two stages corresponding to the two thermal transients. The cumulated plastic strain stabilizes as the aging heat treatment plateau is reached. Its magnitude is considerably higher at IP 678/1 in comparison to IP 473/1. This is due to the sharpness of the thermal transients seen by IP 678/1 being at the edge of the structure.

Figure 4.16b shows σ_{22} with respect to σ_{11}. On the one hand, it can be observed that IP 678/1 is clearly under uni-axial stress in the x_2 direction ranging

from -175 MPa to just under 150 MPa. On the other hand, IP 473/1 is under biaxial stress, dominated by the x_2 component ranging from -60 to 150 MPa versus -25 to 25 MPa for the x_1 component. At the end of the heat treatment, IP 473/1 retains σ_{11} and σ_{22} stresses of around 12 and 90 MPa respectively.

Figures 4.16c and 4.16d, presents the stress-plastic strain response at these two integration points. The antithetical behavior of the edge and core can be observed whereby tensile stresses at IP 678/1 are met with compressive stresses at IP 473/1 in both directions and vice versa. It is worth pointing out how yield occurs at significantly lower stress values during the quench in comparison to during the heating. For example, at IP 678/1 which hardens the most, the first yield point during the quench occurs at around 45 MPa which essentially amounts to the intrinsic matrix strength and solide solution strengthening. However, the second yield point occurs at around 125 MPa since the material benefits from the hardening effect of precipitation at this stage. At the end of the heat treatment, IP 678/1 retains σ_{22} stresses of around 40 MPa.

Finally, Figures 4.16e and Figures 4.16f allow the tracking of the von Mises stress along with yield stress. It can be observed that relaxation occurs around the time the aging heat treatment plateau is reached in both integration points. As hardening occurs faster and more significantly in IP 678/1, relaxation occurs earlier as the von Mises stress dips below yield stress. The opposite is seen in IP 473/1 where the von Mises stress remains above yield stress for a longer duration. The residual stress, in the von Mises sense, after heat treating for 2 hours is therefore significantly higher at IP 473/1 (around 80 MPa) in comparison with IP 678/1 (around 25 MPa).

4.6 Conclusion

The evolution of yield stress was modelled as the summation of the contributions of intrinsic strength, solid solution strengthening and precipitation hardening. The equations estimating these contributions all involve output variables of the precipitation model thus offering a microstructure-informed estimation. The contribution of precipitates was modelled such that their morphology and orientation in the matrix are taken into account. This model also splits the precipitates into two separate contributions of shearable and bypassed precipitates.

The results of the yield stress model were then confronted to the tensile test results presented in chapter 2. A sufficiently adequate fit to the experiments was achieved using a critical radius for shearing of R_{crit}= 2.25 nm. Another option consisting in eliminating the contribution of shearable precipitates allowed a perfect fit with the experiments with a value of R_{crit}= 1.6 nm.

The yield stress model breaks down for long aging durations and predicts considerably lower values than the experiments. This is due to the phase transformation occuring at long thermal exposure durations which transition the microstructure from being β-dominated to Q-dominated.

Coupling to the FEM was achieved by means of a post-processing which was

named `precipAlu`. This post-processing program takes as input thermal maps and produces maps of precipitation kinetics variables and yield stress. The latter were used as an input material behavior law parameter directly informed by the temperature and time dependent microstructural evolution in the part.

A 2D demonstrator was setup and an example calculation was carried out. The analysis of the results of this calculation show coherent results in terms of all the output variables. This newly established computation chain allowed the evaluation of the yield stress gradient occuring as a result of a heat treatment sequence. Just as important, the residual stress created during quenching and their subsequent relaxation can also be evaluated.

This offers a powerful tool for the optimization of heat treatments and geometries in industrial contexts. Of course, further fine tuning in terms of the time and size-space discretization would be necessary to improve the results of such calculations.

End of quench | Beginning of aging | After 2h plateau

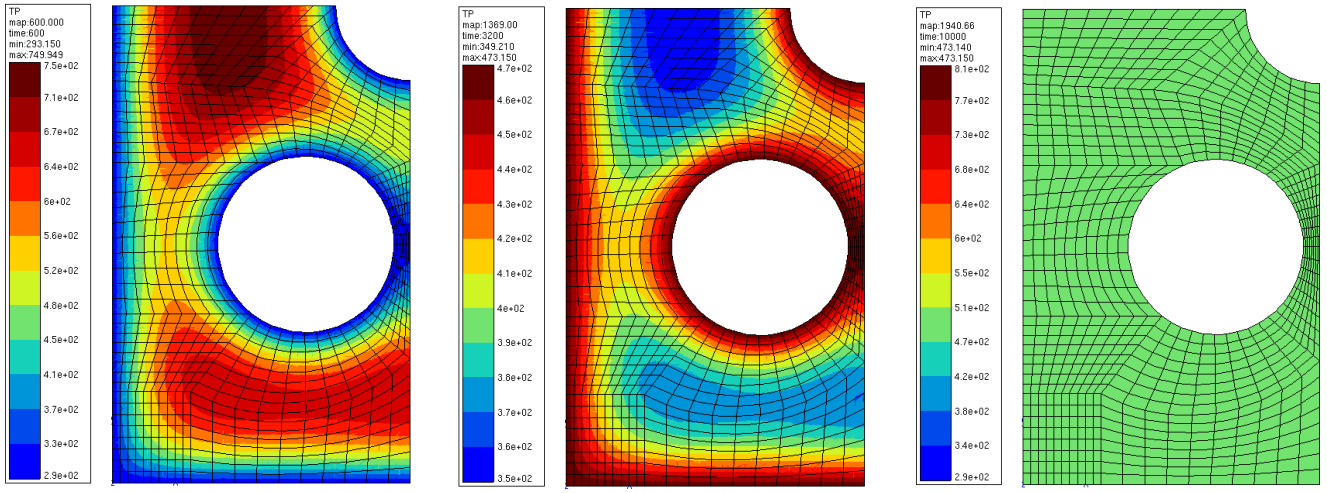

(a) (b) (c)

Temperature

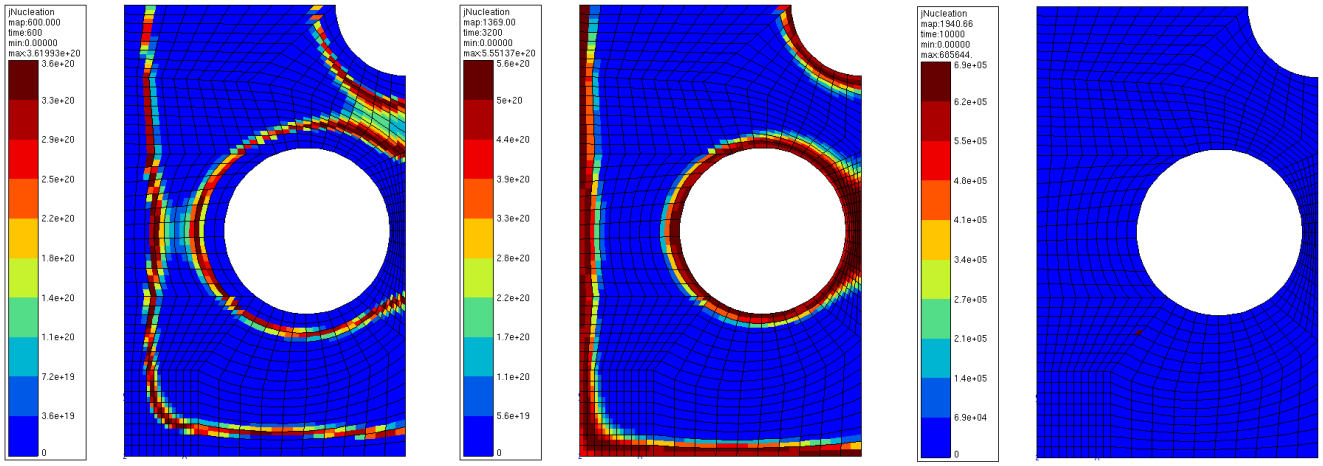

(d) (e) (f)

Nucleation rate

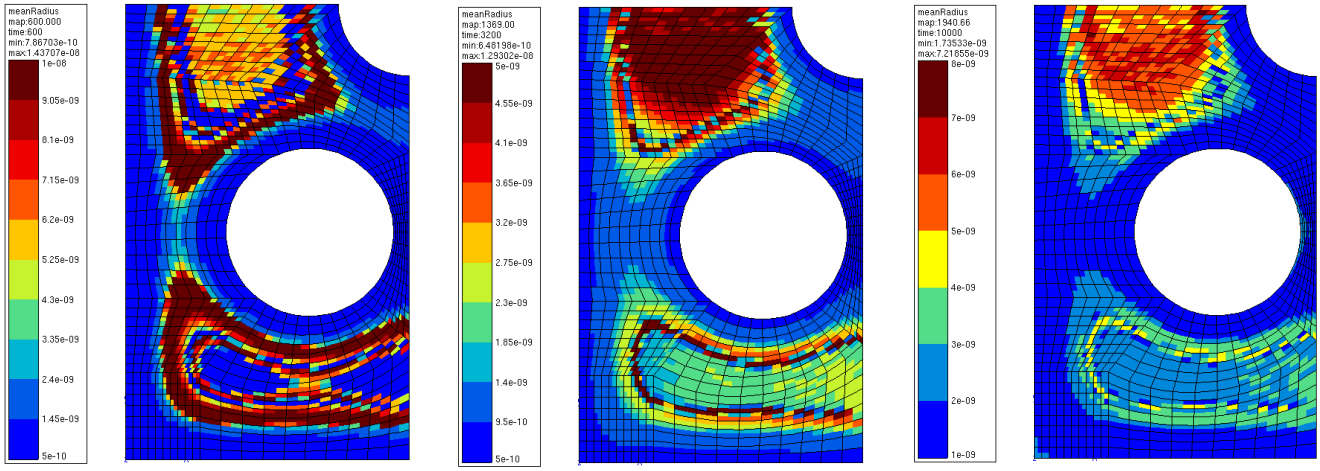

(g) (h) (i)

Mean radius

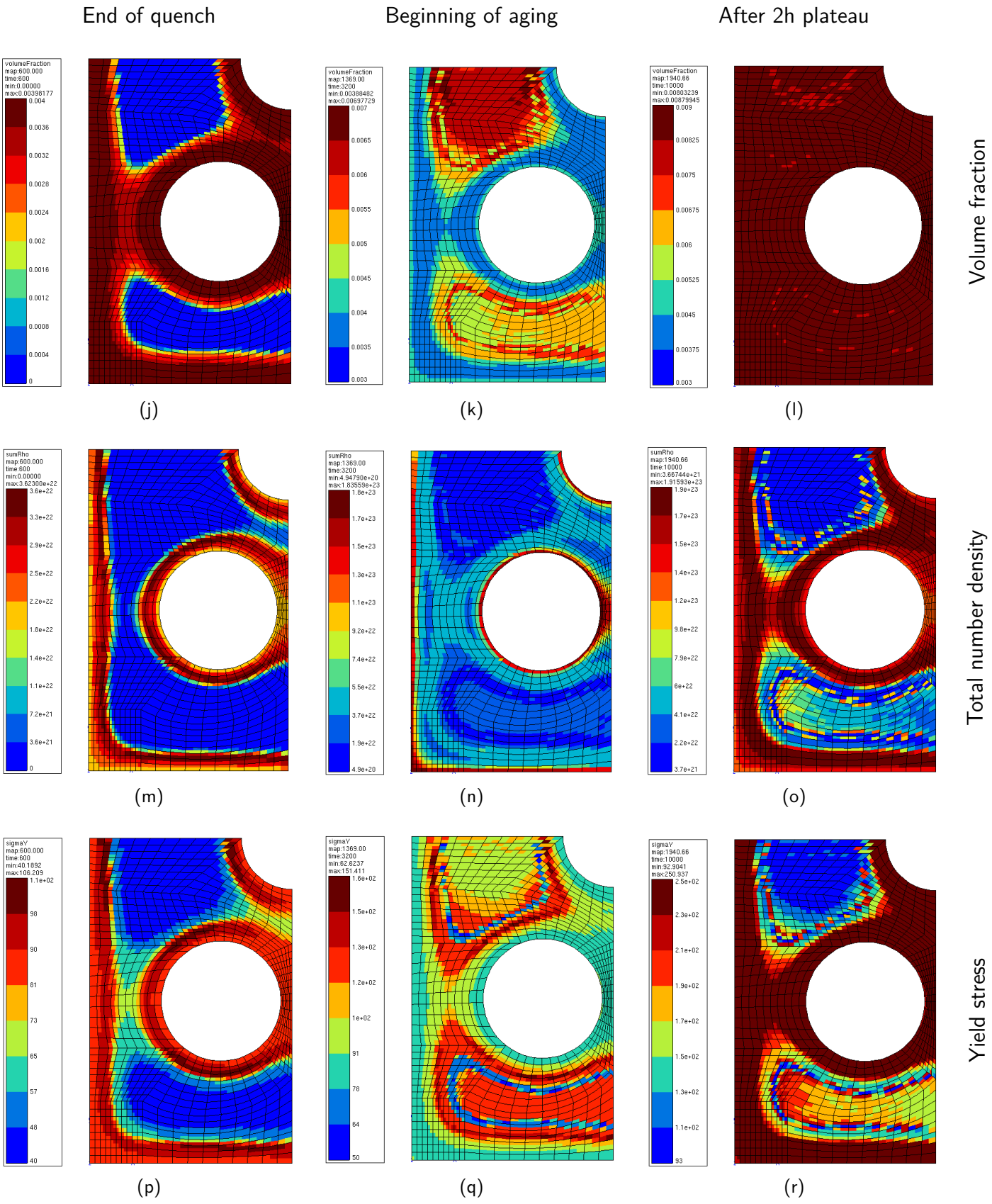

Figure 4.13 – Maps of temperature and the output variables of interest for the `precipAlu` post-processing. Columns from left to right correspond to the end of the quench, beginning of the aging heat treatment plateau and following 2 hours of aging respectively. Rows 1 through 6 correspond to temperature, nucleation rate, mean radius, volume fraction, total number density and yield stress respectively.

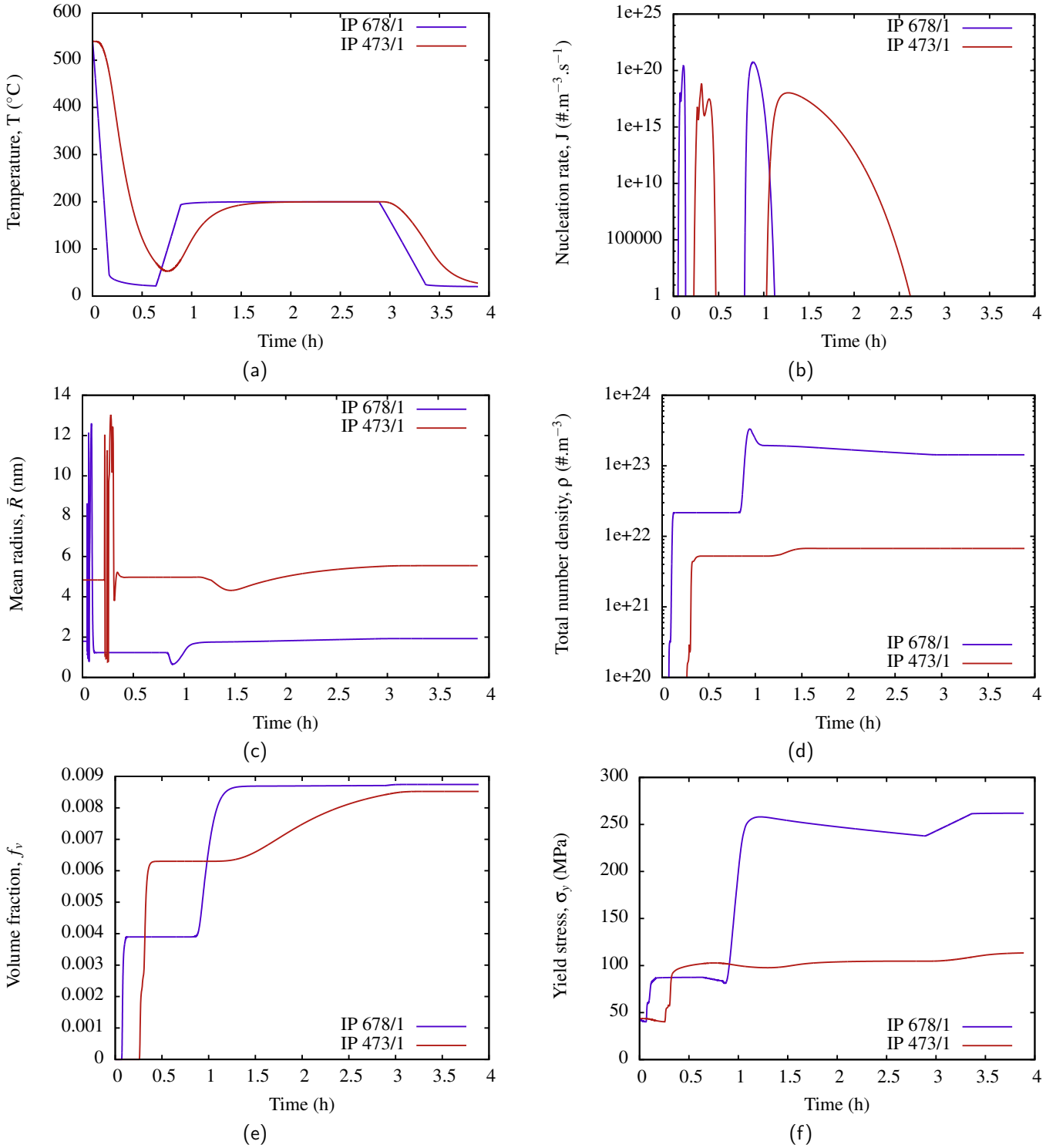

Figure 4.14 – Behavior comparison between IP 678/1 and IP 473/1 through time in terms of (a) temperature ,(b) nucleation rate (c) mean radius, (d) total number density, (e) volume fraction and (f) yield stress.

End of quench | Beginning of aging | After 2h plateau

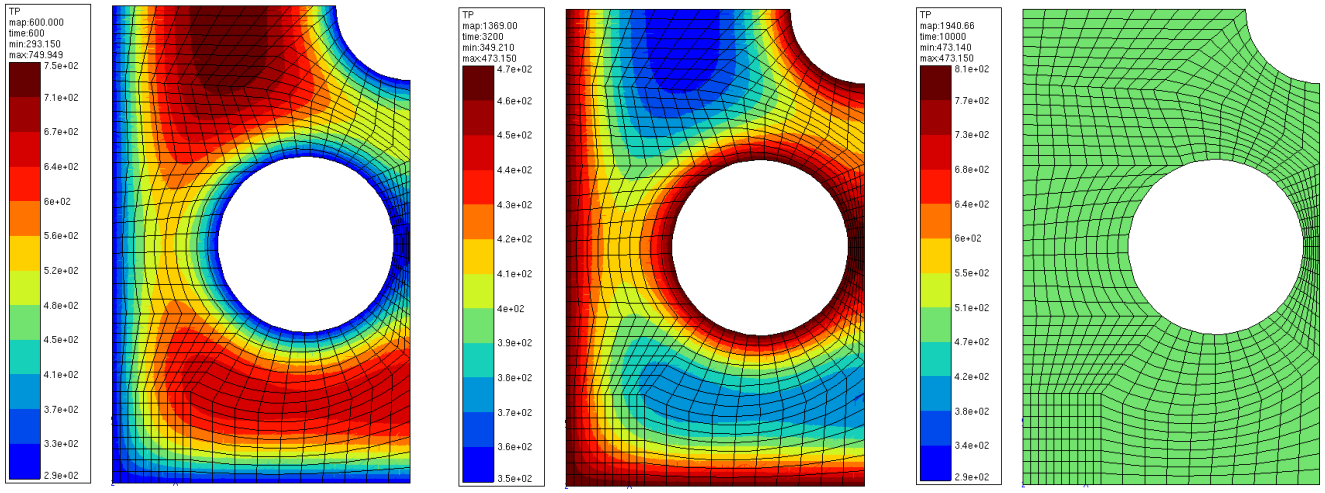

(a) (b) (c)

Temperature

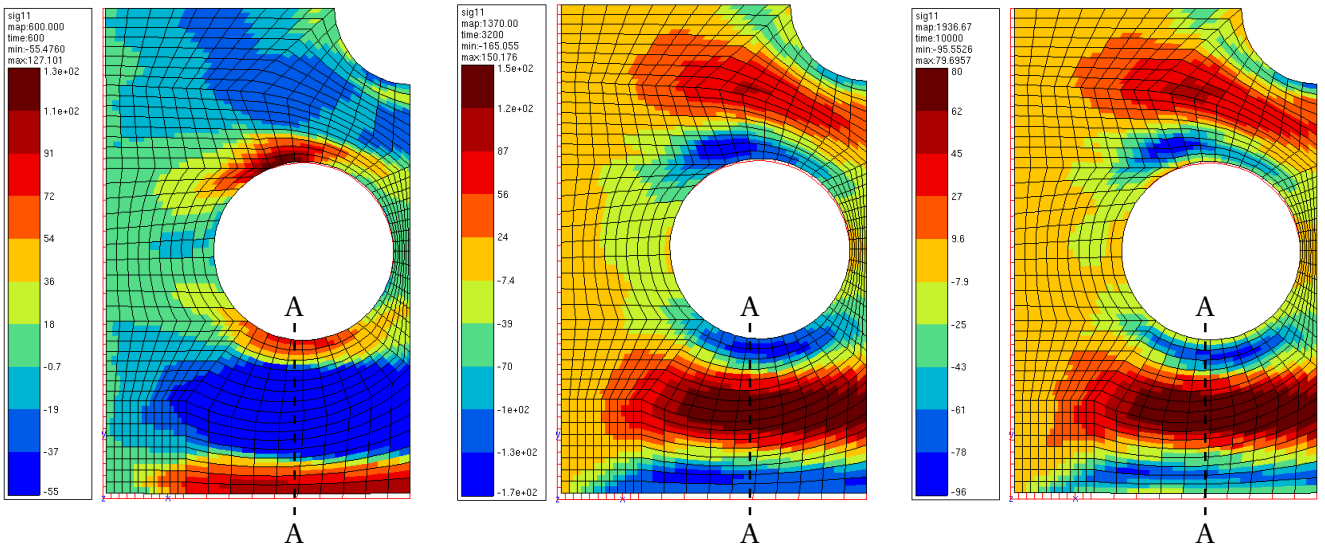

(d) (e) (f)

σ_{11}

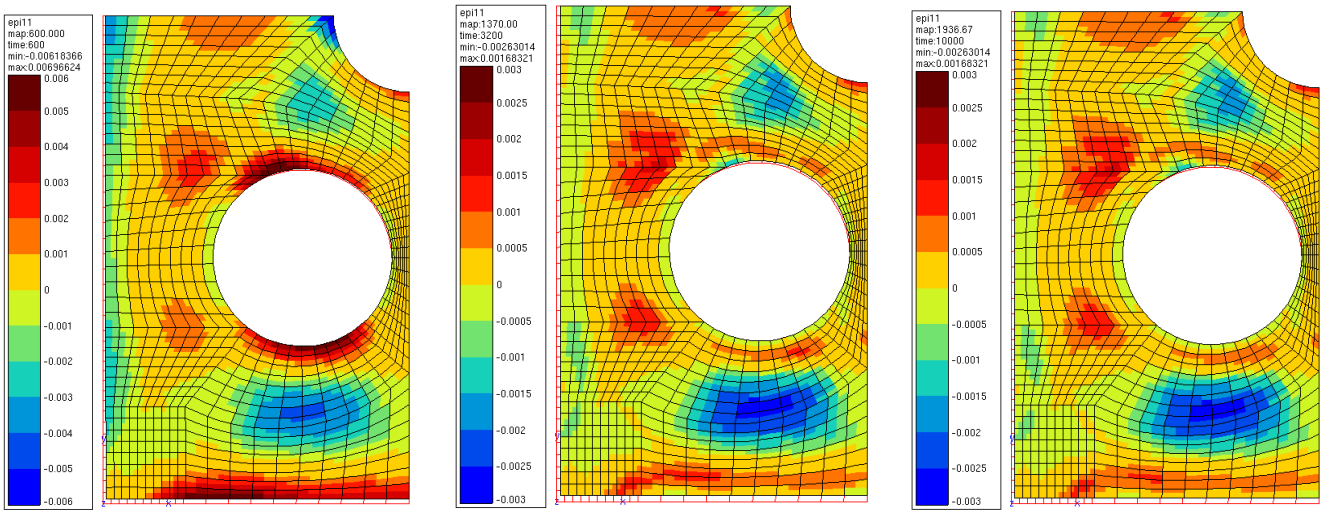

(g) (h) (i)

ε_{11}^{p}

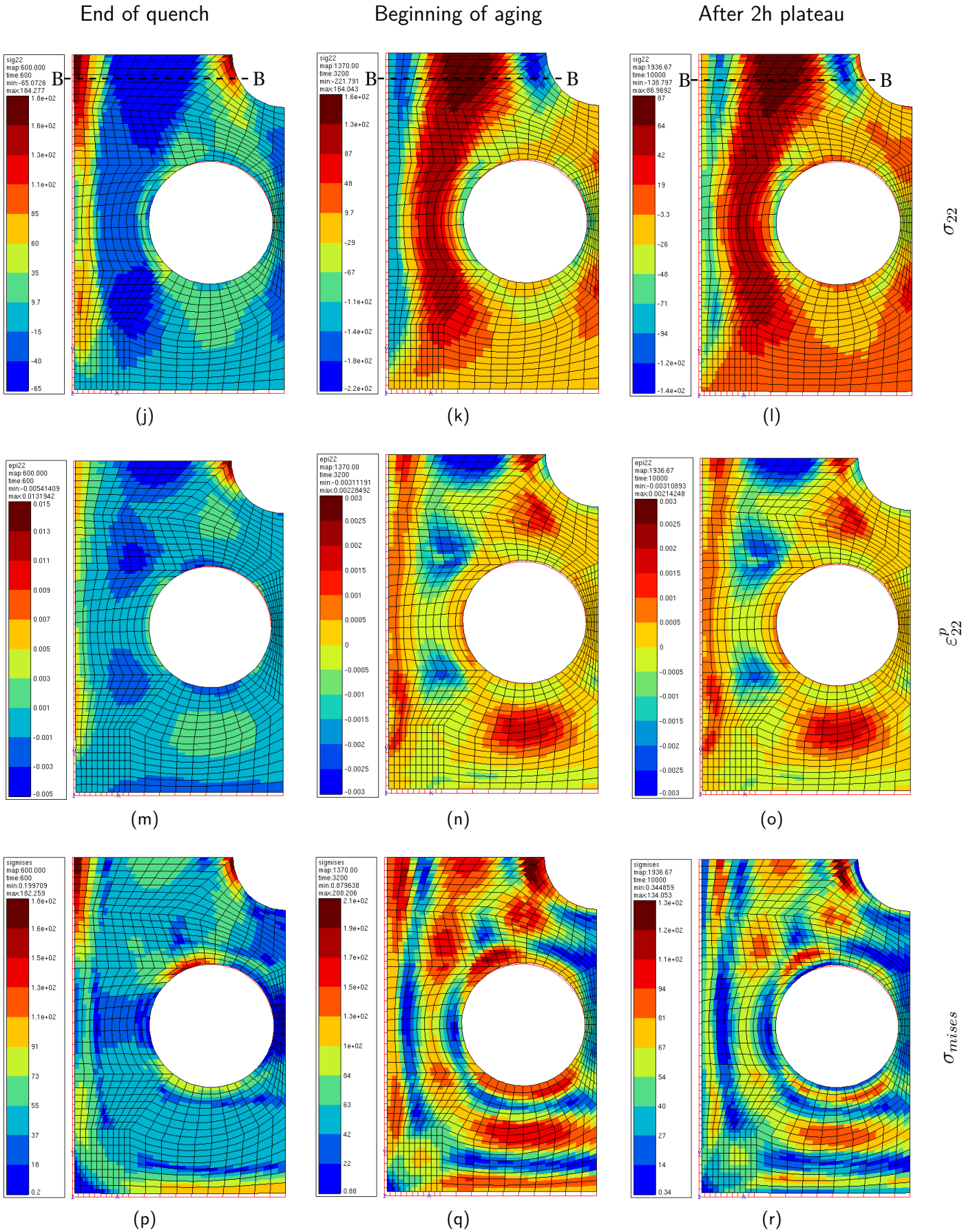

Figure 4.15 – Maps of temperature and the output variables of interest for the mechanical calculation. Columns from left to right correspond to the end of the quench, beginning of the aging heat treatment plateau and following 2 hours of aging respectively. Rows 1 through 6 correspond to temperature, σ_{11}, ε_{11}, σ_{22}, ε_{22} and σ_{mises}.

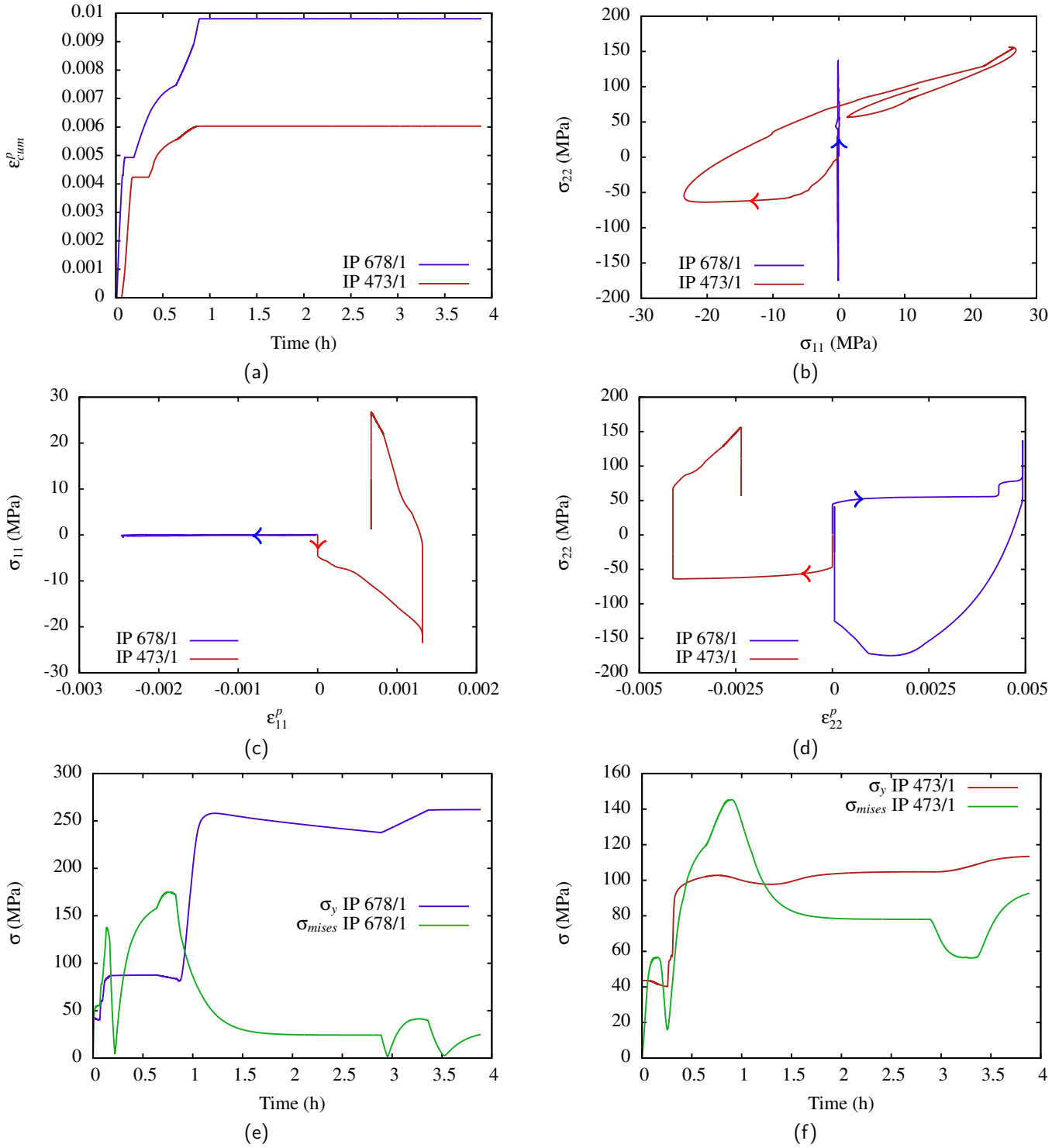

Figure 4.16 – Behavior comparison between IP 678/1 and IP 473/1: (a) cumulated plastic strain with respect to time, (b) σ_{22} with respect to σ_{11} (c) stress-plastic strain response in the x_1 direction, (d) stress-plastic strain response in the x_2 direction, (e) von Mises and yield stress with respect to time for IP 678/1 (f) mises and yield stress with respect to time for IP 473/1.

Conclusion and perspectives

This work was centered around modelling precipitation hardening in an A356+0.5Cu cast aluminum alloy for cylinder head applications. The low-alloyed nature of this alloy allows it to have an optimal thermal conductivity compared to its high-alloyed counterparts. This alloy benefits from adequate mechanical properties resulting from heat treatments of solutionizing, quenching and aging. These heat treatment activate the precipitation of the β-Mg_2Si hardening phase system, thus considerably raising the yield stress of the alloy.

The behavior of the studied A356+0.5Cu alloy when subject to a heat treatment sequence was studied. Indeed, samples were solutionized, quenched and aged at 200°C for 0.1, 1, 10 and 100 hours. Then, a TEM characterization was conducted on these samples with qualitative and quantitative aims. It was shown that for the short aging durations (up to 10 hours), the dominating hardening precipitates were β'' rods, while for the long aging duration (100 hours), the dominance shifted to the Q-phase system (Q′, Q″ precipitates). The length and diameter of the β'' rods were measured on a sufficiently high number of precipitates to produce size distributions. These size distributions later served for the calibration and validation of the precipitation kinetics model. In addition to that, tensile tests were carried out for these aging conditions in order to evaluate the evolution of yield stress as a function of the duration of the aging heat treatment at 200°C. Thus, the aging curve was produced which in its turn served for the calibration and validation of the yield stress model.

The aim of the modelling effort was therefore to reproduce the experimental results both in terms of size distributions and yield stress by simulating the heat treatment sequence. A physics-based precipitation kinetics model was used which relied on classical nucleation theory equations and Fick's laws of diffusion. Indirect coupling to the Thermo-Calc software was used to feed the model essential thermodynamic variables such as the driving force for precipitation and the solubility product. These variables are extracted for a wide range of compositions and temperature and then numerically fitted. Then, the model accesses their values by simply evaluating these numerical functions thus reducing computation time. Recent developments regarding the correction of the growth rate equations and the curvature effect to take into account the elongated morphology of precipitates were also implemented [81]. The KWN size class approach was used to track the evolution of the size distributions. This approach combined with a Euler implicit finite differences scheme linearizes the integration problem and reduces it to the

inversion of a tri-diagonal matrix which can be efficiently achieved thanks to an upper-lower type algorithm. The implementation of a Newton-Raphson solver algorithm was also made necessary by the multi-constituent nature of the precipitating phase.

The precipitation model was then confronted to the measured size distributions for calibration and validation. As it is practiced for this type of approaches, the matrix/precipitate interfacial energy was used as a fitting parameter. In this work two separate values were used for the nucleation equations and growth equations. For reasonable values of these parameters the model was capable of reproducing the experimental size distributions with good accuracy.

The yield stress was modelled as the pythagorean sum of the contributions of intrinsic strength, solid solution strengthening and precipitation hardening. The major contribution there being precipitation hardening, it was modelled using an approach originally proposed by Deschamps *et al.* [110]. Further developments introduced by Esmaeili *et al.* [11] and Bardel *et al.* [8] which address the morphology and orientation of these precipitates in the matrix were implemented. The results of the yield stress model were also confronted to experiments using the critical radius for shearing as a fitting parameter. Again, with reasonable values of this parameter, a good agreement with the experiments was obtained. However, a large underestimation of yield stress was obtained for a long aging duration at 200°C (100 hours). This is explained by the phase transformation observed in the microstructural analysis after long aging. Indeed, the transition to the Q-phase hardening system allows the alloy to maintain a higher level of yield stress for a significantly longer aging time. This is the result of the presence of Cu in the composition which allows this phase transformation and increases the aging resistance of the alloy.

Overall, this hybrid physics-based and phenomenological approach presents a good step in the direction of the integrated computational materials engineering. However, many assumptions are made all throughout in the adopted modelling scheme. They are accomodated by the use of fitting parameters, the values of which are detached from physical considerations. Finally, the physical underpinning of many aspects of this modelling effort offers a good scope of application, especially when compared to purely phenomenological approaches [111, 112, 113]. Indeed, thanks to this model, the effect of heat treatment parameters can be studied, the ability to handle anisothermal states being at the core of the capabilities of this approach. It is also possible to study, to a certain extent, the effect of changes in the chemistry of the alloy. This is however limited by the necessity for the chemistry change to have no impact on the nature of the hardening precipitates.

This leads to the statement of the most important perspective of this work, which is the generalization to a multi-phase model. This should especially address the case where the precipitation of different phases is inter-dependent, such is the case for alloys of type A356+0.5Cu. The KWN approach is intrinsically capable of handling multiple distributions of precipitates, but the thermodynamic description

of these phases and the transition from one to the other requires further work. Aside from remedying to the aforementioned discrepancy of the model and experiments for long aging durations, this would open the door for studying the effect of chemical composition, thus enabling tailor-made alloy development.

Another major perspective of this work consists in extending the effect of microstructure dependence to the material parameters that represent isotropic and kinematic hardening. In the present state, only initial yield stress is informed by the microstructural state while the hardening variables are experimentally identified. These variables are therefore dependent only on temperature and are identified for alloys in a given heat treated state. This limits the capability of the model in terms of representing the evolution of the plastic domain.

More immediate perspectives include the introduction of an evolution law for the aspect ratio, considered constant in this work, compatible with isothermal treatments. The nucleation stage also merits more consideration of elastic strain energy and heterogeneous nucleation.

From a more fundamental point of view, the experimental or computational determination of the matrix/precipitate interfacial energies would solve a major drawback of these approaches. Also, the scale transition from dislocation/obstacle interactions to macroscopic estimations of yield stress requires significant work.

Finally, the ultimate goal of this work was the construction of a finite elements method computation chain integrating the precipitation kinetics and yield stress model. This has been achieved by means of the creation of a postprocessing option called "`precipAlu`". The process takes as its input the result of a FEM thermal calculation and produces maps of the precipitation kinetics variables and of the initial yield stress. The initial yield stress map is joined to the temperature map to be the input of the mechanical calculation. A 2D demonstrator has been set up and was used to show the capability of the computation chain to track the property gradients produced by the heterogeneous temperature distribution in the structure. It was also shown that the FEM model properly represents the evolution of internal stresses induced by quenching and relaxed by aging. This allows the estimation and localization of the residual stresses which can be used to optimize heat treatments and geometries. Further fine tuning is required in order to transition to 3D calculations and experimental verification of the capability of the model to predict the levels and localization of residual stresses is of course necessary.

Bibliography

[1] European Union. Climate action section of the official website of the european union.

[2] Mustafa Kemal Kulekci. Magnesium and its alloys applications in automotive industry. *The International Journal of Advanced Manufacturing Technology*, 39(9-10):851–865, 2008.

[3] Neda Sarmady. The effect of quench rate and initial grain structure on the mechanical behaviour of an al-mg-si-mn aluminum alloy. Master's thesis, University of British Columbia, 2018.

[4] Anatomy Note. Car engine anatomical structure - https://www.anatomynote.com/transportation-anatomy/machinery-parts/car-engine-anatomical-structure/.

[5] Eric Nicouleau-Bourles. *Etude experimentale et numerique du vieillissement d'un alliage d'aluminium. Application aux culasses automobiles*. PhD thesis, École Nationale Supérieure des Mines de Paris, 1999.

[6] Bruno Barlas. *Etude du comportement et de l'endommagement en fatigue d'alliages d'aluminium de fonderie*. PhD thesis, École Nationale Supérieure des Mines de Paris, 2004.

[7] Rémi Martinez. *Modélisation multi-échelles des propriétés mécaniques d'un alliage d'aluminium de fonderie*. PhD thesis, Paris Est, 2012.

[8] D. Bardel, M. Perez, D. Nelias, A. Deschamps, C.R. Hutchinson, D. Maisonnette, T. Chaise, Josselin Garnier, and F. Bourlier. Coupled precipitation and yield strength modelling for non-isothermal treatments of a 6061 aluminium alloy. *Acta Materialia*, 62:129–140, 2014.

[9] Yue Li, Bjørn Holmedal, Hongxiang Li, Linzhong Zhuang, Jishan Zhang, and Qiang Du. Precipitation and strengthening modeling for disk-shaped particles in aluminum alloys: Size distribution considered. *Materialia*, 4:431–443, 2018.

[10] Rui Chen, Qingyan Xu, Huiting Guo, Zhiyuan Xia, Qinfang Wu, and Baicheng Liu. Modeling the precipitation kinetics and tensile properties

in Al-7Si-Mg cast aluminum alloys. *Materials Science and Engineering: A*, 685:403–416, 2017.

[11] Shahrzad Esmaeili. *Precipitation hardening behaviour of AA6111*. PhD thesis, University of British Columbia, 2002.

[12] John Allison, Dan Backman, and Leo Christodoulou. Integrated computational materials engineering: a new paradigm for the global materials profession. *Jom*, 58(11):25–27, 2006.

[13] R. Martinez, D. Larouche, G. Cailletaud, I. Guillot, and D. Massinon. Simulation of the concomitant process of nucleation-growth-coarsening of Al2Cu particles in a 319 foundry aluminum alloy. *MSMSE*, 23(4), 2015.

[14] Encyclopedia Britannica, 2007.

[15] Joseph R. Davis et al. *Aluminum and aluminum alloys*. ASM international, 1993.

[16] Country Granted Number Year. Bayer's process for alumina production: a historical perspective. *Bull. Hist. Chem*, 17(18):15, 1995.

[17] Vinay Kumar and Linda Milewski. Charles martin hall and the great aluminum revolution. *Journal of Chemical Education*, 64(8):690, 1987.

[18] Dietrich G. Altenpohl. *Aluminum: Technology, applications, and environment; a profile of a modern metal; aluminium from within*. Warrendale, TMS., 1998.

[19] *Aluminum Standards and Data*. The Aluminum Association, 2009.

[20] P.S. Mohanty and J.E. Gruzleski. Grain refinement mechanisms of hypoeutectic Al–Si alloys. *Acta materialia*, 44(9):3749–3760, 1996.

[21] Günter Gottstein. Solidification. In *Physical Foundations of Materials Science*, pages 357–388. Springer, 2004.

[22] David A. Porter, Kenneth E. Easterling, and Mohamed Sherif. *Phase Transformations in Metals and Alloys, (Revised Reprint)*. CRC press, 2009.

[23] D. Massinon and V. Constantin. Formation métallurgie et défauts de fonderie. Montupet Châteauroux, 2002.

[24] F.T. Lee, J.F. Major, and F.H. Samuel. Effect of silicon particles on the fatigue crack growth characteristics of Al-12 Wt pct Si-0.35 Wt pct Mg-(0 to 0.02) Wt pct Sr casting alloys. *Metallurgical and Materials Transactions A*, 26(6):1553–1570, 1995.

[25] M. Haghshenas, A. Zarei-Hanzaki, and S.M. Fatemi-Varzaneh. The effects of thermo-mechanical parameters on the microstructure of thixocast A356 aluminum alloy. *Materials Science and Engineering: A*, 480(1-2):68–74, 2008.

[26] D.G. Eskin, V.I. Savran, L. Katgerman, et al. Effects of alloy composition and casting speed on structure formation and hot tearing during direct-chill casting of Al-Cu alloys. *Metallurgical and Materials Transactions*, 35(11):3551, 2004.

[27] John A. Taylor. The effect of iron in Al-Si casting alloys. In *35th Australian foundry institute national conference, Adelaide, South Australia*, volume 31, pages 148–157, 2004.

[28] L. Lu and A.K. Dahle. Iron-rich intermetallic phases and their role in casting defect formation in hypoeutectic Al–Si alloys. *Metallurgical and Materials Transactions A*, 36(3):819–835, 2005.

[29] L. Wang and S. Shivkumar. Strontium modification of aluminium alloy castings in the expendable pattern casting process. *Journal of materials Science*, 30(6):1584–1594, 1995.

[30] Giulio Timelli and Daniele Caliari. Influence of process parameters on the microstructure and casting defects of a LPDC engine block. In *Shape Casting: 6th International Symposium*, pages 151–158. Springer, 2016.

[31] P. Ouellet and F.H. Samuel. Effect of Mg on the ageing behaviour of Al-Si-Cu 319 type aluminium casting alloys. *Journal of Materials Science*, 34(19):4671–4697, 1999.

[32] Bartłomiej Dybowski, Bogusława Adamczyk-Cieślak, Kinga Rodak, Iwona Bednarczyk, Andrzej Kiełbus, and Jaroslaw Mizera. The microstructure of AlSi7Mg alloy in as cast condition. In *Solid State Phenomena*, volume 229, pages 3–10. Trans Tech Publ, 2015.

[33] R. Martinez, V. Russier, Couzinié, I. Guillot, and G. Cailletaud. Modeling of the influence of coarsening on viscoplastic behaviour of a 319 foundry aluminum alloy. *Mater. Sci. Eng. A*, 559:40, 2013.

[34] M. Karlik and B. Jouffrey. High resolution electron microscopy study of Guinier-Preston (GP1) zones in Al_2Cu based alloys. *Acta materialia*, 45(8):3251–3263, 1997.

[35] Delavand Ovono-Ovono. *Recyclabilité des alliages d'aluminium de fonderie: Influence des éléments résiduels sur la microstructure et le comportement mécanique*. PhD thesis, Université Technologique de Compiègne, 2004.

[36] Emma Sjölander and Salem Seifeddine. The heat treatment of Al–Si–Cu–Mg casting alloys. *Journal of Materials Processing Technology*, 210(10):1249–1259, 2010.

[37] Daniele Casari. *The grain refinement and the Ni/V contamination in the A356 aluminium casting alloy: an experimental study on impact and tensile properties*. PhD thesis, Università degli Studi di Ferrara, 2014.

[38] M. Karlik, B. Jouffrey, and S. Belliot. The copper content of Guinier–Preston (GP1) zones in Al–1.84 at.% Cu alloy. *Acta materialia*, 46(5):1817–1825, 1998.

[39] Katharina Teichmann, Calin D. Marioara, Sigmund J. Andersen, and Knut Marthinsen. Tem study of β' precipitate interaction mechanisms with dislocations and β' interfaces with the aluminium matrix in Al–Mg–Si alloys. *Materials Characterization*, 75:1–7, 2013.

[40] Erhard Hornbogen. Hundred years of precipitation hardening. *Journal of light metals*, 1(2):127–132, 2001.

[41] A. (Anthony) Kelly, R.B Nicholson, and ScienceDirect (Online service). *Precipitation hardening*. Oxford : Pergamon Press, 1963.

[42] H. Liu, I. Papadimitriou, F.X. Lin, and J. LLorca. Precipitation during high temperature aging of Al–Cu alloys: A multiscale analysis based on first principles calculations. *Acta Materialia*, 167:121–135, 2019.

[43] S.K. Son, M. Takeda, M. Mitome, Y. Bando, and T. Endo. Precipitation behavior of an Al–Cu alloy during isothermal aging at low temperatures. *Materials letters*, 59(6):629–632, 2005.

[44] S. Shivkumar, C. Keller, and D. Apelian. Aging behavior in cast Al-Si-Mg alloys. *AFS Transactions*, 98:905–911, 1990.

[45] I. Dutta and S.M. Allen. A calorimetric study of precipitation in commercial aluminium alloy 6061. *Journal of Materials Science Letters*, 10(6):323–326, 1991.

[46] Eva A. Mørtsell, Feng Qian, Calin D. Marioara, and Yanjun Li. Precipitation in an A356 foundry alloy with Cu additions-A transmission electron microscopy study. *Journal of Alloys and Compounds*, 785:1106–1114, 2019.

[47] Takeshi Saito, Eva A. Mørtsell, Sigurd Wenner, Calin D. Marioara, Sigmund J. Andersen, Jesper Friis, Kenji Matsuda, and Randi Holmestad. Atomic structures of precipitates in Al–Mg–Si alloys with small additions of other elements. *Advanced Engineering Materials*, 20(7):1800125, 2018.

[48] G.A. Edwards, K. Stiller, G.L. Dunlop, and M.J. Couper. The precipitation sequence in Al–Mg–Si alloys. *Acta materialia*, 46(11):3893–3904, 1998.

[49] W.F. Miao and D.E. Laughlin. Precipitation hardening in aluminum alloy 6022. *Scripta Materialia*, 40(7):873–878, 1999.

[50] S.J. Andersen, C.D. Marioara, R. Vissers, A. Frøseth, and H.W. Zandbergen. The structural relation between precipitates in Al–Mg–Si alloys, the Al-matrix and diamond silicon, with emphasis on the trigonal phase U1-MgAl2Si2. *Materials Science and Engineering: A*, 444(1-2):157–169, 2007.

[51] S.J. Andersen, C.D. Marioara, A. Frøseth, R. Vissers, and H.W. Zandbergen. Crystal structure of the orthorhombic U2-Al4Mg4Si4 precipitate in the Al–Mg–Si alloy system and its relation to the β' and β" phases. *Materials Science and Engineering: A*, 390(1-2):127–138, 2005.

[52] C.D. Marioara, H. Nordmark, S.J. Andersen, and R. Holmestad. Post-β" phases and their influence on microstructure and hardness in 6xxx Al-Mg-Si alloys. *Journal of materials science*, 41(2):471–478, 2006.

[53] C. Ravi and C. Wolverton. First-principles study of crystal structure and stability of Al–Mg–Si–(Cu) precipitates. *Acta materialia*, 52(14):4213–4227, 2004.

[54] C. Cayron and P.A. Buffat. Transmission electron microscopy study of the β' phase (Al–Mg–Si alloys) and QC phase (Al–Cu–Mg–Si alloys): ordering mechanism and crystallographic structure. *Acta Materialia*, 48(10):2639–2653, 2000.

[55] C.D. Marioara, S.J. Andersen, T.N. Stene, H. Hasting, J. Walmsley, A.T.J. Van Helvoort, and R. Holmestad. The effect of Cu on precipitation in Al–Mg–Si alloys. *Philosophical Magazine*, 87(23):3385–3413, 2007.

[56] S.J. Andersen, H.W. Zandbergen, J. Jansen, C. Traeholt, U. Tundal, and O. Reiso. The crystal structure of the β" phase in Al–Mg–Si alloys. *Acta Materialia*, 46(9):3283–3298, 1998.

[57] R. Vissers, M.A. van Huis, J. Jansen, H.W. Zandbergen, C.D. Marioara, and S.J. Andersen. The crystal structure of the β' phase in Al–Mg–Si alloys. *Acta Materialia*, 55(11):3815–3823, 2007.

[58] Chen Qian, Xie Quan, Zhao Feng-Juan, Cui Dong-Meng, and Li Xu-Zhen. First-principles calculation of electronic structure of Mg2Si with doping. In *2009 International Forum on Information Technology and Applications*, volume 1, pages 338–341. IEEE, 2009.

[59] A. Perovic, D.D. Perovic, G.C. Weatherly, and D.J. Lloyd. Precipitation in aluminum alloys AA6111 and AA6016. *Scripta Materialia*, 41(7):703–708, 1999.

[60] Kenji Matsuda, Susumu Ikeno, Yasuhiro Uetani, and Tatsuo Sato. Metastable phases in an Al-Mg-Si alloy containing copper. *Metallurgical and Materials Transactions A*, 32(6):1293–1299, 2001.

[61] C. Wolverton. Crystal structure and stability of complex precipitate phases in Al–Cu–Mg–(Si) and Al–Zn–Mg alloys. *Acta Materialia*, 49(16):3129–3142, 2001.

[62] Kyoungdoc Kim, Andrew Bobel, Vuk Brajuskovic, Bi-Cheng Zhou, Mike Walker, Gregory B. Olson, and C. Wolverton. Energetics of native defects, solute partitioning, and interfacial energy of Q precipitate in Al-Cu-Mg-Si alloys. *Acta Materialia*, 154:207–219, 2018.

[63] S.I. Bakhtiyarov, R.A. Overfelt, and S.G. Teodorescu. Electrical and thermal conductivity of A319 and A356 aluminum alloys. *Journal of Materials Science*, 36(19):4643–4648, 2001.

[64] Thomas H. Ludwig, Paul L. Schaffer, and Lars Arnberg. Influence of vanadium on the microstructure of A356 foundry alloy. *Light Metals*, 2013.

[65] George W. Smith. Precipitation kinetics in an air-cooled aluminum alloy: a comparison of scanning and isothermal calorimetry measurement methods. *Thermochimica acta*, 313(1):27–36, 1998.

[66] Yan Zheng, Wenlong Xiao, Sujing Ge, Weitao Zhao, Shuji Hanada, and Chaoli Ma. Effects of Cu content and Cu/Mg ratio on the microstructure and mechanical properties of Al–Si–Cu–Mg alloys. *Journal of Alloys and Compounds*, 649:291–296, 2015.

[67] Xiang Wang, Shahrzad Esmaeili, and David J. Lloyd. The sequence of precipitation in the Al-Mg-Si-Cu alloy AA6111. *Metallurgical and materials transactions A*, 37(9):2691–2699, 2006.

[68] D.J. Chakrabarti, Yingguo Peng, David E. Laughlin, et al. Precipitation in Al-Mg-Si alloys with Cu additions and the role of the Q' and related phases. In *Materials Science Forum*, volume 396, pages 857–862. Transtec Publications; 1999, 2002.

[69] Kenneth C. Russell. Nucleation in solids: the induction and steady state effects. *Advances in Colloid and Interface Science*, 13(3-4):205–318, 1980.

[70] John Wyrill Christian. The theory of transformations in metals and alloys. I. equilibrium and general kinetic theory. 1975.

[71] D.A. Porter and K.E. Easterling. *Phase transformations in metals and alloys*. Chapman and Hall, Padstow, Cornwall, 1981.

[72] Jacques Besson, Georges Cailletaud, Jean-Louis Chaboche, and Samuel Forest. *Non-linear mechanics of materials*, volume 167. Springer Science & Business Media, 2009.

[73] Boris S. Bokstein, Mikhail I. Mendelev, David J. Srolovitz, et al. *Thermodynamics and kinetics in materials science: a short course*. Oxford University Press, 2005.

[74] O.R. Myhr, Ø Grong, and S.J. Andersen. Modelling of the age hardening behaviour of Al–Mg–Si alloys. *Acta Materialia*, 49(1):65–75, 2001.

[75] O.R. Myhr, Ø Grong, H.G. Fjaer, and C.D. Marioara. Modelling of the microstructure and strength evolution in Al–Mg–Si alloys during multistage thermal processing. *Acta Materialia*, 52(17):4997–5008, 2004.

[76] Myriam Nicolas and Alexis Deschamps. Characterisation and modelling of precipitate evolution in an Al–Zn–Mg alloy during non-isothermal heat treatments. *Acta Materialia*, 51(20):6077–6094, 2003.

[77] Aude Simar, Yves Bréchet, B. De Meester, A. Denquin, and Thomas Pardoen. Sequential modeling of local precipitation, strength and strain hardening in friction stir welds of an aluminum alloy 6005A-T6. *Acta Materialia*, 55(18):6133–6143, 2007.

[78] Michel Perez. Gibbs–Thomson effects in phase transformations. *Scripta materialia*, 52(8):709–712, 2005.

[79] Q. Du, W.J. Poole, M.A. Wells, and N.C. Parson. Microstructure evolution during homogenization of Al–Mn–Fe–Si alloys: Modeling and experimental results. *Acta Materialia*, 61(13):4961–4973, 2013.

[80] Qiang Du, Michel Perez, Warren J. Poole, and Mary Wells. Numerical integration of the Gibbs–Thomson equation for multicomponent systems. *Scripta Materialia*, 66(7):419–422, 2012.

[81] Bjørn Holmedal, Elisa Osmundsen, and Qiang Du. Precipitation of non-spherical particles in aluminum alloys part I: generalization of the Kampmann–Wagner numerical model. *Metallurgical and Materials Transactions A*, 47(1):581–588, 2016.

[82] Qiang Du, Bjørn Holmedal, Jesper Friis, and Calin D Marioara. Precipitation of non-spherical particles in aluminum alloys part II: numerical simulation and experimental characterization during aging treatment of an Al-Mg-Si alloy. *Metallurgical and Materials Transactions A*, 47(1):589–599, 2016.

[83] Richard Wagner, Reinhard Kampmann, and Peter W Voorhees. Homogeneous second-phase precipitation. *Phase transformations in materials*, 5:309, 2001.

[84] O.R. Myhr and Øystein Grong. Modelling of non-isothermal transformations in alloys containing a particle distribution. *Acta Materialia*, 48(7):1605–1615, 2000.

[85] Yong Du, LiJun Zhang, SenLin Cui, DongDong Zhao, DanDan Liu, WeiBin Zhang, WeiHua Sun, and WanQi Jie. Atomic mobilities and diffusivities in al alloys. *Science China Technological Sciences*, 55(2):306–328, 2012.

[86] Joël Douin. *Mécanique des milieux continus: introduction à la plasticité des matériaux*. Diderot éd., 1997.

[87] Erich Schmid and Walter Boas. Plasticity of crystals. 1950.

[88] G. Sachs and J. Weerts. Tensile tests on gold-silver crystals. *Z. Physik*, 1930.

[89] Geoffrey Ingram Taylor. The mechanism of plastic deformation of crystals. part I.—theoretical. *Proceedings of the Royal Society of London. Series A, Containing Papers of a Mathematical and Physical Character*, 145(855):362–387, 1934.

[90] Derek Hull and David J Bacon. *Introduction to dislocations*, volume 37. Elsevier, 2011.

[91] FRN Nabarro. Dislocations in a simple cubic lattice. *Proceedings of the Physical Society*, 59(2):256, 1947.

[92] Guillaume Fribourg. *Couplages entre précipitation et plasticité dans un alliage d'aluminium 7xxx: application à des traitements thermomécaniques de réduction des distorsions dans des composants aéronautiques*. PhD thesis, Grenoble INPG, 2009.

[93] J.L. Martin. Dislocations et Plasticité des Cristaux, Presses Polytechniques et Universitaires Romandes, Lausanne, 2000. *Price: CHF34, h23*, 10.

[94] Georges Saada et al. L'état métallique. déformation plastique. 1980.

[95] A. Portevin and F. Le Chatelier. The obtention, by thermal treatment, of light aluminium alloys of high resistance not containing magnesium. *C. R. Acad. Sci. Paris*, 177:311, 1923.

[96] Ali Argon. *Strengthening mechanisms in crystal plasticity*, volume 4. Oxford University Press on Demand, 2008.

[97] D. Hull and D.J. Bacon. *Introduction to dislocations*. Butterworth Heinemann, Oxford, 1984.

[98] A. Deschamps and Y. Bréchet. Influence of predeformation and ageing of an Al-Zn-Mg alloy - II. Modeling of precipitation kinetics and yield stress. *Acta Mater.*, 47:293, 1999.

[99] F.C. Frank and W.T. Read Jr. Multiplication processes for slow moving dislocations. *Physical Review*, 79(4):722, 1950.

[100] E.O. Hall. The deformation and ageing of mild steel: III discussion of results. *Proceedings of the Physical Society. Section B*, 64(9):747, 1951.

[101] N.J. Petch. The cleavage strength of polycrystals. *Journal of the Iron and Steel Institute*, 174:25–28, 1953.

[102] A. de Vaucorbeil, W.J. Poole, and C.W. Sinclair. The superposition of strengthening contributions in engineering alloys. *Mater. Sci. Eng. A*, 582:147–154, 2013.

[103] G.P.M. Leyson, L.G. Hector Jr., and W.A. Curtin. Solute strengthening from first principles and application to aluminum alloys. *Acta Materialia*, 60(9):3873–3884, 2012.

[104] J. Friedel. *Dislocations*. Addison-Wesley Publishing Company Inc., Reading, Massachussets, USA, 1964.

[105] R.L. Fleischer and W.R. Hibbard. The relation between the structure and mechanical properties of metals. *Her Majesty's Stationary Office, London*, 261, 1963.

[106] A.J. Ardell. Precipitation hardening. *Metall. Trans.*, 16A:2131, 1985.

[107] C. Gallais, A. Denquin, Y. Bréchet, and G. Lapasset. Precipitation microstructures in an AA6056 aluminium alloy after friction stir welding: Characterisation and modelling. *Materials Science and Engineering: A*, 496(1-2):77–89, 2008.

[108] Aude Simar, Yves Bréchet, B. De Meester, Anne Denquin, Christophe Gallais, and Thomas Pardoen. Integrated modeling of friction stir welding of 6xxx series Al alloys: process, microstructure and properties. *Progress in Materials Science*, 57(1):95–183, 2012.

[109] Jean Lemaitre and Jean-Louis Chaboche. *Mechanics of solid materials*. Cambridge university press, 1994.

[110] A. Deschamps and Y. Brechet. Influence of predeformation and ageing of an Al–Zn–Mg alloy - II. Modeling of precipitation kinetics and yield stress. *Acta Materialia*, 47(1):293–305, 1998.

[111] B. Barlas. *Étude du comportement et de l'endommagement en fatigue d'alliages d'aluminium de fonderie*. PhD thesis, École Nationale Superieure des Mines de Paris, France, 2004.

[112] E. Nicouleau-Bourles. *Étude expérimentale et numérique du vieillissement d'un alliage d'aluminium. Application aux culasses automobiles*. PhD thesis, École Nationale Supérieure des Mines de Paris, France, 1999.

[113] François-Xavier Hoche. *Vers une prise en compte du vieillissement thermique dans la filière de dimensionnement des structures pour la fatigue thermomécanique*. PhD thesis, Paris Sciences et Lettres, 2016.

List of Figures

List of Tables

Appendices

A Frost & Ashby properties of FCC metals

Material	*Nickel*		*Copper*		*Silver*		*Aluminium*		*Lead*		*γ-Iron* (u)	
Crystallographic and thermal data												
Atomic volume, Ω (m^3)	$1{\cdot}09 \times 10^{-29}$		$1{\cdot}18 \times 10^{-29}$		$1{\cdot}71 \times 10^{-29}$		$1{\cdot}66 \times 10^{-29}$		$3{\cdot}03 \times 10^{-29}$		$1{\cdot}21 \times 10^{-29}$	(u)
Burgers vector, b (m)	$2{\cdot}49 \times 10^{-10}$		$2{\cdot}56 \times 10^{-10}$		$2{\cdot}86 \times 10^{-10}$		$2{\cdot}86 \times 10^{-10}$		$3{\cdot}49 \times 10^{-10}$		$2{\cdot}58 \times 10^{-10}$	
Melting temperature, T_M (K)	1726		1356		1234		933		601		1810	
*Modulus**												
Shear modulus at 300 K μ_0 (MN/m^2)	$7{\cdot}89 \times 10^4$	(a)	$4{\cdot}21 \times 10^4$	(f)	$2{\cdot}64 \times 10^4$	(j)	$2{\cdot}54 \times 10^4$	(o)	$0{\cdot}73 \times 10^4$	(r)	$8{\cdot}1 \times 10^4$	(u)
Temperature dependence of modulus, $\frac{T_M}{\mu_0}\frac{d\mu}{dT}$	$-0{\cdot}64$	(a)	$-0{\cdot}54$	(f)	$-0{\cdot}54$	(k)	$-0{\cdot}50$	(o)	$-0{\cdot}76$	(r)	$-0{\cdot}91$	
Lattice diffusion†												
Pre-exponential, D_{0v} (m^2/s)	$1{\cdot}9 \times 10^{-4}$	(b)	$2{\cdot}0 \times 10^{-5}$	(g)	$4{\cdot}4 \times 10^{-5}$	(l)	$1{\cdot}7 \times 10^{-4}$	(p)	$1{\cdot}4 \times 10^{-4}$	(s)	$1{\cdot}8 \times 10^{-5}$	(u)
Activation energy, Q_v (kJ/mole)	284	(b)	197	(g)	185	(l)	142	(p)	109	(s)	270	
Boundary diffusion†												
Pre-exponential, δD_{0b} (m^3/s)	$3{\cdot}5 \times 10^{-15}$	(c)	$5{\cdot}0 \times 10^{-15}$	(h)	$4{\cdot}5 \times 10^{-15}$	(m)	$5{\cdot}0 \times 10^{-14}$	(h)	$8{\cdot}0 \times 10^{-14}$	(t)	$7{\cdot}5 \times 10^{-14}$	(u)
Activation energy, Q_b (kJ/mole)	115	(c)	104	(h)	90	(m)	84	(h)	66	(t)	159	
Core diffusion†												
Pre-exponential, $a_c D_{0c}$ (m^4/s)	$3{\cdot}1 \times 10^{-23}$	(d)	$1{\cdot}0 \times 10^{-24}$	(i)	$2{\cdot}8 \times 10^{-25}$	(n)	$7{\cdot}0 \times 10^{-25}$	(q)	$1{\cdot}0 \times 10^{-22}$	(h)	$1{\cdot}0 \times 10^{-23}$	(u)
Activation energy, Q_c (kJ/mole)	170.	(d)	117	(i)	82	(n)	82	(q)	66	(h)	159	
Power-law creep												
Exponent, n	4·6	(e)	4·8	(e)	4·3	(e)	4·4	(e)	5·0	(e)	4·5	(u)
Dorn constant,‡ A	$3{\cdot}0 \times 10^6$		$7{\cdot}4 \times 10^5$		$3{\cdot}2 \times 10^2$		$3{\cdot}4 \times 10^6$		$2{\cdot}5 \times 10^8$		$4{\cdot}3 \times 10^5$	
P-L breakdown, α'	—		794		—		1000		—		—	
Obstacle-controlled glide												
0 K flow stress, $\hat{\tau}/\mu_0$	$6{\cdot}3 \times 10^{-3}$	(e)	$6{\cdot}3 \times 10^{-3}$	(e)	$7{\cdot}2 \times 10^{-3}$	(e)	$7{\cdot}2 \times 10^{-3}$	(e)	$8{\cdot}7 \times 10^{-3}$	(e)	$1{\cdot}7 \times 10^{-3}$	(u)
Pre-exponential, $\dot{\gamma}_0$ (s^{-1})	10^6		10^6		10^6		10^6		10^6		10^6	
Activation energy, $\Delta F/\mu_0 b^3$	0·5		0·5		0·5		0·5		0·5		0·5	

* $\mu = \mu_0\left(1 + \left(\frac{(T-300)}{T_M}\right)\frac{T_M}{\mu_0}\frac{d\mu}{dT}\right)$.

† $D_v = D_{0v}\exp -\frac{Q_v}{RT}$; $\delta D_b = \delta D_{0b}\exp -\frac{Q_b}{RT}$; $a_c D_c = a_c D_{0c}\exp -\frac{Q_c}{RT}$.

‡ This value of A refers to tensile stress and strain-rate. The maps relate shear stress and strain-rate. In constructing them we have used $A_s = (\sqrt{3})^{n+1}A$.

(a) Alers *et al.* (1960)
(b) Monma (1965).
(c) Wazzan (1965).
(d) Cannon and Stark (1969).
(e) See text.
(f) Chang and Himmel (1966); Overton and Gaffney (1955).
(g) Kuper *et al.* (1954), (1956).
(h) Estimated by setting $\delta D_{0B} = b.D_{0v}$ and $Q_B = 0{\cdot}6Q_v$ or Q_c (if known) $a_c D_{0c} = 4b^2 D_{0v}$ and $Q_c = 0{\cdot}6Q_v$ or Q_B (if known) unless otherwise stated in the text.
(i) Derived from comparison with experiment as described in the text.
(j) Chang and Himmel (1966).
(k) Neighbours and Alers (1958).
(l) Tomizuka and Sonder (1956).
(m) Hoffman and Turnbull (1951).
(n) Turnbull and Hoffman (1954).
(o) Sutton (1953); Lazarus (1959).
(p) Lundy and Murdock (1962).
(q) Balluffi (1970).
(r) Huntington (1958).
(s) Nachtrieb *et al.* (1959).
(t) Okkerse (1954).
(u) Data for γ-Fe are described in full in Chapter 8. They are listed here to permit comparison.

B Thermo-Calc macro example

The following is a Thermo-Calc macro example used to extract the driving force for precipitation of the MG2SI phase. A number of macro files are generated spanning a wide range of Mg content in the alloy. The "DGM(phase)" variable in Thermo-Calc represents the difference in the Gibbs free energy for a unit volume between the precipitating phase and the matrix. It is important to point out that this value is normalized by $R.T$, R being the perfect gas constant and T the temperature in kelvin. Note in the following that comments in the Thermo-Calc console language are preceded by `@@`. They are colored in blue for ease of interpretation.

```
@@Opening the TCAL5 aluminum database
GOTO_MODULE DATABASE

SWITCH_DATABASE

TCAL5

@@Definition of the alloy system, reduced for simplicity
DEFINE_SYSTEM AL SI CU MG

@@All phases are rejected and only the phases of interest are
   restored
REJECT PHASES *

RESTORE PHASES FCC_L12 AL2CU_C16 DIAMOND_A4 MG2SI LIQUID

@@Retrieval of date from the database for the selected phases
GET_DATA

GOTO_MODULE POLY-3

@@Setting thermodynamic conditions for a preliminary equilibrium
   concentration.  Compositions are set to the alloy composition
   with a varying Mg
SET-CONDITIONS N=1 P=1e5 T=300 w(cu)=0.5e-2 w(si)=7e-2 w(mg)=0.001421

@@Changing the phase status to dormant allows calculation of the
   driving force
CHANGE_STATUS PHASE
MG2SI
DORMANT

COMPUTE-EQUILIBRIUM
```

```
@@Definition of a range of temperature over which calculations are
   carried out
SET_AXIS_VARIABLE 1 t 273.15 923.15 1

STEP

NORMAL

@@Definition of the driving force variable deltaGv
ENTER FUNCTION deltaGv

DGM(Mg2Si)*8.314*T;

@@Tabulating the results:  temperature, molar fraction of Mg in
   FCC-Al, deltaGv
ENTER TABLE dGv
t x(fcc_l12,mg) deltaGv;

TABULATE dGv deltaGv_Mg2Si_1421_Mg.txt

EXIT
```

An excerpt of the resulting table is presented in the following :

```
...
col-1=T, col-3=X(FCC_L12#1,MG), col-4=DELTAGV,
4.20000E+02  1.77548E-02 1.58391E+04
4.21000E+02  1.77546E-02 1.58081E+04
4.22000E+02  1.77544E-02 1.57771E+04
4.23000E+02  1.77542E-02 1.57461E+04
4.24000E+02  1.77540E-02 1.57151E+04
4.25000E+02  1.77538E-02 1.56841E+04
4.26000E+02  1.77536E-02 1.56531E+04
4.27000E+02  1.77534E-02 1.56221E+04
4.28000E+02  1.77532E-02 1.55911E+04
...
```

C Source code for the precipitation and yield stress model

The following are commented snippets of the stand alone C++ code for the precipitation and yield stress model. The aim is to highlight key elements of the code such that its functioning is further elucidated. Note that comments in the C++ language are preceded by "//". They are colored in blue for ease of interpretation. The three dots refer to skips in the code where variable declarations and initialization take place which are not of great interest to the reader.

```
// These are the preamble code elements necessary for executing the
   Newton-Raphson algorithm. The third degree polynomial of the
   equiilbrium Mg concentration is defined. Then its derivative is
   also defined and finally a Newton-Raphson resolution scheme is
   implemented. The c0 to c3 coefficients will later be defined as
   a function of various model variables.
...
struct fMgEq {
fMgEq(double c3, double c2, double c1, double c0)
: c3_f(c3)
, c2_f(c2)
, c1_f(c1)
, c0_f(c0)
{}

double operator()(double MgEq) const {
return c3_f*pow(MgEq,3.0) + c2_f*pow(MgEq,2.0) + c1_f*MgEq + c0_f;
}
private:
double c3_f;
double c2_f;
double c1_f;
double c0_f;
};

struct fPrimeMgEq {
fPrimeMgEq(double c3, double c2, double c1)
: c3_f(c3)
, c2_f(c2)
, c1_f(c1)
{}
double operator()(double MgEq) const {
return 3.0*c3_f*pow(MgEq,2.0) + 2.0*c2_f*MgEq + c1_f;
}
private:
double c3_f;
double c2_f;
```

```
double c1_f;
};

double newtonRaphson(double x, double epsilon, double c3, double c2,
    double c1, double c0, double temperature)
{
fMgEq     func(c3,c2,c1,c0);
fPrimeMgEq derivFunc(c3,c2,c1);

double h = func(x) / derivFunc(x);

while (fabs(h) >= epsilon)
{
h = func(x)/derivFunc(x);
x = x - h;
//cout << "residu=" << fabs(h) << endl;
}
return x;
}
...
// Discretization parameters are defined.  The time step upper limit
    and the precision coefficient.  The size space is discretized
    into nm equal size classes (dr) from the minimum radius to the
    maximum.
...
double dt_u    = 5.;
double coefU   = 0.9;

int    nm         = 296;
double dr         = 0.05e-09;
double radMax = 15.0e-09;
double radMin = 0.2e-09;
...
// The concentrations within Mg2Si, supposed stœchiometric, are
    defined.  Then the initial values of the concentration in the
    matrix at the solutionizing temperature according to Thermo-Calc
    are set.
...
double MgPre = 0.666;
double SiPre = 0.334;
double Mg0 = 4.73404e-03;
double Si0 = 1.11337e-02;

int main(){

// The corrections dependent on the shape factor are defined here.
...
```

```
shapeFactorBeta      = 6.6;
growthCorrectionBeta = (2*sqrt(pow(shapeFactorBeta,2.0)-1.0))/(pow(
    shapeFactorBeta,(1.0/3.0))*log(2*pow(shapeFactorBeta,2.0)+2*
    shapeFactorBeta*sqrt(pow(shapeFactorBeta,2.0)-1.0)-1.0));
gThomsonCorrectionBeta = ((2*shapeFactorBeta+1.0)/(2*M_PI))*pow(((4*
    M_PI)/(3*shapeFactorBeta)),(2.0/3.0));
...

// Declaration of the maximum admissible time step, initialization of
    time and definition of the total simulation time.  Then the loop
    over time starts.
...
double dt_Adm;
double t = 0.;
double totalTime = 38900.;

while (t <= totalTime){
...

// Definition of the thermal history.  This is an example where the
    transients are time controlled.  It is possible to do the same in
    a rate controlled manner.
double quenchTime = 120., quenchTemperatureStart = 813.15,
    quenchTemperatureEnd = 293.15;
double naturalAgingTime = 1880., naturalAgingTemperature = 293.15;
double agingHeatingTime = 900., agingTemperature = 473.15;
double quenchRate = (quenchTemperatureStart - quenchTemperatureEnd)/
    quenchTime;
double agingHeatingRate = (agingTemperature - naturalAgingTime)/
    agingHeatingTime;
double agingHeatingStartTime = quenchTime + naturalAgingTime;
double agingStartTime = agingHeatingStartTime + agingHeatingTime;

//Quench
if (t <= Q_time) {Temperature = Q_T_start - Q_rate*t;}
//Natural aging
if (t > Q_time && t <= AHT_H_start) {Temperature = NA_T;}
//Aging HT heating
if (t > AHT_H_start && t <= AHT_start) {Temperature += AHT_rate*dt;}
//Aging HT hold
if (t > AHT_start) {Temperature = AHT_T;}
...

//Definition of the atomic diffusivities.
...
DiffMg = DOMg*exp(-qMg/(perfectGaz*Temperature));
DiffSi = DOSi*exp(-qSi/(perfectGaz*Temperature));
```

```
...

//Definition of the available silicon concentration in the matrix.
   Contrary to Mg0 which is constant, Si0 varies as a function of
   Temperature as Si participates in the formation of a phase other
   than Mg2Si (the Si phase).  Then the conversion from volume
   fraction to molar fraction is made in order to introduce the mass
   balance equation calculating the mean solute content.
   coefAlphaInv is the ratio between the molar volume of Mg2Si and
   that of the matrix.
...
Si0   = (11.8823311456309*exp(-6004.36592881425/Temperature)
   +0.00238605644562167)*((Temperature <= 7.58514E+02)?1:0)
   +(11.9334636957044*exp(-5670.5375376213/Temperature)
   +-3.97042147335617e-05)*((Temperature > 7.58514E+02)?1:0);

molarFractionBeta = volumeFractionBeta/(coefAlphaInv +
   volumeFractionBeta*(1. - coefAlphaInv));
MgBar = Mg0-(molarFractionBeta*MgPre))/(1.-molarFractionBeta);
SiBar = Si0-(molarFractionBeta*SiPre))/(1.-molarFractionBeta);
...

//Precipitation driving force for Mg2Si fitted on data extracted
   using Thermo-Calc/TCAL5
...
deltaGvBeta       = -3.6516762664448237e+04/(1.0/Temperature)
   -1.0300542835149117e+07*log(MgBar)-4.4530917064438512e+02/pow
   ((1.0/Temperature),2.0)-2.9830189042941332e+04*pow(log(MgBar)
   ,2.0)+4.4579777571176417e+05*log(MgBar)/(1.0/Temperature)
   +2.0372938422416959e+09;
...

//Nucleation equations leading up to the evaluation of the nucleation
   rate jNucleationBeta.
...
rStarNucleationBeta = 2.*surfaceEnergyBetaNuc/deltaGvBeta;
zeldovitchBeta    = vAlpha*pow(deltaGvBeta,2.)/(8.*M_PI*sqrt(pow(
   surfaceEnergyBetaNuc,3.)*kB*Temperature));
deltaGstarBeta    = (16.*M_PI*pow(surfaceEnergyBetaNuc,3.))/(3.*pow(
   deltaGvBeta,2.));
betaStarBeta      = (16.*M_PI*pow(surfaceEnergyBetaNuc,2.)*DiffMg*
   MgBar)/(pow(deltaGvBeta,2.)*pow(latticeParam,4.));
tauBeta           = (8.*kB*Temperature*surfaceEnergyBetaNuc*pow(
   latticeParam,4.))/(pow(vAlpha,2.)*pow(deltaGvBeta,2.)*DiffMg*
   MgBar);
jNucleationBeta   = zeldovitchBeta*betaStarBeta*N0*exp(-1.*
   deltaGstarBeta/(kB*Temperature))*exp(-tauBeta/t);
```

```
...

//Shear modulus according to Ashby and Frost Properties of FCC
   metals.
...
G = 2.64e+10*(1.-0.5*((Temperature - 300.0)/886.83));
...

//Initialization of the admissible time step and a bool test.
...
bool dtOK = 1;
dtAdm    = 1.0e+20;
...

//Loop over the size classes calculating the growth rate and defining
   the maximal admissible time step.
for (int i = 0 ; i <= nm-1; i++){

//Gibbs-Thomson curvature corrections.
correctionSiGT = exp((2.*gThomsonCorrectionBeta*surfaceEnergyBetaGro*
   molarVolumeBeta)/(SiPre*rBeta[i]*perfectGaz*Temperature));
correctionMgGT = exp((2.*gThomsonCorrectionBeta*surfaceEnergyBetaGro*
   molarVolumeBeta)/(MgPre*rBeta[i]*perfectGaz*Temperature));

//Definition of the polynomial parameters for the Newton-Raphson
   algorithm.
c3 = DiffSi*SiBar - DiffMg*SiPre*coefAlpha;
c2 = DiffMg*MgBar*SiPre*coefAlpha - DiffSi*SiBar*MgPre*coefAlpha;
c1 = (DiffMg - DiffSi)*pow(10.0,(-7144.83024258463/Temperature) +
   2.69175189050442)*correctionMgGT*correctionSiGT;
c0 = (DiffSi*MgPre*coefAlpha - DiffMg*MgBar)*pow
   (10.0,(-7144.83024258463/Temperature) + 2.69175189050442)*
   correctionSiGT;

//Execution of the Newton-Raphson algorithm, the maximal residual is
   set by eps = 1.0e-12 and the root search occurs between 0 and 1.
   The result is the equilibrium Mg concentration satisfying the
   thermodynamic and kinetic constraints.  The Si equilibrium
   concentration is then calculated using the solubility product.
operMgEq = newtonRaphson(1.0, eps, c3, c2, c1, c0, Temperature);
operSiEq = pow(10.0,(-7144.83024258463/Temperature) +
   2.69175189050442)/pow(operMgEq,2.0);

MgInt[i] = operMgEq*correctionMgGT;
SiInt[i] = operSiEq*correctionSiGT;
```

```
//The growth rate can therefore be calculated using either element Mg
    or Si.
growRateBetaMg[i] = growthCorrectionBeta*(DiffMg/rBeta[i])*(MgBar -
    MgInt[i])/(coefAlpha*MgPre - MgInt[i]);
growRateBetaSi[i] = growthCorrectionBeta*(DiffSi/rBeta[i])*(SiBar -
    SiInt[i])/(coefAlpha*SiPre - SiInt[i]);

growRateBeta[i] = growRateBetaMg[i] =;

//Definition of the maximal admissible time step.  The treatment is
    only made over classes with non null number densities.
if (rhoBeta[i] > 0.0){
dtOK = 0;
dtAdm = min(dtAdm, dr/fabs(growRateBeta[i]));
}
}

//Loop ends and the actual time step is defined.  It is the minimum
    between the admissible time step, here multiplied by a precision
    coeffcient (coefU which is less than 1), and the upper limit set
    earlier.  The time step is therefore validated and the time is
    then incremented.

if(dtOK == 0){
dt = min(coefU*dtAdm,dt_u);
}
t  = t + dt;

//The size classes right above the critical nucleation radius are
    filled by the nucleating particles
...
if (deltaGvBeta <= 0.0 || jNucleationBeta*dt/dr <= 1.0){
jNucleationBeta = 0.0;
}

for (int i = 0 ; i <= nm-1; i++){
if (jNucleationBeta*dt/dr > 1.0 && rStarNucleationBeta > rBeta[i] &&
    rStarNucleationBeta < rBeta[i+1])
{rhoBeta[i+1] += jNucleationBeta*dt/dr;}
else
{rhoBeta[i+1] += 0.0;}
}

//The tridiagonal matrix is hereby filled according to the
    considerations exposed in chapter 4.
for (int i = 0 ; i <= nm-1; i++){
```

```
if (rhoBeta[i] >= 0 && i > 0 && i < nm-1 && growRateBeta[i-1] > 0. &&
     growRateBeta[i] > 0.) {mark = 1;}
if (rhoBeta[i] >= 0 && i > 0 && i < nm-1 && growRateBeta[i] < 0. &&
    growRateBeta[i+1] < 0.) {mark = 2;}
if (rhoBeta[i] >= 0 && i > 0 && i < nm-1 && growRateBeta[i-1] > 0. &&
     growRateBeta[i+1] < 0.) {mark = 3;}
if (rhoBeta[i] >= 0 && i > 0 && i < nm-1 && growRateBeta[i-1] < 0. &&
     growRateBeta[i+1] > 0.) {mark = 4;}
if (rhoBeta[i] >= 0 && i == 0)
                                                          {mark = 5;}
if (rhoBeta[i] >= 0 && i == nm-1)
                                                       {mark = 6;}

switch (mark) {
case 1:
AeBeta[i] = 0.;
AwBeta[i] = growRateBeta[i-1];
ApOBeta[i] = dr/dt;
ApBeta[i] = dr/dt + growRateBeta[i];
aBeta[i]  = -1.*AwBeta[i]/ApOBeta[i];
bBeta[i]  =    ApBeta[i]/ApOBeta[i];
cBeta[i]  = -1.*AeBeta[i]/ApOBeta[i];
break;

case 2:
AeBeta[i] = -growRateBeta[i+1];
AwBeta[i] = 0.;
ApOBeta[i] = dr/dt;
ApBeta[i] = dr/dt - growRateBeta[i];
aBeta[i]  = -1.*AwBeta[i]/ApOBeta[i];
bBeta[i]  =    ApBeta[i]/ApOBeta[i];
cBeta[i]  = -1.*AeBeta[i]/ApOBeta[i];
break;

case 3:
AeBeta[i] = -growRateBeta[i+1];
AwBeta[i] = growRateBeta[i-1];
ApOBeta[i] = 2.*dr/dt;
ApBeta[i] = 2.*dr/dt;
aBeta[i]  = -1.*AwBeta[i]/ApOBeta[i];
bBeta[i]  =    ApBeta[i]/ApOBeta[i];
cBeta[i]  = -1.*AeBeta[i]/ApOBeta[i];
break;

case 4:
AeBeta[i] = -growRateBeta[i+1];
AwBeta[i] = growRateBeta[i-1];
```

```
ApOBeta[i] = 2.*dr/dt;
ApBeta[i] = 2.*dr/dt;
aBeta[i]  = -1.*AwBeta[i]/ApOBeta[i];
bBeta[i]  =    ApBeta[i]/ApOBeta[i];
cBeta[i]  = -1.*AeBeta[i]/ApOBeta[i];
break;

case 5:
AeBeta[i] = -growRateBeta[i+1];
AwBeta[i] = 0.;
ApOBeta[i] = dr/dt;
ApBeta[i] = dr/dt - growRateBeta[i];
aBeta[i]  = -1.*AwBeta[i]/ApOBeta[i];
bBeta[i]  =    ApBeta[i]/ApOBeta[i];
cBeta[i]  = -1.*AeBeta[i]/ApOBeta[i];
break;

case 6:
AeBeta[i] = 0.;
AwBeta[i] = growRateBeta[i-1];
ApOBeta[i] = dr/dt;
ApBeta[i] = dr/dt + growRateBeta[i];
aBeta[i]  = -1.*AwBeta[i]/ApOBeta[i];
bBeta[i]  =    ApBeta[i]/ApOBeta[i];
cBeta[i]  = -1.*AeBeta[i]/ApOBeta[i];
break;

default:
break;
}
}

//The tridiagonal matrix is inverted thanks to the tridiagonal matrix
   algorithm coded in the function tridiagsingle.  This function
   takes as input the parameters above, the current number density
   vector rhoBeta and outputs the number density resBeta after the
   time increment.  The code for this function can be found below.
tridiagSingle (aBeta, bBeta, cBeta, rhoBeta, resBeta, nm);

for (int i = 0 ; i <= nm-1; i++){
rhoBeta[i] = resBeta[i];
}

//Integrating the size distribution to obtain the volume fraction,
   the total number density etc.  The various sums over the
   shearable precipitates and bypasses precipitates are also
   calculated here to be subsequently used in calculating their
```

```
    contributions to the yield stress.
for (int i = 0 ; i <= nm-1; i++){
volumeFractionBeta += 4./3.*M_PI*pow(rBeta[i],3.0)*rhoBeta[i]*dr;
sumRandRhoBeta    += rBeta[i]*rhoBeta[i]*dr;
sumRhoBeta        += rhoBeta[i]*dr;
totalRho          += rhoBeta[i];

if (rBeta[i] <= criticRadiusForShearing){
sumRhoBetaShear += rhoBeta[i]*dr;
sumRandRhoShear += rBeta[i]*rhoBeta[i]*dr;
sumLandRhoShear += lengthRodBeta[i]*rhoBeta[i]*dr;
}

if (rBeta[i] > criticRadiusForShearing){
sumRandRhoBypass += rBeta[i]*rhoBeta[i]*dr;
sumLandRhoBypass += lengthRodBeta[i]*rhoBeta[i]*dr;
}
}

//Updating the system in terms of molar fraction, mean radius and
    mean solute content.  The cases with and without precipitates are
    distinguished.  The yield stress is then calculated accordingly
    by adding up the various available contributions.

molarFractionBeta = volumeFractionBeta/(coefAlphaInv +
    volumeFractionBeta*(1. - coefAlphaInv));

if (sumRhoBeta == 0.){//Still no precipitation.
MgBar   = Mg0;
SiBar   = Si0;

meanRadiusBeta = 0.0;

sigmaMg = taylorFactor*kMg*pow(MgBar,(2./3.));
sigmaSi = taylorFactor*kSi*pow(SiBar,(2./3.));
sigmaSS = sqrt(pow(sigmaMg,2.0) + pow(sigmaSi,2.0));
sigmaY = sigmaLattice + sigmaSS;
}

if (sumRhoBeta > 0.){//Precipitation has begun.
MgBar         = max((Mg0-(molarFractionBeta*MgPre))/(1.-
    molarFractionBeta),1.1*MgEq);
SiBar         = max((Si0-(molarFractionBeta*SiPre))/(1.-
    molarFractionBeta),1.1*SiEq);

meanRadiusBeta = sumRandRhoBeta/sumRhoBeta;
```

```
sigmaShear    = (1.0e-06)*(taylorFactor*pow(k,1.5)*G/(sqrt(2.0*sqrt
    (3.0)*beta*burgers)))*sqrt(sumLandRhoShear)*pow((sumRandRhoShear/
    sumRhoBetaShear),1.5);
sigmaBypass   = (1.0e-06)*taylorFactor*sqrt(2.0)*beta*G*burgers*sqrt(
    sumLandRhoBypass);
sigmaMg       = taylorFactor*kMg*pow(MgBar,(2./3.));
sigmaSi       = taylorFactor*kSi*pow(SiBar,(2./3.));
sigmaSS       = sqrt(pow(sigmaMg,2.0) + pow(sigmaSi,2.0));
sigmaP        = pow((pow(sigmaBypass,q) + pow(sigmaShear,q)),(1./q));
sigmaY        = sigmaLattice + sigmaSS + sigmaP;
}

return 0;
}
```

The following is the code for the tridiagonal matrix inversion algorithm used as a function in the code above. This code is included in a header file.

```
void tridiagSingle (double* diagLow, double* diag, double* diagUpp,
    double* input, double* result, int n) {

double gam[n];
double bet;
if (diag[0] == 0.0) {
//cout << "Error 1 in TRIDIAG1"<< endl;
}
bet = diag[0];
result[0] = input[0]/bet;

for (int i = 1; i < n; i++) {
gam[i]= diagUpp[i-1]/bet;
bet = diag[i]-diagLow[i]*gam[i];
if (bet == 0.0) {
//cout << "Error 2 in TRIDIAG1" << endl;
}
result[i] = (input[i] - diagLow[i]*result[i-1]) / bet;
}

for (int i = n-2; i >= 0; i--) {
result[i] -= gam[i+1]*result[i+1];
}
}
```

D Source code for the precipAlu postprocessing

The following are commented snippets of the manner in which the stand alone C++ code for the preciptiation and yield stress model is coupled to the Z-Set local post-processing environment. The aim is to show the simple manner by which the code is utilized in the finite element framework. To avoid repetition, only the snippets pertaining to the Z-Set environment will be shown, the code will be referred to in commentary. The reader can refer to Appendix C for the detailed source code of the model. Recall that comments in the C++ language are preceded by "//" and are hereby colored in blue for ease of interpretation.

```
#include <Local_post_computation.h>
#include <Post_timer.h>

namespace ZSET {

class PRECIPALU:public LOCAL_POST_COMPUTATION {
public :

//All the variables are declared here.  var_name stands for the input
   variable name.  This will be temperature.
STRING var_name;
int nm;
double radMin;
double radMax;
double dr;
...

//The tridiagonal matrix inversion function and the Newton-Raphson
   functions are declared here.  In the Z-Set post-processing
   environment the function "input_i_need" is used to define and
   retrieve the input variables.  "output_i_give" defines the output
   variables, and compute refers to the actual calculations which
   link the two.  The MODIFY_INFO_RECORD is used in order to
   override parameter initializations made here using values entered
   by the user in the input file.
void tridiagSingle (VECTOR& diagInf, VECTOR& diag, VECTOR& diagSup,
   VECTOR& input, VECTOR& result, int n);
void newtonRaphson (double x, double epsilon, double c3, double c2,
   double c1, double c0, double temperature);
PRECIPALU();
~PRECIPALU(){}
virtual MODIFY_INFO_RECORD* get_modify_info_record();
virtual bool verify_info();
virtual void input_i_need(int,ARRAY<STRING>&);
virtual void output_i_give(bool&,ARRAY<STRING>&);
```

```
virtual void compute(const ARRAY<VECTOR>&,ARRAY<VECTOR>&);
};
}

using namespace ZSET;

//The record modification function is used here for example to allow
   the user to define their own size discretization parameters (nm,
   dr, radMax and radMin).  Any other parameter can be allowed to be
   modified directly by the user in the input file.

DECLARE_OBJECT(LOCAL_POST_COMPUTATION,PRECIPALU,precipAlu)
MODIFY_INFO_RECORD* PRECIPALU::get_modify_info_record(){
MODIFY_INFO_RECORD* ret = new MODIFY_INFO_RECORD;
ret->ptr = (void*)this;
ret->info = "PRECIPALU";
ADD_SINGLE_CMD_TO_MODIF_REC(var, var_name);
ADD_SINGLE_CMD_TO_MODIF_REC(nm, nm);
ADD_SINGLE_CMD_TO_MODIF_REC(dr, dr);
ADD_SINGLE_CMD_TO_MODIF_REC(radMax, radMax);
ADD_SINGLE_CMD_TO_MODIF_REC(radMin, radMin);
return( ret );
}

PRECIPALU::PRECIPALU(){
//Here, all the fixed parameters are initialized.  These values are
   overridden with the record modification.
...
avogadro          = 6.0221413e+23;
perfectGaz        = 8.3144621;
latticeParam      = 4.0412e-10;
...
}

bool PRECIPALU::verify_info() {
return TRUE;
}

//The required input is specified here by var_name.  The
   post-processing considers therefore the variable name given by
   the user in the input file after *var_name.
void PRECIPALU::input_i_need(int,ARRAY<STRING>& ret) {
ret.resize(1);
ret[0]=var_name;
}
```

```
//The output vector is defined here.  In this example, temperature,
   the nucleation rate, mean radius, volume fraction, total number
   density and yield stress are output.
void PRECIPALU::output_i_give(bool& every_card,ARRAY<STRING>& ret) {
every_card=TRUE;
ret.resize(6);
ret[0]="temperature";
ret[1]="jNucleation";
ret[2]="meanRadius";
ret[3]="volumeFraction";
ret[4]="sumRho";
ret[5]="sigmaY";
}

//The computation occurs here.
void PRECIPALU::compute(const ARRAY<VECTOR>& in,ARRAY<VECTOR>& out)

//The time step is inherited from the input maps as the difference in
   time stamps between the current and the previous map.  Artificial
   maps are interpolated in order to satisfy the CFL condition if
   need be.
for (int icard = 0 ; icard <! in ; icard++) {
double time, _Dtime;
time = TimePost(icard);
if (icard == 0) {
_Dtime = TimePost(icard);
}

else {
_Dtime = TimePost(icard)-TimePost(icard-1);
}

//Temperature is read directly from the map at each time step.

temperature = in[icard][0];
int mark   = 0;

...
//The stand alone code is inserted as is without any further
   considerations.
...

//Output maps are hereby generated.
out[icard][0] = temperature;
out[icard][1] = jNucleation;
out[icard][2] = meanRadius;
out[icard][3] = volumeFraction;
```

```
out[icard][4] = sumRho;
out[icard][5] = sigmaY;
}
}

//The tridiagonal matrix inversion and the Newton-Raphson algorithms
    are coded here.
void PRECIPALU::tridiagSingle (VECTOR& diagInf, VECTOR& diag, VECTOR&
     diagSup, VECTOR& input, VECTOR& result, int n) {
...
...
}

void PRECIPALU::newtonRaphson (double x, double epsilon, double c3,
    double c2, double c1, double c0, double temperature)
{
...
...
}
```

E Thermal calculation input file

The following is a simple input for a thermal transient finite element calculation using Z-Set. Note that comments in the Z-Set environment are preceded by "%". They are colored in blue for ease of interpretation.

```
****calcul thermal_transient
% Calling the mesh file.
 ***mesh **file ../GEOF/finemesh.geof
 ***resolution
  **sequence
% Definition of the time sequence.  A large number of
    increments is used for sequences where transients will
    take place.  A Newton-Raphson algorithm is used with an
    option for dividing the time step to ensure convergence.
   *time        600. 2300. 3200. 10400. 12100. 14000.
   *increment   600   170   600    600    425    100
   *iteration 20
   *algorithm p1p2p3
  **automatic_time
   *divergence 2. 10
   *security 1.5
% Uniform temperature over the whole structure 813.15 K.
 ***init_dof_value
    TP uniform 813.15
% The boundary conditions are applied to the node sets
    according to the description made in chapter 4.
 ***bc **impose_nodal_dof
       Bottom    TP 1.0 tab
       SparkPlug TP 1.0 tab
       Valve     TP 1.0 tab
       Left      TP 1.0 tab
% The heat treatment sequence is hereby defined.
 ***table **name tab
   *time   0.    600.   2300.   3200. 10400.  12100.   14000.
   *value 813.15 293.15 293.15 473.15 473.15  293.15  293.15
 ***material *this_file
****return

% The material file is simply defined in the input file.
 ***behavior thermal
  **conductivity isotropic
    k   217.6
  **coefficient
    capacity 950.
 ***return
```

F Material file for FEM mechanical calculations

The following is the Z-Set mechanical behavior law file for the studied material. Note that R0 stands for yield stress and it is defined as a parameter taken from the results of the precipAlu postprocessing (see Appendix H). All the other variables were identified thanks to cyclical tensile tests from previous studies. Note that the file is written in two columns.

```
***behavior gen_evp
**elasticity isotropic
young  temperature
76000. 293.15
75000. 423.15
62000. 473.15
57000. 553.15
54778. 573.15
53826. 593.15
53826. 900.15
poisson 0.3
**thermal_strain isotropic
alpha function (2.702e-08*
   temperature + 8.459e-06);
ref_temperature 293.15

**potential gen_evp ep
*criterion mises
*flow norton
n     temperature
5.58  293.15
4.49  423.15
4.06  473.15
3.22  573.15
3.22  593.15
3.22  900.15
K    temperature
5.   293.15
100. 423.15
80.  473.15
60.  573.15
60.  593.15
60.  900.15
*kinematic nonlinear
C      temperature
110000. 293.15
110000. 423.15
38000. 473.15
25000. 553.15
22000. 573.15
19000. 593.15
19000. 900.15
D     temperature
1100. 293.15
1800. 423.15
2000. 473.15
2300. 553.15
2800. 573.15
2000. 593.15
2000. 900.15
*kinematic nonlinear
C     temperature
25000. 293.15
16000. 423.15
4500.  473.15
1700.  553.15
1600.  573.15
1200.  593.15
1200.  900.15
D 100.
*isotropic nonlinear
R0 function sigmaY;
Q     temperature
5.6   293.15
-2.0  423.15
-31.0 473.15
-26.0 553.15
-15.0 573.15
-13.0 593.15
-13.0 900.15
b   temperature
2.0 293.15
2.0 423.15
1.2 473.15
0.8 553.15
0.3 573.15
0.2 593.15
0.2 900.15
***return
```

G precipAlu post-processing input file

The following is an example input file for the precipAlu Z-Set post-processing. Recall that comments in the Z-Set environment are preceded by "%". They are colored in blue for ease of interpretation.

```
% The thermal calculation result file is opened here.
****post_processing
 ***data_source Z7
  **open        ../THERM/thermique.ut
 ***precision   6

% In this example the post-processing is applied to
    integration points.  The input variable is therefore given
    here and is named temperature.  As mentioned in the
    post-processing source code, the record is here modified
    by the input file in terms of the size discretization
    parameters.
 ***local_post_processing
  **file        integ
  **elset       ALL_ELEMENT
  **process     precipAlu
   *var         temperature
   *nm          198
   *dr          0.1e-09
   *rayonMax    20.0e-09
   *rayonMin    0.2e-09
****return
```

H Mechanical calculation input file

The following is an the input file for the mechanical Z-Set calculation. Recall that comments in the Z-Set environment are preceded by "%". They are colored in blue for ease of interpretation.

```
****calcul
 ***mesh plane_strain **file ../GEOF/finemesh.geof
 ***resolution
  **automatic_time automatic_by_sequence global 3
   *divergence 2. 10  *security 1.2
  **sequence
   *time        600. 2300. 3200. 10400. 12100. 14000.
   *increment   600   170   600    600    425    100
   *algorithm p1p2p3
   *iteration 10
   *ratio absolu 1.
% The yield stress parameter is read from a file output by the
    precipAlu post-processing (sigmay.dat).  rec_size refers
    to the number of Gauss points in the mesh.
 ***parameter
  **file sigmaY
   *ip
   *rec_size 3344
   *table_file sigmay.dat
% Temperature is read from a file output by the thermal
    calculation (temperature.dat).  rec_size refers to the
    number of nodes in the mesh.
  **file temperature
   *node
   *rec_size 2664
   *table_file temperature.dat
% The displacement boundary conditions are set according to
    the description in chapter 4.
 ***bc **impose_nodal_dof
    RIGHT U1 0.
    TOP   U2 0.
% The material file is called here.  Aside from the yield
    stress, all material the parameters of the constitutive
    equations are found in this file.
 ***material
   *file  Material_file.mat
   *integration theta_method_a 1. 1.e-09 200
 ***output **save_parameter
****return
```

RÉSUMÉ

Les alliages d'aluminium du type A356+0.5Cu sont fortement utilisés en fonderie pour l'application culasses automobile en raison de leurs bonnes propriétés thermiques et mécaniques. La limite d'élasticité de ces alliages est étroitement reliée à la microstructure de précipitation dont la formation et l'évolution sont contrôlées par la diffusion. Dans ce travail, la cinétique de précipitation de la phase durcissante β"-Mg_2Si et la limite d'élasticité associée ont été modélisées. La précipitation a été modélisée en se basant sur la théorie classique de la germination et la croissance contrôlée par la diffusion. L'approche numérique KWN de discrétisation en classes de tailles a été employée afin de suivre l'évolution des distributions de tailles en réponse à un historique thermique. La limite d'élasticité a été modélisée en additionnant les contributions des précipités et le durcissement par solution solide de façon directement informée par le modèle de précipitation. La contribution des précipités a été modélisée en prenant en compte leur morphologie en bâtonnets et leur orientation dans la matrice. Des échantillons ont été coulés et ont été assujettis à un traitement thermique de mise en solution, trempe et vieillissement pour des durées variables. Le modèle a ensuite été confronté à deux niveaux aux résultats d'expériences conduites sur ces échantillons. D'une part, les distributions de tailles simulées ont été comparées aux mesures effectuées grâce à des observations par microscopie électronique en transmission. D'autre part, la limite d'élasticité simulée a été comparée aux résultats d'essais de traction. Finalement, une chaîne de calculs éléments-finis intégrant ces modèles a été mise au point dans le code de calcul Z-Set. Des simulations de traitement thermique de trempe et vieillissement ont été effectuées permettant la représentation des gradients de propriété ainsi que l'estimation et la localisation des contraintes résiduelles.

MOTS CLÉS

Durcissement par précipitation, KWN, alliages d'aluminium de fonderie, calcul par éléments finis, modélisation multi-physique

ABSTRACT

Aluminum alloys of type A356+0.5Cu are widely used in casting cylinder heads for automotive applications due to their good thermal and mechanical properties. The yield stress in these alloys is closely related to precipitation microstructure, the formation and evolution of which are diffusion controlled. In this work, the precipitation kinetics of the β"-Mg_2Si hardening phase and the associated evolution of yield stress are modelled. Precipitation is modelled based on classical nucleation theory equations and diffusion controlled growth. The KWN size class discretization approach was used to track the evolution of size distributions of precipitates in response to a given thermal history. Yield stress was modelled by adding up the contributions of precipitates and solid solution strengthening in a manner directly informed by the precipitation model. The contribution of precipitates was modelled taking into account their rod morphology and their orientation in the matrix. Samples were cast and were subject to a solutionizing, quenching and aging heat treatment for various durations. The model was then confronted, on two levels, to the results of experiments conducted on these samples. On the one hand, simulated size distributions were compared to measurements performed on precipitates observed using electron transmission microscopy. On the other hand, the simulated yield stress was compared to the results of tensile tests. Finally, a finite-elements computation chain integrating these models was developed in the Z-Set framework. It was then used to simulate quenching and aging heat treatment making possible tracking of property gradients as well as estimating and localizing residual stresses.

KEYWORDS

Precipitation hardening, KWN, cast aluminum alloy, finite-element computations, multi-physics modelling